

Sensitivity of Jet Observables to Molière Scattering Off Quasiparticles in Quark-Gluon Plasma

Zachary Hulcher,^a Arjun Srinivasan Kudinoor,^b Daniel Pablos,^{c,d} Krishna Rajagopal^b

^a*SLAC National Accelerator Laboratory, Menlo Park, CA 94025, USA*

^b*Center for Theoretical Physics — a Leinweber Institute, Massachusetts Institute of Technology, 77 Massachusetts Ave, Cambridge, MA 02139, USA*

^c*Departamento de Física, Universidad de Oviedo, Avda. Federico García Lorca 18, 33007 Oviedo, Spain*

^d*Instituto Universitario de Ciencias y Tecnologías Espaciales de Asturias (ICTEA), Calle de la Independencia 13, 33004 Oviedo, Spain*

E-mail: zhulcher@stanford.edu, kudinoor@mit.edu,

pablosdaniel@uniovi.es, krishna@mit.edu

ABSTRACT: Quark-gluon plasma (QGP) behaves as a strongly coupled liquid when viewed at length scales of order the inverse of its temperature and longer. However, when it is probed at sufficiently short length scales, with sufficiently high momentum-exchange, the asymptotic freedom of QCD mandates the presence of quark- and gluon-like quasiparticles. High-energy partons in jets can trigger such perturbative, high momentum-exchange $2 \rightarrow 2$ Molière scatterings off quasiparticles in the medium, making jets useful probes with which to study the microscopic structure of QGP. Prior to this work, as appropriate for a strongly coupled liquid, nonperturbative soft momentum-exchanges between jet partons and the hydrodynamic droplet of QGP produced in a heavy-ion collision, as well as the wakes that jets excite in the droplet, had been accounted for in the hybrid strong/weak coupling model of jet quenching. Here, we present a full calculation of Molière scattering and describe how it is implemented in the Hybrid Model. Molière scattering off a quasiparticle in the medium results in the deflection of the jet parton and the excitation of a parton from the thermal medium that recoils after being kicked. The scattered jet parton and the recoil parton continue to propagate through the QGP, lose energy and momentum, excite wakes, and may further re-scatter. Using the Hybrid Model, we study how Molière scatterings impact a variety of observables including jet shapes and fragmentation functions, the Soft Drop splitting angle R_g , jet girth g , and observables that focus on the number and angular distribution of subjects within jets. We demonstrate that photon-tagged jets provide a particularly sensitive probe: selecting events by the photon energy mitigates the selection bias inherent in inclusive jet measurements and enhances sensitivity to rare large-angle scatterings. We find that Molière scatterings broaden both the R_g and g distributions when jets significantly softer than the photon are included. Our results point the way towards distinctive model-independent experimental signatures of hard scattering of jet partons off quasiparticles in QGP.

Contents

1	Introduction	2
2	Molière scattering	6
2.1	Review of a Previous Calculation	6
2.2	Decomposition of the Total Probability	10
3	Phase-Space Constraints and Sampling Kinematic Variables	13
3.1	Phase-Space Constraints	13
3.2	Evaluating the Probability of Elastic Scatterings and Sampling Kinematic Variables	17
4	Incorporating Molière Scatterings in the Hybrid Model	22
4.1	Hybrid Model description of strongly coupled jet-medium interactions	23
4.2	Adding perturbative hard processes within strongly coupled plasma	26
4.3	Monte Carlo implementation within the Hybrid Model	29
5	Results	32
5.1	Jet and single hadron suppression, and introducing results to follow	33
5.2	Two ungroomed observables	34
5.3	Groomed observables	36
5.4	Jets within Jets	40
5.5	Photon-tagged Jet Observables	42
6	Concluding Remarks and a Look Ahead	49
A	Decomposition of Subprocesses	53
B	Evaluating u at $k_T = k_T^{\min}$	55
C	Kinematics of Elastic $2 \rightarrow 2$ Scattering	56
D	Integrals	57
D.1	ϕ Integrals	59
D.2	\tilde{k} Integrals	61
D.3	k_χ^{\min} and x Integrals	67

1 Introduction

When viewed at length scales of order the inverse of its temperature T and longer, quark-gluon plasma (QGP) behaves as a strongly coupled liquid. It has no quasiparticles with mean free paths that are long compared to $1/T$ and flows as a hydrodynamic liquid with a lower specific shear viscosity than that of any other known liquid. Relativistic heavy-ion collisions at RHIC and the LHC produce droplets of this high-temperature phase of QCD matter and have shown it is in fact a strongly coupled liquid [1–5]. However, when it is probed at sufficiently short length scales with sufficiently high momentum transfer, the asymptotic freedom of QCD mandates the presence of quark-like and gluon-like quasiparticles. This raises a guiding question: How does this strongly coupled liquid emerge from an asymptotically free gauge theory?

A natural method of answering this question is to perform scattering experiments with sufficiently large momentum transfer so that the microscopic, particulate structure of QGP is resolved. High-energy partons within jets produced in a heavy-ion collision can trigger such high momentum-exchanges with the quark- and gluon-like quasiparticles in the droplet of QGP formed in the same collision. This makes jets a particularly compelling probe to access detailed information about the microscopic structure of QGP.

Hard scatterings between partons in the incident nuclei produce two or more quarks, antiquarks or gluons with high virtuality. In the absence of a droplet of QGP (aka in vacuum), each high-virtuality parton relaxes its virtuality down to the QCD confinement scale via successive splittings. This produces a shower of partons within some irregular cone in momentum space around the direction of the initial high-virtuality parton. This shower of partons is called a jet. The production and subsequent evolution of a jet in vacuum is theoretically well described by the high-virtuality, perturbative DGLAP evolution equations. However, the evolution of a jet through a droplet of expanding, flowing, and cooling QGP formed in a heavy-ion collision is more complicated. As the high-energy partons within a jet plow through the droplet of QGP, they undergo strong interactions with the strongly coupled colored liquid or, possibly, with the colored quasiparticles that can be resolved within it at short length scales. Such interactions modify the parton shower, and consequently the energy and structure of the measured jet. The modifications to the energy and structure of jets as a result of their interactions with the droplet of QGP is colloquially referred to as *jet quenching* [6–17]. In this paper, we shall focus on one aspect of the interaction between a parton shower and QGP: $2 \rightarrow 2$ elastic scatterings between high-energy jet-partons and thermal quasiparticles in the medium. Elastic scattering with sufficiently high momentum transfer can be described perturbatively. Later in this Introduction, and at greater length in Section 4, we shall also describe the jet quenching dynamics that results from strongly coupled interactions between jet partons and the strongly coupled liquid QGP through which they propagate, as a result of which the jet partons lose energy, accumulate soft transverse momentum and excite wakes in the droplet of QGP.

The short-distance, particulate structure of QGP can be resolved when a high-energy jet-parton scatters off a thermal parton in a droplet of it. If QGP were a liquid at all length scales with no particulate constituents at any length scales, then the probability that an

energetic parton plowing through it is deflected with some momentum q_{\perp} perpendicular to its initial direction of motion is a Gaussian distribution in q_{\perp} [18–21]. So, at sufficiently small values of q_{\perp} the distribution of transverse momentum broadening experienced by a jet-parton will be Gaussian. This soft, Gaussian, strongly coupled transverse momentum broadening falls off rapidly at large q_{\perp} . However, because QCD is asymptotically free this cannot be the whole story. QGP is not a strongly coupled liquid at all scales: it must be particulate at short length-scales. Thus, large angle, high momentum-transfer $2 \rightarrow 2$ scatterings of jet-partons with thermal partons in the medium may be rare, but they will not be Gaussianly rare. Experimental measurements of such large angle, high momentum, deflections of jet-partons — referred to as *Molière scatterings* after the person who first discussed the QED analogue [22–24] — are the first steps to studying the microscopic structure of QGP and to understanding how a strongly coupled QCD liquid emerges from an asymptotically free gauge theory.

In this paper, we develop a concrete framework for incorporating Molière scatterings into a realistic model of jet quenching and explore how their presence modifies a broad set of jet observables. Our goal is twofold: first, to embed perturbative elastic $2 \rightarrow 2$ scattering processes consistently within the hybrid strong/weak coupling model (or simply the Hybrid Model) of jet quenching [25–35], which already captures nonperturbative energy loss, soft momentum broadening, and the effects of jet wakes that all arise from strongly coupled interactions between jet partons and QGP; and, second, to identify jet observables that are sensitive to Molière scatterings off thermal partons in the medium. By doing so, we aim to assess how current and future measurements of jets and jet substructure can meaningfully constrain the short-distance, quasiparticle structure of QGP.

We shall implement Molière scatterings in the Hybrid Model, which is a theoretical framework for jet quenching designed to describe the multi-scale processes of jet production and evolution through strongly coupled plasma. Processes that can be described by weakly coupled QCD are described as such, while processes that are intrinsically strongly coupled are also described appropriately. It treats jet production and hard evolution perturbatively while modeling the soft momentum exchanges between partons in a jet shower and the droplet of QGP using insights from holographic calculations derived rigorously in a strongly coupled gauge theory. Each parton in a jet shower loses energy to the plasma via a holographically derived formula [36, 37] implemented in Refs. [25–35]. The interaction strength is governed by the dimensionless parameter κ_{sc} ; for illustration, a parton with initial energy E_{in} thermalizes over a distance $x_{\text{stop}} = E_{\text{in}}^{1/3}/(2\kappa_{\text{sc}}T^{4/3})$ if it does not split first. κ_{sc} can be calculated in the strongly coupled gauge theory where the energy loss formula was derived; fitting Hybrid Model predictions to data [29] shows that κ_{sc} is smaller by a factor of 3 to 4 in QCD. Jet-induced wakes are computed by perturbing the stress–energy tensor of the hydrodynamic droplet and converting the perturbation into soft hadrons via the Cooper–Frye prescription, assuming a hydrodynamic wake and a small perturbation to the hadron spectra [27, 32, 33, 38]. New observables have been proposed to isolate measurable signatures of jet wakes [32, 33]. The Hybrid Model incorporates soft, Gaussian-distributed transfers of momentum transverse to the jet parton’s direction of motion, describing the frequent (continuous in the strong coupling limit) back-and-forth

exchanges between the jet parton and the medium [27]. However, prior to this study the Hybrid Model has not included rare, perturbative, high momentum transfer Molière $2 \rightarrow 2$ scattering between jet partons and weakly coupled quasiparticles resolved in QGP at short length-scales. An early and incomplete version of this study was reported in Ref. [31].

We begin in Section 2 by reviewing perturbative calculations of Molière scattering probabilities for energetic partons traversing a thermal medium, following and adapting earlier work in Ref. [39]. In particular, we review a calculation [39] of the probability of finding an outgoing hard parton with energy p and angle θ relative to the direction of the incident hard jet-parton after a $2 \rightarrow 2$ scattering has occurred. While the calculation of this probability in Ref. [39] assumed that only one parton in the final state is observed, we extend it to a formulation in which both outgoing partons are explicitly tracked, as is required for a realistic implementation within a description of jet quenching since after the scattering both outgoing partons should be considered jet partons, as both will subsequently lose energy, excite wakes in the QGP, and may scatter again.

Next, in Section 3, we specify the region of phase space over which a perturbative description of Molière scatterings is reasonably valid. In particular, we require the momentum transfer squared of a scattering $cd \rightarrow ab$ (for partons a , b , c , and d) to be greater than a multiple a (we shall typically chose $a = 10$) of the squared Debye mass m_D^2 , namely $|t|, |u| > am_D^2$. We also introduce a set of kinematic variables that will help us to evaluate the probability distributions calculated in Section 2 subject to the constraints $|t|, |u| > am_D^2$. We find that, depending on the value of a , certain ranges of outgoing momentum p and scattering angle θ are disallowed by the constraint $|t| > am_D^2$ and find that the constraint $|u| > am_D^2$ reduces the probability of finding scattered partons in certain other regions of p and θ . To conclude Section 3, we address the practical task of sampling the kinematics of each scattering process $cd \rightarrow ab$ from the probability distributions that we have computed so that Molière scatterings may be included within the Hybrid Model of jet quenching.

In Section 4, we describe how we incorporate the Molière scattering processes evaluated in Sections 2 and 3 into the Hybrid Model. At each timestep of the in-medium evolution of a parton shower, we compute the probability that a hard scattering occurs and, when it does, probabilistically select which subprocess $cd \rightarrow ab$ takes place and choose the corresponding final-state kinematics by sampling from the appropriate probability distributions. The calculation of the total probability with which a Molière scattering occurs, as well as the process by which we sample the kinematics of each scattering, is specified by a set of four integrals, given in Section 3.2. We perform two of the integrations analytically (as described in explicit detail in Appendix D). Although doing so is laborious, the analytic evaluation of two of the four types of integrals provides us with a significant computational advantage, as it means that we only need to evaluate a double integral numerically, not a quadruple integral.

Momentum transfers below the hard-scattering threshold $|t|, |u| < am_D^2$ are not computed perturbatively; instead, their cumulative effect is treated as Gaussian transverse momentum broadening in the Hybrid Model [27], since the transverse momentum distribution of energetic partons propagating through a strongly coupled liquid are Gaussian-

distributed [18, 20, 21]. We choose the magnitude of the soft transverse momentum broadening so as to ensure a smooth matching between its Gaussian distribution and the probability for rare hard Molière scatterings that we have calculated. These Molière scattering and Gaussian transverse momentum broadening effects are embedded in the Hybrid Model alongside its nonperturbative description of strongly coupled energy loss. At each time-step, each jet parton loses energy to, and exchanges soft momentum with, the droplet of QGP and may, with a probability that we compute in this paper, experience a Molière scattering. After a Molière scattering, the two outgoing partons lose energy to the droplet of QGP like any other partons in the jet. That is, we track the energy and momentum deposited by all the jet partons and each recoiling thermal parton after a Molière scattering, and convert all of this “lost” energy and momentum into a hydrodynamic wake in the droplet of QGP which, via the Cooper-Frye prescription at freezeout, becomes soft hadrons in the final state. Including soft jet wakes in the analysis is important to elucidating the consequences of hard Molière scattering for observables because the scattered partons lose energy and produce wakes, in many cases to such a degree that the most significant consequence of a Molière scattering arises from the modification of the shape of the wake of the jet.

In our implementation, we do not include the effects of a finite nonzero medium resolution length L_{res} , defined such that two partons separated by a distance less than L_{res} will interact with the plasma as if they were a single color-charged object, and will interact with the plasma independently if and only if they are separated by a distance greater than L_{res} . The effects of a finite nonzero L_{res} have been implemented and studied in the Hybrid Model in Refs. [28, 34]. In this paper, we treat all partons as if they interact independently with the medium at all times, and leave the analysis of Molière scatterings between multiple unresolved jet-partons and thermal medium-partons [40] to future studies.

In Section 5, we present a systematic study of our implementation of Molière scatterings in the Hybrid Model and how their inclusion impacts a variety of jet observables in PbPb collisions, including the suppression R_{AA} of charged-hadrons and jets, jet shapes and fragmentation functions, the jet girth g , groomed jet observables like the Soft Drop angle R_g and leading k_T , and observables that focus on the number and angular distribution of (sub)jets within jets. We find that, compared to when elastic Molière scatterings are excluded from the Hybrid Model, the presence of elastic scatterings broadens the radial distribution of hadronic energy within jets (i.e. broadens the jet shape and girth) and it broadens the Soft Drop angle R_g of photon-tagged and inclusive jets in PbPb collisions. We confirm that the selection bias intrinsic to selecting jets based upon their own energy can be partially mitigated by selecting gamma-jet events based on the photon energy. In particular, we find that the distributions of both the Soft Drop angle R_g and the girth g of gamma-jets in PbPb collisions broaden due to Molière scatterings as long as jets which are sufficiently softer than the photon are included.

Our analysis in Section 5 of Hybrid Model calculations of both the Soft Drop splitting angle R_g and the jet girth g in photon-tagged $R = 0.2$ jets and $R = 0.6$ jets, in each case considering both samples selected with $x_J \equiv p_T^{\text{jet}}/p_T^\gamma > 0.2$ and $x_J > 0.8$ provides a compelling case study. We find that in samples of $R = 0.2$ photon-tagged jets with

$x_J > 0.2$ recoiling against photons with $p_T^\gamma > 150$ GeV, the broadening of the R_g and g distributions induced by Molière scattering in PbPb collisions relative to those in pp collisions can overcome the narrowing associated with jet selection bias and show that jet wakes make a negligible contribution to these observables in such narrow jets. Comparing the PbPb/pp ratios of these distributions in samples selected with $x_J > 0.8$ and $x_J > 0.2$ serves to quantify the effects of selection bias due to energy loss, and comparing these distributions for jets with $R = 0.6$ and $R = 0.2$ reveals a fascinating interplay between the effects of jet wakes and Molière scattering. Jet wakes make a dominant contribution to the PbPb/pp ratio for both R_g and g in a sample of $R = 0.6$ jet with $x_J > 0.2$, but only to g in a sample of these wide jets with the more restrictive selection $x_J > 0.8$. This provides a roadmap for how experimentalists can use their ability to dial two knobs — the radius R of the jets they reconstruct and the x_J selection criterion for which jets they include in their sample — so as to separately focus on and highlight the effects of selection bias due to energy loss, jet wakes, and Molière scattering. With regards to Molière scattering in particular, we explain how our study, in combination with the existing tantalizing CMS measurements [41] of R_g and g for $R = 0.2$ photon-tagged jets with $p_T^\gamma > 100$ GeV and $x_J > 0.4$, indicates that measurements with a modestly higher photon- p_T that allows for jets with a somewhat lower x_J to be included in the analysis can reveal an enhancement of photon-tagged jets with large R_g and large g in PbPb collisions relative to pp collisions. This would be a distinctive model-independent experimental signature of hard scattering of jet partons off quasiparticles in QGP, and would open the door to studying the microscopic particulate nature of QGP and seeing how a strongly coupled QCD liquid emerges from an asymptotically free gauge theory. We conclude and look ahead, in particular towards the importance of making such measurements in oxygen-oxygen collisions, in Section 6.

2 Molière scattering

Motivated by the tantalizing possibility that large angle, large momentum-transfer, elastic scatterings between jet partons and thermal quasiparticles can reveal the short-distance structure of QGP, we now turn to a quantitative description of these scattering processes. In this section, we review and adapt earlier work in Ref. [39] on the perturbative framework needed to compute the differential probabilities with which such Molière scatterings occur. Our goal here is to establish notation and define the kinematic variables, and probability distributions that will later allow us to consistently incorporate elastic $2 \rightarrow 2$ scatterings into the Hybrid Model.

2.1 Review of a Previous Calculation

When viewed at length scales of order the inverse of its temperature T and longer, quark-gluon plasma (QGP) behaves as a strongly coupled liquid. It has no quasiparticles with mean free paths that are long compared to $1/T$ and flows as hydrodynamic liquid with a lower specific shear viscosity than that of any other known liquid. However, when it is probed at shorter length scales with sufficiently high momentum transfer, the asymptotic freedom of QCD mandates the presence of quark-like and gluon-like quasiparticles. High

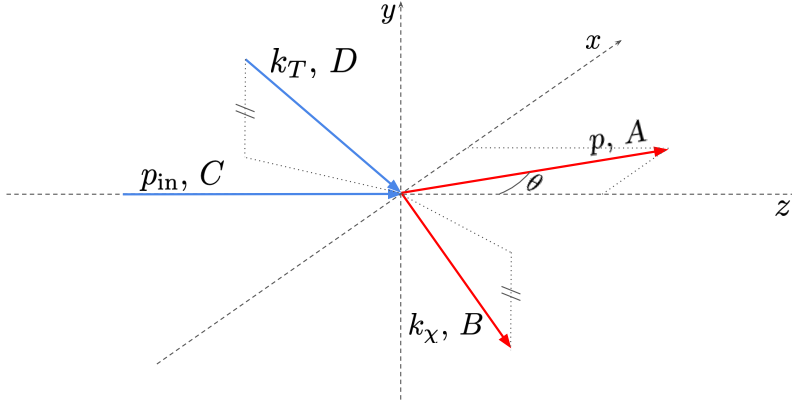


Figure 1: Schematic of a $2 \rightarrow 2$ Molière scattering process, where an incoming particle of type C with momentum p_{in} in the $+\hat{z}$ direction scatters off a thermal particle of type D with momentum k_T . The outgoing particle of type A has momentum p and scatters in the (z, x) plane at an angle θ relative to the direction of propagation of the incoming hard parton. The other outgoing parton of type B has momentum k_χ and scatters at an angle which can be determined using energy-momentum conservation. For example, momentum conservation means that k_χ has the same \hat{y} component as k_T , as indicated in the diagram. A , B , C , and D can each be a gluon, quark, or antiquark.

energy partons within jets can trigger such exchanges, revealing the particulate structure of QGP. Such large-angle, high-momentum transfer, $2 \rightarrow 2$ elastic scatterings between high energy partons in a jet and quasiparticles in the medium are rare but not exponentially rare. Fig. 1 shows a schematic of what a Molière scattering process looks like. It is a high momentum transfer scattering between an incident parton with momentum p_{in} and a target thermal parton from the QGP medium with momentum k_T (where the subscript T refers to the word “thermal”, not “transverse”) that produces two outgoing partons with momenta p and k_χ . Each of the partons can be a gluon, quark, or antiquark. We shall treat the quarks and antiquarks as massless. Note that the two outgoing partons can each be either the deflected incident parton or the recoiling QGP parton after it has been kicked. The calculation of the probability that an incident parton with momentum p_{in} experiences a Molière scattering that yields an outgoing parton with momentum p at an angle θ was set up in Refs. [21, 39]. In this Section, we review the results of Ref. [39].

We adopt the notation used in Ref. [39] to denote different parton species with lower case letters (i.e. $a = u, \bar{u}, d, \bar{d}, s, \bar{s}, g$) and to denote different types of partons, like gluons, quarks, and antiquarks using uppercase indices (i.e. $A = G, Q, \bar{Q}$). For a $2 \rightarrow 2$ Molière scattering like that shown in Fig. 1, $F^{C \rightarrow A}(p, \theta; p_{\text{in}})$ denotes the probability of finding an outgoing parton of type A with energy p at angle θ with respect to the direction of an incoming parton of type C with energy p_{in} . The leading order perturbative QCD calculation of $F^{C \rightarrow A}(p, \theta; p_{\text{in}})$ is introduced and described in Ref. [39].

To implement Molière scatterings in the Hybrid Model, two steps are required. First, at each time step in the evolution of a parton shower, for each parton in the shower at

that time, we need to calculate the probability that a Molière scattering occurs. This can be done by integrating $F^{C \rightarrow A}(p, \theta; p_{\text{in}})$ over the variables p and θ . Second, if any Molière scatterings occur, we then need to determine which type of $2 \rightarrow 2$ scattering process takes place (e.g. $qq \rightarrow qq, q\bar{q} \rightarrow gg$, etc.) and what the momenta are of the two outgoing partons. In Section 3, we shall describe how we accomplish these two steps and then in Section 4 we shall implement them in the Hybrid Model.

Before we move forward with any computations, it is useful to review some key details about the calculation of $F^{C \rightarrow A}(p, \theta; p_{\text{in}})$ as presented in Ref. [39]; this is our goal in this Section. Suppose that $f_a(p, \theta, t)$ denotes the probability of finding a parton of species a in a phase-space cell at angle θ (relative to the incident parton) with energy p at time t . So, if a parton enters a static brick of QGP at time $t = t_I$ with energy p_I , then $f_a(p, \theta, t_I) = 0$ for all values of $p \neq p_I$ and $\theta \neq 0$. Assume that this incident parton propagates through the plasma for a time Δt . Then, $f_a(p, \theta, t_I + \Delta t)$ is a phase space distribution function for an outgoing parton of species a that can be nonzero for $p \neq p_I$ and $\theta \neq 0$.

One can then write the probability distribution function $F^{C \rightarrow A}(p, \theta; p_{\text{in}})$ as a sum over all possible processes with C in the initial state and A in the final state

$$F^{C \rightarrow A}(p, \theta; p_{\text{in}}) = V \frac{p^2 \sin(\theta)}{(2\pi)^2} \sum_{a \in A} \nu_a f_a(p, \theta, t_I + \Delta t), \quad (2.1)$$

where the prefactor in front is the Jacobian of the phase space integration and ν_a is a degeneracy factor that accounts for helicity and color configurations. In particular, $\nu_a = 2(N_c^2 - 1)$ if a is a gluon and $\nu_a = 2(N_c - 1)$ if a is a quark or antiquark. The probability of finding a parton of any type with momentum p and angle θ in the final state is then obtained by summing over all possible A :

$$F^{C \rightarrow \text{all}}(p, \theta) = F^{C \rightarrow G}(p, \theta) + F^{C \rightarrow Q}(p, \theta) + F^{C \rightarrow \bar{Q}}(p, \theta). \quad (2.2)$$

Suppose that we wish to consider an elastic $2 \rightarrow 2$ scattering process $cd \rightarrow ab$. We further assume that both the partons a and b are detected in the final state; this differs from the assumption in Ref. [39], where only the parton a is detected in the final state and the parton b is undetected. After examining the form of $f_a(p, \theta, t_I + \Delta t)$ in Eq. (2.4) of Ref. [39] and noting the difference described in the preceding sentence, $F^{C \rightarrow A}(p, \theta; p_{\text{in}})$ is given by the expression

$$\begin{aligned} F^{C \rightarrow A}(p, \theta; p_{\text{in}}) &= V \frac{\kappa p^2 \sin \theta}{T (2\pi)^2} \sum_n w_C^{(n)} \frac{\tilde{\delta}_{a,A}}{1 + \delta_{cd}} \int_{\mathbf{p}', \mathbf{k}', \mathbf{k}} \frac{|\mathcal{M}_{ab \leftrightarrow cd}^{(n)}|^2}{g_s^4} \\ &\times \frac{1}{\nu_C} \left[\tilde{\delta}_{d,C} f_I(\mathbf{k}') n_c(\mathbf{p}') + \tilde{\delta}_{c,C} f_I(\mathbf{p}') n_d(\mathbf{k}') \right] \\ &\times [1 \pm n_a(\mathbf{p})] [1 \pm n_b(\mathbf{k})], \end{aligned} \quad (2.3)$$

where $\kappa \equiv g_s^4 T \Delta t$ is a dimensionless parameter that depends on the thickness Δt of the QGP brick and the strength of the QCD coupling g_s ,

$$f_I(\mathbf{p}) \equiv \nu_a f_a(\mathbf{p}, t_I) = \frac{1}{V} \frac{4\pi^2}{p_{\text{in}}^2} \delta(p - p_{\text{in}}) \delta(\cos \theta - \cos \theta_{\text{in}}), \quad (2.4)$$

(n)	Process	$ \mathcal{M}^{(n)} ^2/g_s^4$	$w_Q^{(n)}$	$w_{\bar{Q}}^{(n)}$	$w_G^{(n)}$
1	$qq \leftrightarrow qq$	$8 \frac{d_F^2 C_F^2}{d_A} \left(\frac{s^2+u^2}{t^2} + \frac{s^2+t^2}{u^2} \right) + 16 d_F C_F \left(C_F - \frac{C_A}{2} \right) \frac{s^2}{tu}$	1	0	0
2	$\bar{q}\bar{q} \leftrightarrow \bar{q}\bar{q}$	$ \mathcal{M}^{(1)} ^2/g_s^4$	0	1	0
3	$q\bar{q} \leftrightarrow q\bar{q}$	$8 \frac{d_F^2 C_F^2}{d_A} \left(\frac{s^2+u^2}{t^2} + \frac{t^2+u^2}{s^2} \right) + 16 d_F C_F \left(C_F - \frac{C_A}{2} \right) \frac{u^2}{st}$	1	1	0
4	$qq' \leftrightarrow qq'$	$8 \frac{d_F^2 C_F^2}{d_A} \left(\frac{s^2+u^2}{t^2} \right)$	$N_f - 1$	0	0
5	$\bar{q}\bar{q}' \leftrightarrow \bar{q}\bar{q}'$	$ \mathcal{M}^{(4)} ^2/g_s^4$	0	$N_f - 1$	0
6	$q\bar{q}' \leftrightarrow q\bar{q}'$	$ \mathcal{M}^{(4)} ^2/g_s^4$	$N_f - 1$	$N_f - 1$	0
7	$q\bar{q} \leftrightarrow q'\bar{q}'$	$8 \frac{d_F^2 C_F^2}{d_A} \left(\frac{t^2+u^2}{s^2} \right)$	$N_f - 1$	$N_f - 1$	0
8	$q\bar{q} \leftrightarrow gg$	$8 d_F C_F^2 \left(\frac{t^2+u^2}{tu} \right) - 8 d_F C_F C_A \left(\frac{t^2+u^2}{s^2} \right)$	1	1	N_f
9	$qq \leftrightarrow qq$	$-8 d_F C_F^2 \left(\frac{u}{s} + \frac{s}{u} \right) + 8 d_F C_F C_A \left(\frac{s^2+u^2}{t^2} \right)$	1	0	N_f
10	$\bar{q}\bar{q} \leftrightarrow \bar{q}\bar{q}$	$ \mathcal{M}^{(9)} ^2/g_s^4$	0	1	N_f
11	$gg \leftrightarrow gg$	$16 d_A C_A^2 \left(3 - \frac{su}{t^2} - \frac{st}{u^2} - \frac{tu}{s^2} \right)$	0	0	1

Table 1: List of the binary collision processes labeled by (n) that can produce a hard parton in the final state with large transverse momentum with respect to the incoming probe. Here, q and q' are quarks of distinct flavors, \bar{q} and \bar{q}' the associated antiquarks, and g is a gluon. The third column lists explicit leading order perturbative QCD expressions for the corresponding squared matrix elements, in vacuum, summed over initial *and final* polarizations and colors, as a function of the Mandelstam variables $t = -2(p'p - \mathbf{p}' \cdot \mathbf{p})$, $u = -2(p'k - \mathbf{p}' \cdot \mathbf{k})$ and $s = -t - u$. (See Ref. [42].) In an $SU(N_c)$ theory with fermions in the fundamental representation, we have for the dimensions of the representations and the Casimir factors $d_F = C_A = N_c$, $C_F = (N_c^2 - 1)/(2N_c)$, and $d_A = 2 d_F C_F = N_c^2 - 1$. For $SU(3)$ (i.e. QCD), $d_F = C_A = 3$, $C_F = 4/3$, and $d_A = 8$. Finally, we give the degeneracy factors $w_C^{(n)}$ appearing in Eq. (2.3). Here, N_f is the number of light flavors; we take $N_f = 3$ throughout.

where we have already chosen $\theta_{\text{in}} = 0$, $\tilde{\delta}_{a,A}$ is a generalized Kronecker delta which equals 1 if $a \in A$ and is 0 otherwise, n_a is the generalized medium “soft” distribution function

$$n_a(p) = \frac{\tilde{\delta}_{a,G}}{e^{p/T} - 1} + \frac{\tilde{\delta}_{a,Q} + \tilde{\delta}_{a,\bar{Q}}}{e^{p/T} + 1}, \quad (2.5)$$

n_b , n_c and n_d are defined analogously, and $|\mathcal{M}_{ab \leftrightarrow cd}^{(n)}|^2/g_s^4$ is the leading order expression for the corresponding QCD squared matrix element for the different binary collision processes $ab \leftrightarrow cd$ of type (n) in vacuum, summed over initial and final polarizations and colors. The different binary collision processes, these matrix elements, and their associated degeneracy factors $w_C^{(n)}$ are listed in Table 1.

Throughout this work, we shall assume that the momentum distributions of partons

from the QGP medium are given simply by Eq. (2.5) and the matrix elements are given simply by the leading order perturbative QCD expressions in Table 1. The first of these assumptions must be questioned, as QGP is strongly coupled, but it suffices for our purposes of identifying experimental observables that are well-suited for revealing and, ideally, isolating the effects of Molière scattering. We leave investigating more sophisticated forms for $n_a(p)$ to future work. Ideally, future experimental measurements that succeed in isolating effects of Molière scattering may one day be used to infer constraints on the form of $n_a(p)$ in strongly coupled QGP. The second of these assumptions may also be questioned, but we are less concerned about it since we shall only consider elastic scattering processes in which the squared momentum transfer is larger than the squared Debye mass by at least a factor of 10, which provides some justification for assuming weak coupling.

The expression on the right-hand side of Eq. (2.3) for a scattering process $cd \rightarrow ab$, can be understood as follows. As in Ref. [39], our convention is that the outgoing parton a in the final state comes from the parton c in the initial state, and the outgoing parton b in the final state comes from the parton d in the initial state. So, the term $\tilde{\delta}_{c,C} f_I(\mathbf{p}') n_d(\mathbf{k}')$ corresponds to the case where the outgoing parton a came from the incident parton c , and the outgoing parton b came from the thermal medium parton d after it was kicked by the incident parton c , as illustrated in Fig. 1. Conversely, the term $\tilde{\delta}_{d,C} f_I(\mathbf{k}') n_c(\mathbf{p}')$ corresponds to the case when the outgoing hard parton a originates from the thermal medium parton c after having been kicked by the incident parton d , which is deflected and sources the outgoing parton b . The Kronecker delta $\delta_{c,d}$ accounts for when c and d are identical. The modified Kronecker delta $\tilde{\delta}_{a,A}$ ensures that only final state partons a of type A contribute to the total probability $F^{C \rightarrow A}$. Finally, the sum runs over all possible binary collision processes $cd \rightarrow ab$, with $\mathbf{p}', \mathbf{k}', \mathbf{p}, \mathbf{k}$ representing the momenta of c, d, a, b , respectively. The phase space integral is written in the compact form

$$\int_{\mathbf{p}', \mathbf{k}', \mathbf{k}} \equiv \frac{1}{2p} \int \frac{d^3 \mathbf{k}}{2k(2\pi)^3} \int \frac{d^3 \mathbf{p}'}{2p'(2\pi)^3} \int \frac{d^3 \mathbf{k}'}{2k'(2\pi)^3} \times (2\pi)^4 \delta^{(3)}(\mathbf{p} + \mathbf{k} - \mathbf{p}' - \mathbf{k}') \delta(p + k - p' - k'). \quad (2.6)$$

2.2 Decomposition of the Total Probability

The sum over n in Eq. (2.3) runs over all 11 processes in Table 1. $F^{C \rightarrow A}(p, \theta; p_{\text{in}})$ may therefore be decomposed into the partial contributions from each of the 11 binary collision processes for a scattering $cd \rightarrow ab$:

$$F^{C \rightarrow A}(p, \theta; p_{\text{in}}) \equiv \sum_n F_{(n)}^{C \rightarrow A}(p, \theta; p_{\text{in}}). \quad (2.7)$$

Following Section 2.5 of Ref. [39], each partial contribution $F_{(n)}^{C \rightarrow A}(p, \theta; p_{\text{in}})$ is given by a linear combination of two phase space integrals:

$$\langle (n) \rangle_{D,B} \equiv \frac{1}{T} \frac{[1 \pm n_A(p)] p^2 \sin \theta}{(2\pi)^2} \int_{\mathbf{p}', \mathbf{k}', \mathbf{k}} \frac{|\mathcal{M}^{(n)}|^2}{g_s^4} f_I(\mathbf{p}') n_D(\mathbf{k}') [1 \pm n_B(k)], \quad (2.8)$$

$$\langle (\tilde{n}) \rangle_{D,B} \equiv \frac{1}{T} \frac{[1 \pm n_A(p)] p^2 \sin \theta}{(2\pi)^2} \int_{\mathbf{p}', \mathbf{k}', \mathbf{k}} \frac{|\mathcal{M}_{t \leftrightarrow u}^{(\tilde{n})}|^2}{g_s^4} f_I(\mathbf{k}') n_D(\mathbf{p}') [1 \pm n_B(k)], \quad (2.9)$$

where uppercase indices A, B, C, D denote whether the outgoing partons of type A and B and the incoming partons of type C and D are quarks, antiquarks, or gluons and where we shall explain the $t \leftrightarrow u$ notation further below. The factors $[1 \pm n_A]$ and $[1 \pm n_B]$ (the sign is $+$ if A or B is a boson and $-$ if A or B is a fermion) describe Bose enhancement or Pauli blocking and depend on the occupation of the mode in which the outgoing particles A or B in the final state are produced. Note that in the limit of high outgoing momentum p for final state particle a , the Pauli blocking factor $[1 \pm n_A] \approx 1$ and we recover Eqs. (2.15a) and (2.15b) of Ref. [39]. In the present work, we restrict to hard scattering processes with high momentum *transfer*, but do not require the momenta of any particles to be high. One can use Eqs. (2.8) and (2.9) and Table 1 to write expressions for all possible $F^{C \rightarrow A}(p, \theta; p_{\text{in}})$:

$$F^{Q \rightarrow Q}(p, \theta; p_{\text{in}}) = \frac{\kappa}{\nu_q} \left\{ \frac{1}{2} \langle (1) \rangle_{Q,Q} + \frac{1}{2} \langle (\tilde{1}) \rangle_{Q,Q} + \langle (3) \rangle_{Q,Q} + \langle (9) \rangle_{G,G} \right. \\ \left. + (N_f - 1) \left[\langle (4) \rangle_{Q,Q} + \langle (\tilde{4}) \rangle_{Q,Q} + \langle (6) \rangle_{Q,Q} + \langle (7) \rangle_{\bar{Q},\bar{Q}} \right] \right\}, \quad (2.10)$$

$$F^{Q \rightarrow G}(p, \theta; p_{\text{in}}) = \frac{\kappa}{\nu_q} \left\{ \langle (8) \rangle_{Q,G} + \langle (\tilde{8}) \rangle_{Q,G} + \langle (\tilde{9}) \rangle_{G,Q} \right\}, \quad (2.11)$$

$$F^{Q \rightarrow \bar{Q}}(p, \theta; p_{\text{in}}) = \frac{\kappa}{\nu_q} \left\{ \langle (\tilde{3}) \rangle_{Q,Q} + (N_f - 1) \left[\langle (\tilde{6}) \rangle_{Q,Q} + \langle (\tilde{7}) \rangle_{Q,Q} \right] \right\}, \quad (2.12)$$

$$F^{G \rightarrow Q}(p, \theta; p_{\text{in}}) = \frac{\kappa}{\nu_g} N_f \left\{ \langle (8) \rangle_{G,Q} + \langle (\tilde{9}) \rangle_{Q,G} \right\}, \quad (2.13)$$

$$F^{G \rightarrow G}(p, \theta; p_{\text{in}}) = \frac{\kappa}{\nu_g} \left\{ N_f \left[\langle (9) \rangle_{Q,Q} + \langle (10) \rangle_{Q,Q} \right] + \frac{1}{2} \langle (11) \rangle_{G,G} + \frac{1}{2} \langle (\tilde{11}) \rangle_{G,G} \right\}, \quad (2.14)$$

$$F^{G \rightarrow \bar{Q}}(p, \theta; p_{\text{in}}) = \frac{\kappa}{\nu_g} N_f \left\{ \langle (8) \rangle_{G,Q} + \langle (\tilde{10}) \rangle_{Q,G} \right\}. \quad (2.15)$$

Next, we recast Eqs. (2.8) and (2.9) into forms suitable for analytic and numerical evaluation. To this end, let $\omega \equiv p_{\text{in}} - p$ and $\mathbf{q} \equiv \mathbf{p} - \mathbf{p}_{\text{in}}$ denote the energy and momentum difference, respectively, between the incident parton and the outgoing parton a . Then, the momentum transfer is $Q^\mu = (\omega, \mathbf{q})$. Then, upon defining

$$q \equiv |\mathbf{q}| = \sqrt{p_{\text{in}}^2 + p^2 - 2pp_{\text{in}} \cos \theta}, \quad (2.16)$$

energy-momentum conservation requires the incoming thermal parton to have an energy of at least $k_T^{\text{min}} = (q - \omega)/2$. Furthermore, we denote the 4-momentum of the thermal parton from the medium involved in the elastic scattering by (k_T, \mathbf{k}_T) and note that the four-momentum of the outgoing parton b is given by $(k_\chi, \mathbf{k}_\chi)$ with $k_\chi = k_T + \omega$ and $\mathbf{k}_\chi = \mathbf{k}_T + \mathbf{q}$. (In our phase space integration, both $\mathbf{k}' = \mathbf{k}_T$ and $\mathbf{p}' = \mathbf{k}_T$ will contribute; similarly, both $\mathbf{p} = \mathbf{k}_\chi$ and $\mathbf{k} = \mathbf{k}_\chi$ will contribute.)

Given all this, one can reformulate Eq. (2.8) as

$$\langle(n)\rangle_{D,B} = \frac{[1 \pm n_A(p)]}{16(2\pi)^3} \left(\frac{p \sin \theta}{p_{\text{in}} q T} \right) \int_{k_{\text{min}}}^{\infty} dk_T n_D(k_T) [1 \pm n_B(k_\chi)] \int_0^{2\pi} \frac{d\phi}{2\pi} \frac{|\mathcal{M}^{(n)}|^2}{g_s^4}, \quad (2.17)$$

where ϕ is the angle between the two planes identified by the pair of vectors (\mathbf{p}, \mathbf{q}) and $(\mathbf{q}, \mathbf{k}_T)$, and $\mathcal{M}^{(n)}$ are the QCD matrix elements that appear in Table 1. These matrix elements are functions of the Mandelstam variables t and u . Following Ref. [39], we define the quantities t , u and s as

$$\begin{aligned} t &\equiv \omega^2 - q^2 = -2p p_{\text{in}}(1 - \cos(\theta)), \\ u &\equiv -s - t, \\ s &\equiv \left(-\frac{t}{2q^2} \right) \left\{ [(p_{\text{in}} + p)(k_T + k_\chi) + q^2] - \sqrt{(4p_{\text{in}}p + t)(4k_T k_\chi + t)} \cos \phi \right\}. \end{aligned} \quad (2.18)$$

These are the Mandelstam variables in the matrix elements $\mathcal{M}^{(n)}$ in Eq. (2.8), but in the matrix elements $\mathcal{M}_{t \leftrightarrow u}^{(n)}$ in Eq. (2.9) the quantity t (u) defined in Eq. (2.18) plays the role of the Mandelstam variable u (t) — hence the subscript $t \leftrightarrow u$ in Eq. (2.9). Thus,

$$\langle(\tilde{n})\rangle_{D,B} = \frac{[1 \pm n_A(p)]}{16(2\pi)^3} \left(\frac{p \sin \theta}{p_{\text{in}} q T} \right) \int_{k_{\text{min}}}^{\infty} dk_T n_D(k_T) [1 \pm n_B(k_\chi)] \int_0^{2\pi} \frac{d\phi}{2\pi} \frac{|\mathcal{M}_{t \leftrightarrow u}^{(n)}|^2}{g_s^4}. \quad (2.19)$$

The phase space integrals $\langle(n)\rangle_{D,B}$ and $\langle(\tilde{n})\rangle_{D,B}$ for $n = 1, \dots, 11$ are functions of θ and p .

Recall that implementing elastic $2 \rightarrow 2$ scatterings within a framework of jet quenching requires two steps: determining whether or not such a scattering has occurred, and then determining which process $cd \rightarrow ab$ occurred with what momenta for the partons a and b after the elastic scattering. The first of these two steps requires that we integrate our probability $F^{C \rightarrow A}(p, \theta; p_{\text{in}})$ over all allowed values of angle θ and outgoing momentum p . This amounts to performing a total of four integrals, over ϕ , k_T , θ and p .

Finally, following Ref. [39] we observe that $|\mathcal{M}^{(n)}(t, u)|^2$ and $|\mathcal{M}^{(\tilde{n})}(u, t)|^2$ can be decomposed into a linear combination of 7 terms m_i :

$$\frac{1}{g_s^4} \left| \mathcal{M}^{(n)}(t, u) \right|^2 = \sum_i c_i^{(n)} m_i(t, u), \quad \frac{1}{g_s^4} \left| \mathcal{M}^{(\tilde{n})}(u, t) \right|^2 = \sum_i \tilde{c}_i^{(\tilde{n})} m_i(t, u), \quad (2.20)$$

where the 7 terms m_i in question are

$$\begin{aligned} m_1 &= \left(\frac{s}{t} \right)^2, \quad m_2 = -\left(\frac{s}{t} \right), \quad m_3 = 1, \quad m_4 = -\left(\frac{t}{s} \right), \quad m_5 = \left(\frac{t}{s} \right)^2, \\ m_6 &= -\left(\frac{t}{s+t} \right) = \frac{t}{u}, \quad m_7 = \left(\frac{t}{s+t} \right)^2 = \left(\frac{t}{u} \right)^2. \end{aligned} \quad (2.21)$$

The coefficients $c_i^{(n)}$ and $\tilde{c}_i^{(\tilde{n})}$ can be determined from Table 1 and are given explicitly in Appendix A. Since the coefficients $c_i^{(n)}$ and $\tilde{c}_i^{(\tilde{n})}$ only depend on N_c , we may write $\langle(n)\rangle_{D,B}$ as

$$\langle(n)\rangle_{D,B} = \sum_{i=1}^7 c_i^{(n)} \langle m_i(t, u) \rangle, \quad (2.22)$$

where $\langle m_i(t, u) \rangle$ is defined as

$$\langle m_i(t, u) \rangle \equiv \frac{[1 \pm n_A(p)]}{16(2\pi)^3} \left(\frac{p \sin \theta}{p_{\text{in}} q T} \right) \int_{k_{\text{min}}}^{\infty} dk_T n_D(k_T) [1 \pm n_B(k_\chi)] \int_0^{2\pi} \frac{d\phi}{2\pi} m_i(t, u). \quad (2.23)$$

This concludes our review of the calculation as formulated in Ref. [39], with small adaptations for the purposes of our work that we have described along the way.

3 Phase-Space Constraints and Sampling Kinematic Variables

Before we can embed the $2 \rightarrow 2$ elastic scattering processes described in the previous Section into a Monte Carlo model of jet showers in heavy ion collisions, we must define the portion of phase space where a perturbative description of elastic scatterings with *high momentum exchange* is trustworthy and, conversely, excise the soft sector where the shower partons and the QGP are strongly coupled. In the Hybrid Model, making this excision can also be understood as avoiding double counting. The Hybrid Model implementation of energy loss is based upon a strongly coupled calculation in which there is no distinction between elastic and radiative energy loss processes. By fitting the Hybrid Model parameter κ_{sc} that controls the energy loss of jet partons to experimental data we are already incorporating effects that might alternatively be described as elastic scattering with soft momentum exchange. Here, therefore, we need to ensure that what we are adding to the Hybrid Model is only elastic scattering where the exchanged momentum is above a threshold that we must choose. We shall require that the exchanged momentum, squared, is greater than am_D^2 , where we shall take the Debye mass squared to be $m_D^2 = \frac{1}{3}g_s^2 T^2 (N_c + N_f/2) = \frac{3}{2}g_s^2 T^2$. Throughout this paper, we shall choose $a = 10$ unless otherwise noted. The QCD coupling g_s that sets the magnitude of the matrix elements in Table 1 as well as the Debye mass and the threshold parameter a that defines how large the momentum transfer must be in elastic scattering processes that we are adding to the Hybrid Model are the two new Hybrid Model parameters that we introduce in this study.

In Section 3.1 below, we provide an explicit description of how we impose the phase-space constraints corresponding to keeping only those elastic scattering processes with exchanged momentum squared greater than am_D^2 . Having identified the kinematic constraints that isolate hard, perturbative, elastic scatterings, we turn to the practical question of how to integrate over the allowed phase space in order to determine the probability that such an elastic scattering occurs as well as how to sample the allowed phase space with the appropriate probability distribution. In Sec. 3.2, we describe a Monte Carlo procedure for generating elastic scattering events according to the differential probabilities derived in Sec. 2, while consistently enforcing the phase-space restrictions discussed in Sec. 3.1. This step is essential for embedding Molière scatterings into a dynamical jet-quenching model such as the Hybrid Model.

3.1 Phase-Space Constraints

Following Ref. [39], we shall require that the square of the four momentum difference between the incident parton and each of the two outgoing partons must be larger than

am_D^2 . That is, we shall require that

$$|\tilde{t}| = 2p_{\text{in}}p(1 - \cos\theta) > am_D^2, \quad (3.1)$$

and

$$|\tilde{u}| = 2(p_{\text{in}}k_\chi - \mathbf{p}_{\text{in}} \cdot \mathbf{k}_\chi) > am_D^2. \quad (3.2)$$

The two constraints in Eqs. (3.1) and (3.2) serve together to eliminate the phase space corresponding to low momentum exchange processes.

The constraint on $|t|$ in Eq. (3.1) is easy to impose as it is directly expressed as a constraint on p and θ , cutting off the region where either is too close to zero. In Fig. 2 (presented and described in Section 3.2), this excision corresponds to the black excluded regions along the p and θ axes.

The constraint on $|u|$ in Eq. (3.2) requires further examination, because it is not phrased as a constraint on p and θ . For any choice of p and θ , there are some values of the other kinematic variables ϕ and k_T for which $|u|$ satisfies Eq. (3.2) and other values of these kinematic variables that must be excluded because $|u|$ is too small. Two illustrative limits highlight how Eq. (3.2) (together with Eq. (3.1)) constrains the regime of kinematic variables that we must include/exclude. First, we examine the limit in which the momentum k_T of the thermal parton from the QGP involved in the elastic scattering is very small. In Appendix B, we evaluate $|u|$ at the minimum value of k_T allowed by energy and momentum conservation for given specified values of p_{in} , p and θ , namely $k_T = k_T^{\text{min}} = (q - \omega)/2$, obtaining

$$|u(k_T = k_T^{\text{min}})| = \frac{|t|(p - k_T^{\text{min}})}{q} = \frac{2p_{\text{in}}p(1 - \cos(\theta))(p - k_T^{\text{min}})}{q}. \quad (3.3)$$

We then see that if $k_T = k_T^{\text{min}}$ both requirements $|t| > am_D^2$ and $|u| > am_D^2$ are fulfilled at sufficiently high p and θ whereas at small enough p and/or θ one or both can be violated. The second illustrative limit that we examine is a collinear limit where we suppose $k_T = p$. Then,

$$|u(k_T = p)| = \left(\frac{2p_{\text{in}}p \sin(\phi/2) \sin\theta}{q} \right)^2, \quad (3.4)$$

which can become small when $\phi \rightarrow 0$ or $\theta \rightarrow \pi$, as well as when either θ or p is small as before. Hence, for k_T in this regime additional restrictions on ϕ and θ are needed in order to satisfy Eq. (3.2).

Elastic scattering in the regimes where $|t|$ and $|u|$ are small are exactly the regimes of phase space with collinear divergences that would need need to be treated more carefully if we wanted to include such processes. This would entail identifying the regions in the (ϕ, k_T, p, θ) phase space where $|u|$ and $|t|$ are large enough vs. where they are not, and modifying the amplitudes in the latter region according to the prescription from Ref. [42]. As we have already noted, though, doing this would not make sense in the Hybrid Model where we have already incorporated a description of the strongly coupled, soft, exchanges between jet partons and the strongly coupled QGP, which we should not double count. For our purposes, in the regions in (ϕ, k_T, p, θ) phase space where $|u|$ and $|t|$ are large

that describe the large momentum transfer elastic scattering events that are intrinsically weakly coupled that we seek to add to the Hybrid Model we need not modify the scattering amplitudes, and we need to exclude the regions where $|u|$ and/or $|t|$ are $< am_D^2$.

We now describe how we implement the conditions $|u| > am_D^2$ and $|t| > am_D^2$ in the (ϕ, k_T, p, θ) phase space. To save notation, we rewrite Eqs. (2.18) as

$$\tilde{s} = -\tilde{t}(C - D \cos \phi), \quad \tilde{u} = -\tilde{s} - \tilde{t} = \tilde{t}(C_u - D \cos \phi), \quad (3.5)$$

where

$$2q^2 C(p_{\text{in}}, p, q, k_T) \equiv (p_{\text{in}} + p)(k_T + k_\chi) + q^2, \quad (3.6)$$

$$C_u(p_{\text{in}}, p, q, k_T) \equiv C(p_{\text{in}}, p, q, k_T) - 1, \quad (3.7)$$

$$2q^2 D(p_{\text{in}}, p, q, k_T) \equiv \sqrt{(4p_{\text{in}}p + t)(4k_T k_\chi + t)}. \quad (3.8)$$

We also define k_χ^{min} as the minimum value of k_χ allowed by energy and momentum conservation given specified values of p_{in} , p and θ , which can be written as

$$k_\chi^{\text{min}} = \frac{|t|}{4k_T^{\text{min}}} = \frac{|t|}{2(q - \omega)}. \quad (3.9)$$

And, finally, we define the dimensionless quantities $x \equiv am_D^2/|t|$ and $\bar{t} \equiv t/am_D^2 = -1/x$ and introduce the convention that a tilde over a momentum or energy variable makes it dimensionless via dividing by T : $\tilde{p}_{\text{in}} = p_{\text{in}}/T$, $\tilde{p} = p/T$, $\tilde{q} = q/T$, $\tilde{\omega} = \omega/T$, $\tilde{k}_T \equiv k_T/T$, $\tilde{k}_\chi = k_\chi/T$... With these definitions, instead of using the variables (ϕ, k_T, p, θ) we can equivalently describe our phase space using the new variables $\tilde{k} \equiv \tilde{k}_T - \tilde{k}_T^{\text{min}}$, $\tilde{k}_\chi^{\text{min}}$ and x as well as ϕ . (Note that the new variable \tilde{k} that we have defined here and that we will use throughout the following is *not* given by k/T , where k is the integration variable in Eq. (2.3).) We have defined new variables in the way that we have because the constraints (3.1) and (3.2) can be expressed explicitly in terms of these variables, as we now explain. We have defined x in such a way that satisfying the constraint (3.1), namely $|t| > am_D^2$, can be accomplished by requiring that $x < 1$. In order to satisfy the constraint (3.2), we need $\cos \phi < (C_u - x)/D$. This condition follows from writing $u = t(C_u - D \cos(\phi))$ as in Eq. (3.5), which makes clear that imposing $|u| > am_D^2$ yields $C_u - D \cos(\phi) > am_D^2/|t| = x$. If $|C_u - x| > D$, this is automatically satisfied for all ϕ . If $|C_u - x| \leq D$, then ϕ is restricted by $\cos \phi < (C_u - x)/D$. Furthermore, x , \bar{t} and $\tilde{k}_\chi^{\text{min}}$ must be nonzero, with the additional constraint that $k_\chi^{\text{min}} < p_{\text{in}}$, as we now explain. Since we work only in the hard-scattering regime where $|t| > am_D^2 > 0$, it is apparent that $x = am_D^2/|t|$ and $\bar{t} = t/(am_D^2)$ must be nonzero and from Eq. (3.9) we see that $\tilde{k}_\chi^{\text{min}}$ is also nonzero. Turning now to showing that $k_\chi^{\text{min}} < p_{\text{in}}$, from Eq. (3.9) we see that this is equivalent to showing that $|t| < 2p_{\text{in}}(q - \omega)$. With $\omega = p_{\text{in}} - p$ and $q = \sqrt{p_{\text{in}}^2 + p^2 - 2p_{\text{in}}p \cos \theta}$, since $|t| = 2p_{\text{in}}p(1 - \cos \theta)$ it follows that

$$|t| < 2p_{\text{in}}(q - \omega) \iff p(1 - \cos \theta) < q + p - p_{\text{in}} \iff q > p_{\text{in}} - p \cos \theta. \quad (3.10)$$

Therefore it suffices to show that $q > p_{\text{in}} - p \cos \theta$. From the explicit form of q given in Eq. (2.16), we note that

$$q^2 - (p_{\text{in}} - p \cos \theta)^2 = p^2 \sin^2 \theta \geq 0. \quad (3.11)$$

Since $q \geq 0$, $q^2 \geq (p_{\text{in}} - p \cos \theta)^2 \implies q \geq p_{\text{in}} - p \cos \theta$, with equality only for exactly collinear scattering. Thus, throughout the region of space with $|t| > 0$, $k_\chi^{\text{min}} < p_{\text{in}}$.

Recall that our first task is (for each parton in a parton shower, for each time step Δt) to determine whether or not an elastic scattering with high momentum transfer as we have defined it has occurred, and that this requires integrating our probability distribution $F^{C \rightarrow A}$ over the allowed regions of ϕ , k_T , θ and p . We shall, instead, formulate this integral in terms of the new variables ϕ , \tilde{k} , $\tilde{k}_\chi^{\text{min}}$ and x . Writing the constraint $|t| > am_D^2$ in terms of the new variables is trivial since $|t| > am_D^2 \implies x < 1$. To make explicit that the constraint $|u| > am_D^2$ can indeed be written in terms of the new variables $(\phi, \tilde{k}, \tilde{k}_\chi^{\text{min}}, x)$, we begin by observing that since $u = t(C_u - D \cos \phi)$ [cf. Eq. (3.5)],

$$|u| > am_D^2 \iff C_u - D \cos \phi > \frac{am_D^2}{|t|} \equiv x \iff C_u - x - D \cos \phi > 0. \quad (3.12)$$

We now need to show that C_u and D , which were defined in Eqs. (3.7) and (3.8) in terms of the variables ω , q , p , t , k_T and k_χ (as well as the fixed parameter p_{in}) can be written in terms of the variables $(\tilde{k}, \tilde{k}_\chi^{\text{min}}, x)$. We do so as follows. First, we note that $t = -am_D^2/x$ and observe that $\omega^2 - q^2 = t$ and Eq. (3.9) in the form $q - \omega = |t|/(2k_\chi^{\text{min}})$ together imply that

$$\omega = k_\chi^{\text{min}} - \frac{|t|}{4k_\chi^{\text{min}}}, \quad \text{and} \quad q = k_\chi^{\text{min}} + \frac{|t|}{4k_\chi^{\text{min}}}, \quad (3.13)$$

Upon recalling also that $p = p_{\text{in}} - \omega$, we see that we have written ω , q , p and t in terms of x and k_χ^{min} . Next, the definition $\tilde{k} \equiv \tilde{k}_T - \tilde{k}_T^{\text{min}} = \tilde{k}_T - (\tilde{q} - \tilde{\omega})/2$ allows us to write \tilde{k}_T in terms of \tilde{k} as well as q and ω , which we have already written in terms of x and k_χ^{min} . Last, we observe that

$$\tilde{k} + \tilde{k}_\chi^{\text{min}} = \tilde{k}_T + \tilde{k}_\chi^{\text{min}} - \frac{\tilde{q} - \tilde{\omega}}{2} = \tilde{k}_T + \tilde{k}_\chi^{\text{min}} - \frac{|t|}{4k_\chi^{\text{min}}} = \tilde{k}_T + \tilde{\omega} = \tilde{k}_T + \tilde{p}_{\text{in}} - \tilde{p} = \tilde{k}_\chi, \quad (3.14)$$

where we have used Eqs. (3.9) and (3.13) as well as energy conservation to relate \tilde{k}_χ to \tilde{k} and k_χ^{min} . With these substitutions, C_u and D as defined in Eqs. (3.7) and (3.8) are expressed in terms of the variables $(\tilde{k}, \tilde{k}_\chi^{\text{min}}, x)$ and the fixed parameter \tilde{p}_{in} . This means that, per Eq. (3.12), when we write the constraint $|u| > am_D^2$ as

$$\mathcal{P}_u = \Theta(|u| - am_D^2) = \Theta(C_u - x - D \cos \phi), \quad (3.15)$$

we have cast this constraint entirely in terms of the new variables $(\phi, \tilde{k}, \tilde{k}_\chi^{\text{min}}, x)$. Of course, the constraint $|t| > am_D^2$ can straightforwardly be cast as

$$\mathcal{P}_t = \Theta(|t| - am_D^2) = \Theta(1 - x). \quad (3.16)$$

Writing the two constraints in this fashion enables the phase space integral to be transformed as follows:

$$\int dp \int d\theta \int dk_T \int d\phi \mathcal{P}_t \mathcal{P}_u \rightarrow \int_0^1 dx \int_0^{p_{\text{in}}} d\tilde{k}_\chi^{\text{min}} \int_0^\infty d\tilde{k} \int_0^{2\pi} d\phi \mathcal{P}_u |\mathcal{J}|, \quad (3.17)$$

where $|\mathcal{J}|$ is a Jacobian factor which results from the changes of variables and is given by

$$\frac{1}{16(2\pi)^3} \frac{p \sin \theta}{p_{\text{in}} q T} |\mathcal{J}| = \frac{T^2}{p_{\text{in}}^2 (4\pi)^3} \frac{a m_D^2}{4 k_\chi^{\text{min}} x} \frac{1}{x T} = \frac{1}{\tilde{p}_{\text{in}}^2 (4\pi)^3} \frac{k_T^{\text{min}}}{x T} = \frac{\eta \tilde{k}_T^{\text{min}}}{x} \quad (3.18)$$

with $\eta^{-1} \equiv (4\pi)^3 \tilde{p}_{\text{in}}^2$. By construction, this phase space integral transformation is useful for evaluating the probabilities with which elastic scattering processes occur. We shall see that it is also useful for determining the kinematics of these scatterings. We shall focus on these two goals in the next subsection.

3.2 Evaluating the Probability of Elastic Scatterings and Sampling Kinematic Variables

Having constrained our region of phase space to that which is allowed by the kinematic constraints that include only hard, perturbative, elastic scatterings, we now turn to the practical tasks of evaluating the probabilities of such scatterings and sampling their associated kinematics. We begin by computing the probability that a parton with energy p_{in} undergoes Molière scattering during a time interval Δt by integrating the differential probability density $F^{C \rightarrow A}(p, \theta; p_{\text{in}})$ over the allowed region of phase space. Next, we describe how to choose the momenta of the two partons after the scattering (if a Molière scattering process occurs) in a way that satisfies energy and momentum conservation and the constraints (3.1) and (3.2) by sampling the kinematic variables of the Molière scattering over the allowed phase space according to the appropriate probability distribution. This sampling procedure is required to generate physically consistent final-state momenta for the outgoing partons from a $2 \rightarrow 2$ Molière scattering.

We begin by computing the total probability with which a hard parton of type C will undergo an elastic scattering with a quasiparticle in the medium, which is given by

$$P_{\text{tot}} = \int dp \int d\theta F^{C \rightarrow \text{all}}(p, \theta) = \int dp \int d\theta \left(F^{C \rightarrow G}(p, \theta) + F^{C \rightarrow Q}(p, \theta) + F^{C \rightarrow \bar{Q}}(p, \theta) \right). \quad (3.19)$$

And, per Eqs. (2.10)–(2.15), each $F^{C \rightarrow A}(p, \theta; p_{\text{in}})$ can be written as a linear combination of terms $\langle\langle n \rangle\rangle_{D,B}$ and $\langle\langle \tilde{n} \rangle\rangle_{D,B}$ corresponding to the eleven different possible $2 \rightarrow 2$ scattering processes labeled by n . According to Eq. (2.22), each $\langle\langle n \rangle\rangle_{D,B}$ and $\langle\langle \tilde{n} \rangle\rangle_{D,B}$ may be written as a linear combination of seven terms $\langle m_i(t, u) \rangle$ defined in Eq. (2.23) as

$$\langle m_i(t, u) \rangle = \int_{k_T^{\text{min}}}^{\infty} dk_T \int_0^{2\pi} d\phi m_i^{D,B}(t, u), \quad (3.20)$$

where

$$m_i^{D,B}(t, u) \equiv \frac{[1 \pm n_A(p)]}{16(2\pi)^4} \left(\frac{p \sin \theta}{p_{\text{in}} q T} \right) n_D(k_T) [1 \pm n_B(k_\chi)] m_i(t, u). \quad (3.21)$$

Here, i runs from 1 to 7, and the coefficients that specify the 22 linear combinations of the m_i 's that make up the $\langle\langle n \rangle\rangle_{D,B}$ and $\langle\langle \tilde{n} \rangle\rangle_{D,B}$ are given in Appendix A. With all this in mind, we define

$$P_i \equiv \int dp \int d\theta \int dk_T \int d\phi m_i^{D,B}(t, u) \mathcal{P}_t \mathcal{P}_u \quad (3.22)$$

$$= \int_0^1 dx \int_0^{p_{\text{in}}} d\tilde{k}_\chi^{\text{min}} \int_0^\infty d\tilde{k} \int_0^{2\pi} d\phi |\mathcal{J}| m_i^{D,B}(t, u) \mathcal{P}_u, \quad (3.23)$$

where in the second equality we have used the change of variables in Eq. (3.17) and where i runs from 1 to 7. Defining $P^{(n)} \equiv \sum_{i=1}^7 c_i^{(n)} P_i$ and $\tilde{P}^{(\tilde{n})} \equiv \sum_{i=1}^7 \tilde{c}_i^{(\tilde{n})} P_i$ (where the coefficients $c_i^{(n)}$ and $\tilde{c}_i^{(\tilde{n})}$ are the same coefficients as in Eq. (2.20)), the total probability P_{tot} in Eq. (3.19) for the occurrence of an elastic scattering between an incoming parton c of type C with incoming momentum p_{in} and a quasiparticle in the medium is then given by a linear combination of $P^{(n)}$ and $\tilde{P}^{(\tilde{n})}$, analogous to Eqs. (2.10)+(2.11)+(2.12) for an incident quark or antiquark and analogous to Eqs. (2.13)+(2.14)+(2.15) for an incident gluon. We defer a description of how we compute the integrals in Eq. (3.23) to Appendix D.

Note that each $F^{C \rightarrow A}$ term in the total probability (3.19) is proportional to the chosen timestep Δt (c.f. Eq. (2.3)). So, Eq. (3.19) is accurate only when Δt is small enough that the probability of more than one hard scattering occurring in the interval Δt is negligible. We interpret P_{tot} as the first-order expansion of a Poisson process with total rate $P_{\text{tot}}/\Delta t$. Then, the probability that at least one elastic scattering with high momentum transfer occurs in the time interval Δt is then

$$P_{\text{step}} = 1 - e^{-P_{\text{tot}}}. \quad (3.24)$$

Evaluating P_{step} is our first goal. In Appendix D, we describe how we evaluate the four integrals in Eq. (3.23), doing two of them analytically and two of them numerically. Note that if P_{tot} is sufficiently small, then $P_{\text{step}} \approx P_{\text{tot}}$. Furthermore, note that the probability of n Molière scatterings occurring within the time interval Δt is $(P_{\text{tot}})^n e^{-P_{\text{tot}}}$, which is suppressed by powers of $P_{\text{tot}} \ll 1$. Although in answering the question of whether an elastic scattering with high momentum transfer has occurred we shall evaluate P_{step} , we shall always make sure that Δt is small enough that $P_{\text{tot}} \ll 1$ and $P_{\text{step}} \approx P_{\text{tot}}$ so that we can assume that only one elastic scattering with high momentum transfer occurs during the time interval Δt with probability P_{step} .

Before continuing onward to describing how we sample the kinematic variables of the Molière scattering process so as to choose the momenta of the two partons after a scattering from the appropriate probability distribution, it will be helpful to visualize that probability distribution. Visualizing the full four-dimensional distribution, either over the variables (p, θ, k_T, ϕ) or over the variables $(x, \tilde{k}_\chi^{\text{min}}, \tilde{k}, \phi)$, would be a challenge and is not necessary. It will suffice to visualize the probability distribution over the variables (p, θ) , which we do by plotting $F^{G \rightarrow \text{all}}(p, \theta; p_{\text{in}})$ in Fig. 2. Recall that this is the probability density for finding an outgoing particle of any type with an energy p at an angle θ with respect to the direction of an incoming gluon with energy p_{in} . In plotting Fig. 2, we have evaluated $F^{G \rightarrow \text{all}}(p, \theta; p_{\text{in}})$ at a grid of values of (θ, p) where the constraint (3.1) is satisfied. At each point in the grid, we evaluate $k_T^{\text{min}} = (q - p_{\text{in}} + p)/2$ with q defined in Eq. (2.16) and then perform the phase space integrations over k_T from k_T^{min} to infinity and over ϕ that are needed to evaluate the seven functions $\langle m_i(t, u) \rangle$ defined in Eq. (2.23) numerically, with the Heaviside Θ function that defines the constraint (3.2) included in the integrand. We then take the appropriate linear combinations of these functions for each possible $2 \rightarrow 2$

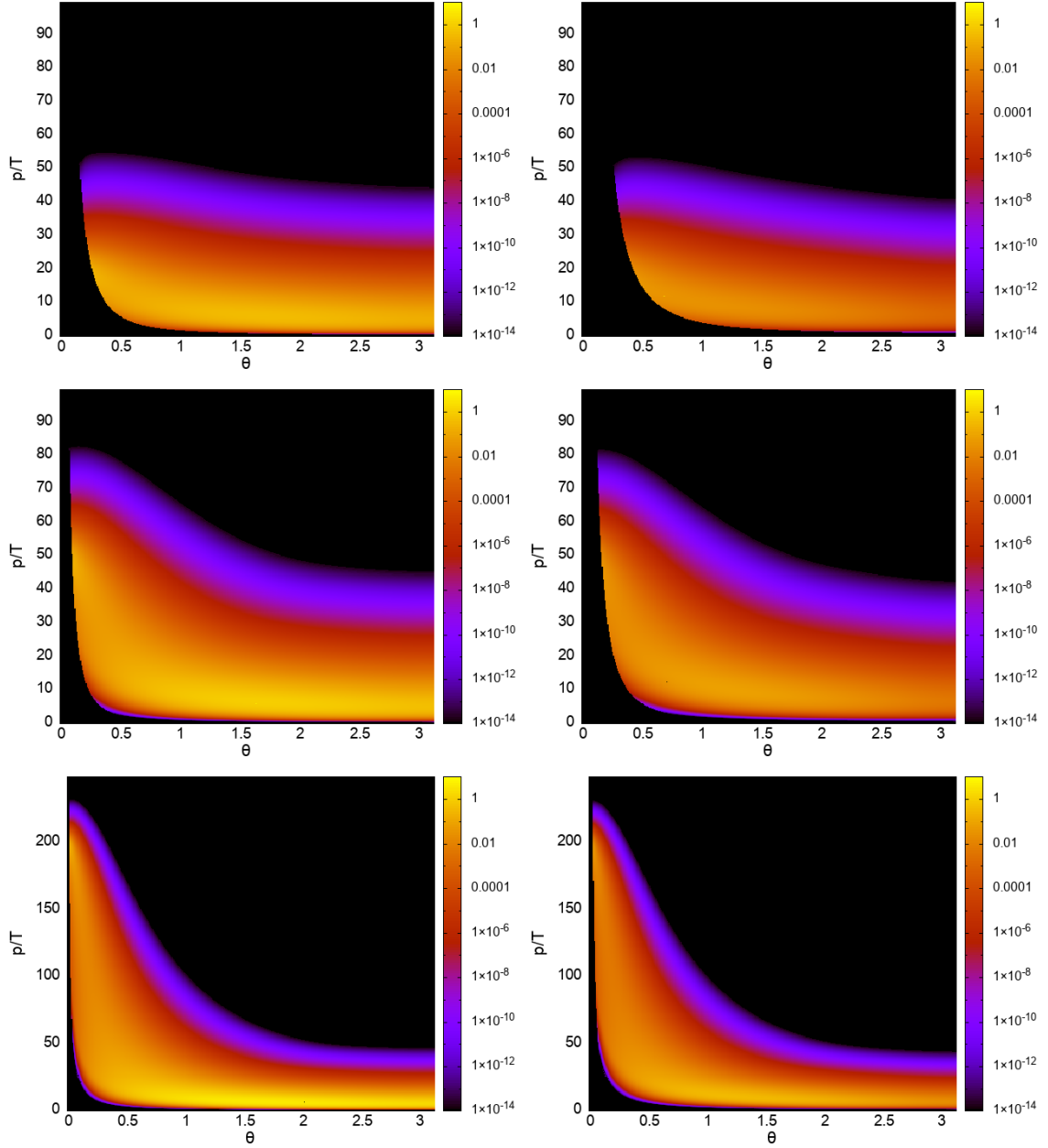


Figure 2: Probability distributions $F^{G \rightarrow \text{all}}(p, \theta; p_{\text{in}})$ for finding a scattered parton with energy and angle (p, θ) from the Molière scattering of an incoming gluon with $p_{\text{in}} = 20T$ (top panels), $50T$ (middle panels), and $200T$ (bottom panels) that has traveled for a time $\Delta t = 6/T$ through a “brick” of QGP with a constant temperature T . We have chosen the two parameters that specify the elastic scattering probabilities (see text for their definition and description) to be $g_s = 2.25$ and $a = 4$ in the left panels, and $g_s = 2.25$ and $a = 10$ in the right panels.

scattering process, see Eq. (2.22), and then, along the lines of Eqs. (2.10)–(2.15), we sum over all the $2 \rightarrow 2$ processes that contribute to $F^{G \rightarrow \text{all}}(p, \theta; p_{\text{in}})$.

In Fig. 2, we show probability distribution $F^{G \rightarrow \text{all}}(p, \theta; p_{\text{in}})$ for the Molière scattering of a relativistic gluon with $p_{\text{in}} = 20T$ (top panels), $50T$ (middle panels), and $200T$ (bottom panels) traveling for a time interval $\Delta t = 6/T$ through a “brick” of QGP with a constant temperature T and a thickness of at least $6/T$. In the Hybrid Model calculations that will be our focus throughout most of this paper, Δt will be a small timestep, but for visualizing the probability distribution and so as to make comparisons to the results of Ref. [39] possible, it is helpful here to consider a brick of QGP. In all panels of Fig. 2 we have chosen the value $g_s = 2.25$ (corresponding to $\alpha_s = 0.4$) for the QCD coupling constant that sets the magnitude of the elastic scattering matrix elements and the Debye mass m_D ; we have displayed results obtained with two different choices of the parameter a (recall that we include only those elastic scattering processes with momentum transfer $> am_D^2$), with $a = 4$ in the left panels of the Fig. 2 and $a = 10$ in the right panels. (Throughout most of this paper, we shall choose $a = 10$.) Fig. 2 illustrates how the phase-space constraints derived in Section 3.1 restrict the allowed values of momentum p and scattering angle θ for the outgoing hard partons after the scattering. The black region at small p or/and θ is excluded by requiring $|t| > am_D^2$, which is a constraint on p and θ , see Eq. (3.1). Enforcing the constraint $|u| > am_D^2$ is responsible for reducing the probability for obtaining scattered particles with small p or/and θ in the region of (p, θ) just outside the black excluded region. If we had only enforced the constraint on t , this region would have been yellow; in fact, it is red/purple. By comparing the right panels to the left panels, we see that increasing a expands the regime of low-momentum transfer elastic scattering that we are excluding, which is as expected. Increasing a has little effect on the probability for the larger momentum transfer elastic scattering processes that we shall include in the Hybrid Model.

By comparing the upper, middle and lower panels of Fig. 2 at around, say, $\theta = 0.5$ radians, we see that increasing the energy of the incident parton shifts the probability distribution for the scattered parton energy to larger p and squeezes the probability distribution for the scattering angle θ to smaller angles, for high energy scattered partons. These scattered partons with larger values of p are most likely the scattered incident partons, but note that these are not all that is plotted in Fig. 2. We are plotting the probability distribution for finding a scattered parton with (p, θ) , but this scattered parton may well be a parton from the QGP that was kicked by the incident gluon. Indeed, the yellowest regions in the probability distributions plotted in Fig. 2 that correspond to scattered partons with energies $\sim 10T$ found at all angles including very large angles are most likely partons from the QGP. This intuition, visualized in Fig. 2 will be important in understanding results from our Hybrid Model calculations that we shall present later.

Having visualized the probability distribution for the energy and angle of partons resulting from Molière scattering processes, we now turn to the calculations that we need in order to be able to implement Molière scattering in the Hybrid Model. Earlier in this Section, we have set up the computation of P_{step} , defined in Eq. (3.24), namely the probability that a Molière scattering occurs during a small timestep Δt . We now describe how we choose the identities, and momenta, of the two partons that result from such an elastic $2 \rightarrow 2$ scattering process. Although in Fig. 2 we only asked about the probability for

finding a single scattered parton thus and so, in the Hybrid Model we will need to specify both scattered partons, with their identities and momenta sampled from the appropriate probability distribution.

During each timestep, we choose a random number between 0 and 1 that, first, determines whether or not the incoming parton of type C undergoes a Molière scattering $cd \rightarrow ab$, noting that the probability that an elastic scattering has occurred is P_{step} . If the Molière scattering has occurred, we calculate the three individual probabilities for the cases where $A = Q$ or $A = \bar{Q}$ or $A = G$. Based upon the value of another random number, we then decide whether $A = Q$ or \bar{Q} or G . We can then determine which of the eleven processes in Table 1 occurred by calculating the conditional probability with which each process may occur, given that the incoming parton is c , and the outgoing parton is of type A as determined in the previous step. The flavor of each (anti-)quark involved in the $2 \rightarrow 2$ scattering is then chosen uniformly from $(\bar{u}, \bar{d}, \bar{s})$ u, d, s .

Once we have decided (probabalistically, as above) which of the eleven $2 \rightarrow 2$ scattering processes occurred, we know the identities of the two scattered partons. To specify their momenta, we need to choose the values of the kinematic variables $(x, \tilde{k}_\chi^{\min}, \tilde{k}, \phi)$ for the Molière scattering process from the appropriate probability distribution. We do so as follows. First, we define conditional probability distribution for the variable x :

$$P_i(x|cd \rightarrow ab) \propto \int_0^{p_{\text{in}}} d\tilde{k}_\chi^{\min} \int_0^\infty d\tilde{k} \int_0^{2\pi} d\phi m_i^{D,B}(t, u) |\mathcal{J}| \mathcal{P}_u. \quad (3.25)$$

We need to choose x by sampling this distribution. We accomplish this via first computing the cumulative distribution functions $\Phi_i(x) = \int_0^x dx' P_i(x')$ corresponding to each of the seven probability distribution functions $P_i(x)$ and adding them in the same way that we described in the paragraph following Eq. (3.23) so as to obtain the total cumulative distribution function $\Phi(x)$. Then, we choose a random number u with a uniform distribution between 0 and 1. Finally, we solve for $x = \Phi^{-1}(u)$ using the bisection method. In this way, we have picked a value of x by sampling the conditional probability distribution (3.25). Having chosen x , we move on to choosing \tilde{k}_χ^{\min} according to the sum of the seven conditional probability distributions

$$P_i(\tilde{k}_\chi^{\min}|x) \propto \int_0^\infty d\tilde{k} \int_0^{2\pi} d\phi m_i^{D,B}(t, u) |\mathcal{J}| \mathcal{P}_u, \quad (3.26)$$

which again we accomplish via first defining a cumulative distribution function, then picking a random number between 0 and 1, and choosing \tilde{k}_χ^{\min} to be the value at which the cumulative distribution function matches that random number. Having found \tilde{k}_χ^{\min} and x , we then sample \tilde{k} using the cumulative distribution functions of

$$P_i(\tilde{k}|\tilde{k}_\chi^{\min}, x) \propto \int_0^{2\pi} d\phi m_i^{D,B}(t, u) |\mathcal{J}| \mathcal{P}_u. \quad (3.27)$$

Finally, having found \tilde{k} , \tilde{k}_χ^{\min} , and x , we sample ϕ using the cumulative distribution functions of

$$P_i(\phi|\tilde{k}, \tilde{k}_\chi^{\min}, x) \propto m_i^{D,B}(t, u) |\mathcal{J}| \mathcal{P}_u. \quad (3.28)$$

All that remains is for us to describe how we compute the conditional probabilities on the right-hand sides of Eqs. (3.28), (3.27), (3.26) and (3.25). Eqs. (3.28) and (3.27) are explicitly calculated in Appendices D.1 and D.2, respectively. The conditional probability distributions in Eqs. (3.26) and (3.25) are evaluated using numerical integration, as described in Appendix D.3. These integrals are complicated by the constraint \mathcal{P}_u , which takes different forms in different regimes of k . These complications are made precise and handled in Appendix D.

The sampling procedure described above yields values for the set of kinematic variables $(x, \tilde{k}_\chi^{\min}, \tilde{k}, \phi)$ that fully specify the kinematics of a Molière scattering process. Around Eqs. (3.13) and (3.14), we have described how to obtain the variables ω, q, p, t, k_T and k_χ from $(x, \tilde{k}_\chi^{\min}, \tilde{k}, \phi)$ and θ can then be obtained via $|t| = 2p_{\text{in}}p(1 - \cos \theta)$. Consequently, as we make explicit in Appendix C, the variables $(x, \tilde{k}_\chi^{\min}, \tilde{k}, \phi)$ specify the energies and angles of the two scattered partons that result from the elastic $2 \rightarrow 2$ scattering process — which is what we will need in the Hybrid Model. The Hybrid Model calculation of a parton shower developing within a droplet of QGP specifies the energy and direction of an incident jet parton and the temperature of the QGP it finds itself in during each time interval Δt ; if a Molière scattering event occurs during a time interval, the kinematic variables (p, θ, k_T, ϕ) that we obtain as we have described specify the energy and direction of the QGP parton that this jet parton scattered from, as well as the energies and directions of the two partons after the elastic scattering. From that time onward, these two partons are treated as a part of the jet shower and evolved accordingly by the Hybrid Model. They will lose energy and momentum to, and create wakes in, the droplet of QGP. And, although this is unlikely, they may scatter elastically again.

4 Incorporating Molière Scatterings in the Hybrid Model

The hybrid strong/weak coupling model, or more simply the Hybrid Model, is a theoretical framework designed to describe the multi-scale processes of jet production and evolution through a droplet of strongly coupled QGP whose expansion and cooling is described via hydrodynamics. The weakly coupled processes of jet production in an initial hard scattering and the subsequent fragmentation into, and evolution of, parton showers are described perturbatively and are implemented in the model using PYTHIA 8 [43] with the EPS09 nuclear parton distribution functions (nPDFs) [44]. Before this study, the Hybrid Model incorporated interactions between jet partons and the strongly coupled QGP in a way that would be appropriate if these interactions are strongly coupled. This is motivated by the fact that the most common momentum transfers q are dominated by the characteristic scales of the medium — such as the temperature T or the Debye mass m_D — at which the strong coupling constant is not small. However, although they are rarer, processes with larger momentum transfer between a jet parton and the QGP can of course occur, and these should be described perturbatively. Elastic Molière scattering is the simplest such process — it must occur although it will not be the only perturbative process via which large momentum transfer occurs. For large-enough momentum-transfers, one can calculate the probability of Molière scatterings perturbatively, as we have done in Sections 2 and

3. By implementing the Molière scattering processes described in Table 1, we incorporate weakly coupled jet-medium processes with large momentum transfer in the Hybrid Model model for the first time. The purpose of our study is to identify jet quenching observables that are sensitive to the presence of Molière scatterings off quasiparticles in the medium. By doing so, we can learn how best to identify and isolate signatures of weakly coupled large momentum transfer processes involving a jet parton and a quasiparticle from the QGP in experimental data. We look forward to the day when this has been done — as at that point if there are quantitative discrepancies between experimental measurements of suitably sensitive observables to the predictions we make this would motivate including other weakly coupled large momentum transfer processes in addition to Molière scattering, which is the simplest example of such a process and which must be present.

In this Section, after reviewing aspects of the Hybrid Model in detail, we review how we incorporate softer Gaussian-distributed transverse momentum broadening, as appropriate in a strongly coupled plasma [27] and then describe in detail how we incorporate hard Molière scatterings in the Hybrid Model.

4.1 Hybrid Model description of strongly coupled jet-medium interactions

An energetic parton produced in a hard QCD process initiated by two partons from the incident nuclei in a heavy ion collision starts out with a virtuality Q of the order of its large transverse momentum p_T . Via a series of splittings that are well described via perturbative QCD, specifically via the DGLAP evolution equations, the hard parton branches into a parton shower. In vacuum, perturbative splitting proceeds until the partons in the shower have virtualities of order Λ_{QCD} at which point they hadronize. The processes of jet production in a hard process, parton shower evolution as described by the DGLAP evolution equations, and hadronization are implemented in the Hybrid Model using PYTHIA 8 [43] with nPDFs from EPS09 [44].

When a parton shower develops within the QGP formed in a heavy ion collision, the early high-virtuality splittings in the shower are not significantly modified relative to how they would occur in vacuum because of the large separation between the scale Q and the temperature of the medium T . As these vacuum-like splittings take place, however, interactions between the partons in the developing shower and the QGP are nevertheless occurring. These interactions are dominated by very common, soft, momentum exchanges that are strongly coupled — that have been the focus of the Hybrid Model prior to this study as we review in this subsection — as well as occasional larger-than-average momentum exchanges that can be described at weak coupling that will be our focus in this paper.

In the Hybrid Model, we model the common, strongly coupled, soft exchanges between an energetic parton and the expanding, cooling, droplet of QGP through which it propagates that result in the loss of energy and momentum in the direction of the parton's direction of propagation based upon what we know from holographic calculations that can be performed in the limit of strong coupling. We assume that an energetic quark traversing the droplet of QGP loses energy at a rate which takes the same form as that for a light quark or gluon traversing strongly coupled plasma in $\mathcal{N} = 4$ SYM theory in the limit of infinite coupling and large N_c . A massless parton that began with energy E_{in} and has

traveled a distance x through the strongly coupled plasma loses energy to the plasma at a rate [36, 37]

$$\left. \frac{dE}{dx} \right|_{\text{strongly coupled}} = -\frac{4}{\pi} E_{\text{in}} \frac{x^2}{x_{\text{stop}}^2} \frac{1}{\sqrt{x_{\text{stop}}^2 - x^2}} \quad , \quad (4.1)$$

where $x_{\text{stop}} \equiv E_{\text{in}}^{1/3}/(2T^{4/3}\kappa_{\text{sc}})$ is the maximum distance the parton can travel before completely thermalizing. Here, κ_{sc} is a dimensionless parameter which governs the strength of the interaction between the massless parton and the strongly coupled medium. κ_{sc} is calculable in $\mathcal{N} = 4$ SYM theory and is proportional to $\lambda^{1/6}$, where $\lambda = g^2 N_c$ is the 't Hooft coupling, with a prefactor that depends on details of the theory. Additionally, note that the stopping distance of a gluon is reduced (meaning that κ_{sc} is increased) by a factor $(C_A/C_F)^{1/3}$ compared to that of a quark [45], where C_A and C_F are the Casimirs of the adjoint and fundamental representations of the color gauge group, respectively. In the Hybrid Model, we aim to describe the soft strongly coupled interaction between jet partons and strongly coupled QGP in QCD, not in $\mathcal{N} = 4$ SYM theory. We assume that the rate of energy loss of a quark or anti-quark in the parton shower is governed by Eq. (4.1) with κ_{sc} treated as a parameter to be determined by fitting to experimental data on the suppression of high- p_T charged-hadrons and jets in PbPb collisions at the LHC, and assume that gluons in the parton shower lose energy as described by Eq. (4.1) with

$$\kappa_{\text{gluon}} = (9/4)^{1/3} \kappa_{\text{sc}} \quad . \quad (4.2)$$

Fitting Hybrid Model calculations to data [29] shows that κ_{sc} is smaller (and the stopping distance of massless partons is larger) by a factor of 3 to 4 in QCD than in $\mathcal{N} = 4$ SYM theory.

As the rate of energy loss dE/dx of a parton in the jet depends on the local temperature of the medium at the position and time where the jet parton is found, in any treatment of jet quenching in heavy ion collisions one must assign a spacetime picture to the development of the momentum-space DGLAP shower. In the Hybrid Model, we use a formation time argument, where each parton in the shower propagates for a time $\tau_f \equiv 2E/Q^2$ before splitting. During this time, the propagating parton loses energy as specified by Eq. (4.1) as long as the local temperature is above a temperature which in this work we set to $T_c = 145$ MeV.

The energy and momentum that the jet partons lose, as described by Eq. (4.1), is deposited into the droplet of QGP. The resulting perturbations of the stress-energy tensor of the liquid QGP (which must have a net energy and momentum equal to that lost by the jet) are referred to as jet wakes. In a hydrodynamic fluid, jet wakes are composed of sound modes (compression and rarefaction) and diffusive modes that describe a region of moving fluid behind the jet where the fluid has picked up net momentum in the direction of the jet. This wake evolves hydrodynamically as the medium expands, flows, and cools until it reaches the freezeout hypersurface and a complete description of this evolution, including the interplay between the jet-induced wake and the background flow of the expanding droplet, requires 3+1-dimensional relativistic hydrodynamic simulations.

In the present paper, we adopt a much simpler description of the observable consequences of jet wakes, based upon a set of simplifying assumptions first employed in Ref. [27]. First, we neglect transverse flow, and assume that the longitudinal expansion of the background fluid is boost invariant, i.e. is a Bjorken flow. Second, we assume that the perturbation stays close in rapidity to the rapidity at which it was deposited. Third, we assume that the jet-induced perturbations to the hydrodynamic stress-energy tensor are small. And, fourth, we assume that after freezeout according to the standard Cooper-Frye prescription at the freezeout hypersurface [46], the perturbations to the spectra of the resulting hadrons is small at all transverse momenta p_T . This fourth assumption, which is only valid in the very soft particle limit, allows us to integrate the flow and entropy profiles over the whole freezeout hypersurface and express the perturbations to the hadronic spectra after freezeout in terms of the deposited momentum and energy. This (over)simplification allows us to ignore the details of the evolution of the perturbed fields and specify the distribution of soft particles originating from the wake of a jet entirely from energy-momentum conservation. The one-body distribution then reads [27]

$$E \frac{d\Delta N}{d^3p} = \frac{1}{32\pi} \frac{m_T}{T^5} \cosh(y - y_j) \exp \left[-\frac{m_T}{T} \cosh(y - y_j) \right] \times \left\{ p_\perp \Delta P_\perp \cos(\phi - \phi_j) + \frac{1}{3} m_T \Delta M_T \cosh(y - y_j) \right\}, \quad (4.3)$$

where m_T , p_\perp , ϕ and y are the transverse mass, transverse momentum, azimuthal angle and rapidity of the hadrons originating from a jet wake and ΔM_T and ΔP_\perp are the transverse mass and transverse momentum that a jet parton with azimuthal angle ϕ_j and rapidity y_j lost per Eq. (4.1) and deposited in the hydrodynamic fluid. The distribution (4.3) is oversimplified but it has the advantage of being fully specified analytically, with no new free parameters. And, it captures important key features, including an enhancement of soft particle production around the jet direction and a depletion of soft particles in the direction opposite to the jet direction in azimuthal angle ϕ . Both are direct consequences of the diffusive modes in the wake: the jet “boosts” a region of fluid in the direction of the jet, resulting in more soft particles in that direction and fewer soft particles in the opposite direction after freezeout than would have been the case if that region of fluid had not been moving. The depletion of soft particle production in the direction opposite to the jet has recently been observed in Z -jet events by CMS [47], with a magnitude that is well described by Eq. (4.3). Eq. (4.3) does not, however, account for the interplay between the hydrodynamic evolution of the wake and the transverse flow of the background fluid, among other effects, meaning that the particles generated with Eq. (4.3) are too soft and too wide in azimuthal angle [27]. An efficient description of a more complete treatment of the response of the flowing hydrodynamic fluid to the passage of a jet, based on the linearized hydrodynamics solutions of Ref. [38], is work in progress by these authors.

While Eq. (4.1) describes energy loss, it has long been known that an energetic parton travelling through strongly coupled plasma will in addition accumulate momentum k_T transverse to its direction of propagation via continuous soft momentum exchange, referred

to as transverse momentum broadening. In a weakly coupled plasma, transverse momentum broadening occurs via repeated soft scattering. In a strongly coupled liquid, it occurs continuously in time with a Gaussian distribution for k_T whose width $\langle k_\perp^2 \rangle$ grows linearly with the time δt for which the parton propagates: $\langle k_\perp^2 \rangle = \hat{q} \delta t$, where \hat{q} is a property of the strongly coupled medium referred to as the jet quenching parameter [18–21]. In the strongly coupled plasma of $\mathcal{N} = 4$ SYM theory in the limit of large coupling and large N_c , the jet quenching parameter is given by [18–21]

$$\hat{q}_{\text{AdS/CFT}} \approx 7.53 \sqrt{\lambda} T^3 \equiv KT^3, \quad (4.4)$$

where λ is the 't Hooft coupling. Note that \hat{q} in Eq. (4.4) is not proportional to N_c^2 , which would be the case in a weakly coupled plasma where \hat{q} would be proportional to the number density of quasiparticles off which a jet parton could scatter. This highlights the fact that soft Gaussian transverse momentum broadening occurs in a strongly coupled plasma that, as in $\mathcal{N} = 4$ SYM theory, is strongly coupled at all scales and has no quasiparticles.

Transverse momentum broadening with $\hat{q} = KT^3$ was first implemented in the Hybrid Model in Ref. [27]. As there, since we are interested in transverse momentum broadening in strongly coupled QGP in QCD not in $\mathcal{N} = 4$ SYM theory, we shall take K as a parameter that should ultimately be fitted to experimental data. The analysis of Ref. [27] found that the experimental observables available at that time showed little sensitivity to transverse momentum broadening even for K as large as ~ 40 , whereas Eq. (4.4) suggests $K \sim 29$ in $\mathcal{N} = 4$ SYM theory with $\lambda = 4\pi$, meaning $\alpha = 0.4$, and in the strongly coupled QGP of QCD, K will be smaller. If we knew that K in QCD was smaller than K in $\mathcal{N} = 4$ SYM theory by the same factor as for κ_{sc} , we could use what has been learned by fitting κ_{sc} to data to estimate $K \sim 7 - 10$, but there is no available holographic computation that relates the energy loss and transverse momentum broadening of massless partons, meaning that ultimately the value of K used in the Hybrid Model should be determined via fitting to experimental data. We shall describe how we choose K in this paper in the next subsection.

4.2 Adding perturbative hard processes within strongly coupled plasma

The $2 \rightarrow 2$ elastic scattering processes with large momentum transfer, namely the Molière scattering processes that are our object of study in this paper, impart transverse momentum to jet partons that is *not* Gaussian distributed, with a harder distribution at high momentum transfer. (This goes back to Rutherford scattering, with momentum transfer distributed $\sim k_T^{-4}$. In the present context, the power-law tail of the distribution can even be somewhat harder than this [48, 49].) Although the soft low momentum exchange processes that lead to Gaussian transverse momentum broadening as specified by Eq. (4.4) are more common than Molière scattering (and in fact happen continuously at strong coupling), rare weakly coupled high momentum transfer processes where a jet parton resolves and scatters off a quasiparticle in the QGP are important because, uniquely, they give us access to the microscopic, short lengthscale, properties of QGP.

The new element that we add to the Hybrid Model in this paper is that at every time-step during the in-medium evolution, for each jet parton in the parton shower, we allow for

the possibility that this parton scatters elastically off a weakly coupled quasiparticle from the QGP with a momentum transfer that is greater than a minimum threshold that we specify. We describe such Molière scattering processes to leading order in weak coupling as in Section 2 and, as described in Section 3, only include processes in which the Mandelstam variables t and u both exceed a threshold expressed as $|t|, |u| > am_D^2$. Here, $m_D^2 = g_s^2 T^2 (N_c + N_f/2)/3$ and we shall take $g_s = 2.25$, corresponding to $\alpha_s \simeq 0.4$, throughout and shall of course take $N_c = N_f = 3$. We are free to choose the threshold parameter a . In this subsection we shall consider $a = 4$ and $a = 10$. Elsewhere in this paper, we shall take $a = 10$ which is more conservative: choosing a larger threshold a reduces the effects of Molière scattering in experimental observables, improves the validity of our assumption that these elastic scattering processes are weakly coupled and can be treated perturbatively, and reduces the risk that we are double counting by extending the Molière scattering calculation down into the low momentum transfer regime that we have already included via strongly coupled transverse momentum broadening as specified by the parameter K .

The considerations above suggest that, given a value of a , we should adjust the value of K to ensure a smooth matching between the probability distribution for k_T coming from rare hard Molière scatterings and that coming from the strongly coupled soft Gaussian transverse momentum broadening specified by Eq. (4.4). This happens naturally in a weakly coupled treatment in which the soft Gaussian-distributed transverse broadening arises from multiple soft scattering treated in the same calculation as the rare hard Molière scattering, for example as in Refs. [50, 51]. As we are treating the soft Gaussian transverse momentum broadening as strongly coupled, we will ultimately need to fit the value of K to data and for the present need to adjust its value by hand. We illustrate how we do this in Fig. 3, which shows (for different choices of a and K) the probability with which an energetic light quark picks up momentum k_T transverse to its direction of propagation after traversing a distance $L = 2$ fm through a static brick of QGP with temperature $T = 0.3$ GeV. (We have chosen $L = 2$ fm because in the Hybrid Model the mean distance that a parton in the shower propagates between the splitting at which it originates and the point where it splits in two is ~ 2 fm.) The calculation of the Molière scattering contribution to this probability distribution proceeds as described around Fig. 2. For $K \neq 0$, the energetic parton picks up an additional Gaussian-distributed transverse momentum with $\langle k_T^2 \rangle = KT^3L$. The energetic particle is a quark with energy $E = 20$ GeV in the left panels, while in the right panels we choose $E = 80$ GeV. The value of the threshold parameter is $a = 4$ in the upper panels and $a = 10$ in the lower panels. All panels show results with only Molière scattering ($K = 0$; black bands) and with soft Gaussian transverse momentum broadening with $K = 4, 7$ and 15 , with and without Molière scattering.

The first thing that one clearly appreciates from Fig. 3 is that the large k_T region is indeed dominated by the Molière scattering, as expected. Comparing the left and right panels also makes it evident that while the contribution coming from strongly coupled Gaussian transverse momentum broadening does not depend on the energy E of the jet parton, the contribution from Molière scattering does. This is also as expected, since there is more phase space where elastic scattering off a thermally distributed medium quasiparticle imparts a momentum k_T to the jet parton when the incident jet parton has

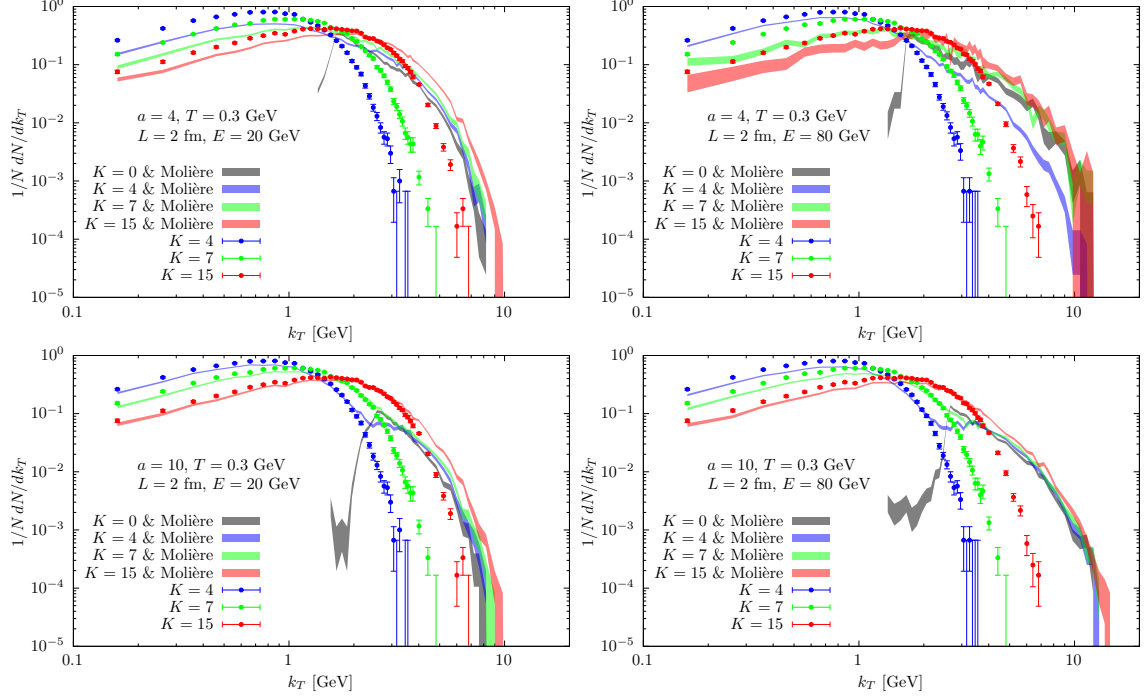


Figure 3: Probability for an incoming quark with energy $E = 20$ GeV (left panels) or $E = 80$ GeV (right panels) to obtain a transverse momentum k_T after traversing a brick of QGP with length $L = 2$ fm and temperature $T = 0.3$ GeV. Different colors correspond to different choices of the parameter K that governs the magnitude of the soft Gaussian transverse momentum broadening. The bands include Molière scattering with squared momentum transfer greater than am_D^2 , where we have chosen the threshold parameter as $a = 4$ (upper panels) or $a = 10$ (lower panels). The points with a given color show the results with that value of K in the absence of Molière scattering. All probability distributions are normalized. (In the case of the grey bands, where $K = 0$, the most probable outcome is $k_T = 0$, no Molière scattering; this is not depicted.)

a higher E . One can appreciate this by noting that when $E = 20$ GeV the k_T distribution drops off steeply as k_T approaches 10 GeV, roughly half E , whereas when $E = 80$ GeV the harder power-law distribution in k_T is apparent for $k_T \sim 10$ GeV and beyond.

We can now describe how we use the results plotted in Fig. 3 to motivate our choice of K , for a given choice of a . Let us begin with $a = 10$. (With $g = 2.25$ and $T = 0.3$ GeV, this corresponds to requiring $|t|, |u| > (2.6 \text{ GeV})^2$.) We see in both bottom panels that if we were then to choose $K = 4$, we obtain a rather unphysical looking probability distribution with a dip in it. From the bottom left panel, we see that with $a = 10$ if we choose either $K = 7$ or $K = 15$, we obtain a smooth probability distribution for k_T for jet partons with $E = 20$ GeV. From the bottom right panel, though, we see that this is better achieved with $K = 15$ than with $K = 7$ for jet partons with $E = 80$ GeV. Since we wish to choose $a = 10$ in order to be conservative in the sense described above, we shall take $K = 15$ throughout the rest of this paper. Any value in the range $7 < K < 15$ is not unreasonable, however,

and in future both K and a should be constrained via fitting Hybrid Model calculations of sufficiently many sufficiently differential observables to experimental data. Note that we see from the upper panels of Fig. 3 that if we were to choose the lower, less conservative, value $a = 4$ for the threshold parameter, including elastic scattering processes with lower momentum transfers, we could accommodate a lower value of K .

We close this subsection by stressing that Molière scattering is only the simplest example of a weakly coupled process where a jet parton scatters off a quasiparticle from the QGP at high momentum transfer; such processes can also be inelastic. Strongly coupled soft inelastic processes are of course already incorporated in the Hybrid Model, but we leave a treatment of weakly coupled inelastic processes with large momentum transfer to future work. At a qualitative level, though, it seems reasonable to speculate that including such processes while somewhat increasing the threshold a that defines which elastic scatterings we include could yield comparable results, both for the probability distribution for k_T in Fig. 3 and for the experimental observables that we shall investigate using the Hybrid Model.

4.3 Monte Carlo implementation within the Hybrid Model

In the previous subsection, we have used a toy calculation involving a brick of QGP to fix our choice of the two parameters that appear in our weakly coupled description of Molière scattering at large momentum transfer, namely $g_s = 2.25$ and $a = 10$, and the one parameter that appears in our description of strongly coupled soft transverse momentum broadening, namely $K = 15$. We turn now to implementing Molière scattering in the Hybrid Model, so that in the next Section we can calculate Hybrid Model predictions for experimental observables with and without including Molière scattering.

At each time step in the Hybrid Model description of an event, we have jet partons propagating through a droplet of QGP whose expansion and cooling is described via a hydrodynamic profile. At each time step in the laboratory frame Δt_{LAB} , a given parton in the shower will be located in a fluid cell with some temperature T and fluid velocity v^i , in the lab frame. The temperature of the QGP is defined in the local fluid rest frame, however. So, before computing the energy loss according to Eq. (4.1), Gaussian transverse momentum broadening with $\langle k_T^2 \rangle \propto KT^3$, and (with some probability) Molière scattering we must first boost from the lab frame to the local fluid rest frame. After doing these computations, we then boost back to the lab frame and, in the lab frame, determine where the jet parton (or two jet partons if a Molière scattering has occurred) are located at the next time step and what the fluid velocity and fluid temperature are at that new spacetime point.

We note here as an aside that because we boost to the local fluid rest frame, compute Molière scattering there, and boost back to the lab frame (which is the same as the collision center of mass frame), and because we make no eikonal approximation, our calculation has encoded within it the way that the flowing medium impacts the shape of jets — at least via high-momentum transfer elastic scattering. The manner in which the hydrodynamic flow of a droplet of QGP can give jets in a fluid flowing transverse to the jet direction a shape that is asymmetric around the jet axis has been of long-standing interest [52] and

has been the subject of much recent work [53–61]. Although the observables that we shall investigate in this study do not do so, in future work one could use the same simulations that we have performed to investigate the contribution of Molière scattering to observables that may be sensitive to jet distortion. The Hybrid Model calculations that we perform in this study do not include distortions of jet wakes arising from fluid flow transverse to the jet, but by building upon the work of Ref. [38] this could be added too.

Returning to describing our implementation, we note following Ref. [26] that in order to apply the strongly coupled energy loss rate from Eq. (4.1), one observes that $dE_L(x_L)/dx_L = dE_F(x_F)/dx_F$, where the subscripts refer to the lab frame and the local fluid rest frame. This means that the amount of energy lost in the lab frame can be computed using Eq. (4.1) in the local fluid rest frame, where all we need from the local fluid rest frame is the value of T . The computation of the Gaussian transverse momentum broadening must be performed in the local fluid rest frame, where we impose that the kick received by the parton is transverse to the parton velocity in that frame, that it does not modify its virtuality, and that its energy remains the same in that frame [27]. Both these processes — longitudinal energy loss and Gaussian transverse momentum broadening — modify the kinematics of a given parton at each time step in the in-medium evolution.

The new element in this paper is that at each time step, for each parton in the shower, after boosting to the local fluid rest frame we apply the results that we have obtained in Section 3, using expressions given explicitly in the Appendices, to compute the probability that this parton, whose “incident” momentum in the local fluid rest frame we refer to as p_{in} , scatters off a quasiparticle from the QGP with momentum k , assumed to be in thermal equilibrium in the local fluid rest frame. (Note that in order to apply the formulae that we have presented in the Appendices, when we boost to the local fluid rest frame we must also rotate such that p_{in} lies along the z -axis, and when we later wish to boost back to the lab frame we must first undo this rotation. Note also that in order to compute the probability of Molière scattering during a specified time step, in the expressions from Section 3 and the Appendices we must employ the time step Δt_F in the local fluid rest frame.) If an elastic $2 \rightarrow 2$ scattering occurs, the outcome of this collision will be two partons, whose momenta in the local fluid rest frame are p and k_χ , specified as described in Appendix C. (One of these outgoing partons, most often the one with higher energy, is the scattered incident parton; the other is the scattered parton that originated from the medium.) It is important that in our Hybrid Model implementation of this physics we treat both outgoing partons fully dynamically. At all subsequent time steps, both are treated as jet partons meaning that both lose energy and momentum, both contribute to the creation of the jet wake, both experience strongly coupled soft Gaussian momentum broadening, and in principle either or both may experience a subsequent Molière scattering at a later time step. We also need to take into account that we have removed four-momentum k from the droplet of QGP by removing a thermal quasiparticle with this four-momentum and, after it scatters, counting it as a parton in the jet. This means that after freezeout the background of soft particles that is uncorrelated with the jet has k less four-momentum than it would have had absent the Molière scattering. Since we do not simulate the uncorrelated background, in order to preserve energy-momentum conservation we need to include a “hole” or “negative particle”

with four-momentum k (boosted back to the lab frame) when we compute experimental observables.

There are two remaining subtleties that need to be addressed in order to complete the Monte Carlo implementation of Molière scattering within the Hybrid Model. First, suppose that the parton in the shower that initiates a Molière scattering would have split later in the DGLAP evolution of the parton shower. After the Molière scattering, this parton has become two partons, both of which we are treating as elements of the parton shower; do these partons split later in the shower evolution? We have chosen the following prescription: (i) we make the scattered parton with the higher momentum split as and when would have happened absent the Molière scattering, with this component of the developing parton shower now pointing in the new direction set by the higher-energy parton emerging from the Molière scattering; and, (ii) we assume that the scattered parton with lower momentum (which is most likely the parton from the medium) does not split. Improving upon these prescriptions is a goal for future work, since in reality the Molière scattering will modify the subsequent DGLAP evolution of both scattered partons. Other possible prescriptions have been investigated in the literature [62–64].

The second subtlety that remains to be discussed relates to the hadronization of the parton shower in the Hybrid Model. In the Hybrid Model, some partons in the shower lose all (and all partons in the shower lose some) of their energy and momentum to the fluid. The energy and momentum from the parton shower that ends up in the jet wake is hadronized according to Eq. (4.3). Note that in many cases the softer of the two scattered partons coming out of a Molière scattering process subsequently loses all of its energy and momentum to the fluid, meaning that an important consequence of Molière scattering is the modification of the wake of the jet. What about the partons that remain in the shower after the Hybrid Model evolution, which is to say after the temperature of the medium in which they are propagating has dropped below 145 MeV? In the Hybrid Model before the present work, jet partons that do not lose all of their energy are hadronized using the Lund string model present in PYTHIA 8 [43], upon assuming for simplicity that these shower partons have retained the same color flow that they would have had in vacuum where a colorless configuration is needed between string endpoints (quarks) in order to produce the hadrons. With the addition of scattered partons coming from Molière scattering, we can no longer use this simplified assumption. In order to hadronize the surviving shower partons, in this work we use the “colorless hadronization prescription”, introduced by the JETSCAPE collaboration [65]. In essence, it consists of building up colorless strings based on a minimization procedure such that consecutive links are built between particles whose distance is minimal in (η, ϕ) -space. This procedure does not require knowledge of the original color labels of the shower partons, making it more consistent with the fact that interactions with the medium will randomly rotate the color of partons in the shower, rearranging their initial color flow configuration. For this reason, changing from hadronizing the surviving shower partons using the Lund string model from PYTHIA 8 to using the colorless hadronization prescription would be a small improvement to the Hybrid Model even without Molière scattering. Finally, we note that any “hole partons” (representing the removal of partons from the QGP by Molière scattering) are hadronized

separately, so as to be able to identify the contribution to the hadronic final state that needs to be subtracted relative to the background (hadrons that are uncorrelated with the jet). This also follows a prescription first introduced by the JETSCAPE collaboration [66].

Having described in full how we calculate the probability for and kinematics of weakly coupled large momentum transfer $2 \rightarrow 2$ elastic scattering (in previous Sections) and the way in which we implement these Molière scattering processes, which are sensitive to the microscopic particulate structure of QGP, in the Hybrid Model, we turn now to the study of their observable consequences.

5 Results

In this Section, we examine a suite of jet observables that have been studied extensively in the past, some groomed and some ungroomed, with the goal of identifying characteristic signatures of $2 \rightarrow 2$ Molière scatterings between jet partons and thermal QGP quasiparticles. Our purpose here is not to perform detailed comparisons with experimental data, but rather to compare Hybrid Model calculations of these observables with and without the inclusion of Molière scattering. In this way we can identify jet observables that are particularly sensitive to Molière scattering in heavy-ion collisions, and more generally that are particularly sensitive to weakly coupled scattering of jet partons off quark- and gluon-quasiparticles in QGP resolved at high momentum transfer.

In all twenty panels in the Figures in this Section, we show four curves corresponding to different implementations of the Hybrid Model in which Molière scatterings and jet wakes are switched on or off: “No Molière Scatterings & No Wake”, in black; “No Molière Scatterings & With Wake”, in blue; “With Molière Scatterings & No Wake”, in green; and “With Molière Scatterings & With Wake”, in red. This controlled Monte Carlo setup allows us to identify which observables and which regions of phase space are most sensitive to the physics of interest.

The first aspect we need to address is the choice of the parameters of the model. In the present setup, there are four parameters: (i) κ_{sc} , which enters via Eq. (4.1) controls the magnitude of the rate of strongly coupled energy loss experienced by partons in jet showers; (ii) K , which is defined in Eq. (4.4), controls the magnitude of the strongly coupled Gaussian-distributed soft transverse momentum broadening; (iii) the strong coupling constant g_s that controls the magnitude of the perturbative QCD matrix elements for Molière scattering; and (iv) the threshold parameter a which sets the minimum squared momentum transfer am_D^2 for the $2 \rightarrow 2$ elastic scatterings that we treat as weakly coupled, add to the Hybrid Model, and refer to as Molière scatterings.¹ Throughout this study, we choose $g_s = 2.25$ (corresponding to $\alpha_s \approx 0.4$), $a = 10$ and $K = 15$, as described in Section 4.2, as these are reasonable values for our purposes here, namely for identifying jet observables that are sensitive to Molière scattering. We are thus left with fixing κ_{sc} . In previous

¹The QCD coupling arising within the Debye mass (recall that $m_D^2 = \frac{3}{2}g^2T^2$ in QCD with $N_c = N_f = 3$) could be taken to have a different value than that the g_s arising in the Molière scattering matrix elements, since Molière scattering involves momentum transfers that are larger than thermal. Doing this would not represent adding an additional parameter, though, as it is equivalent to changing the value of a .

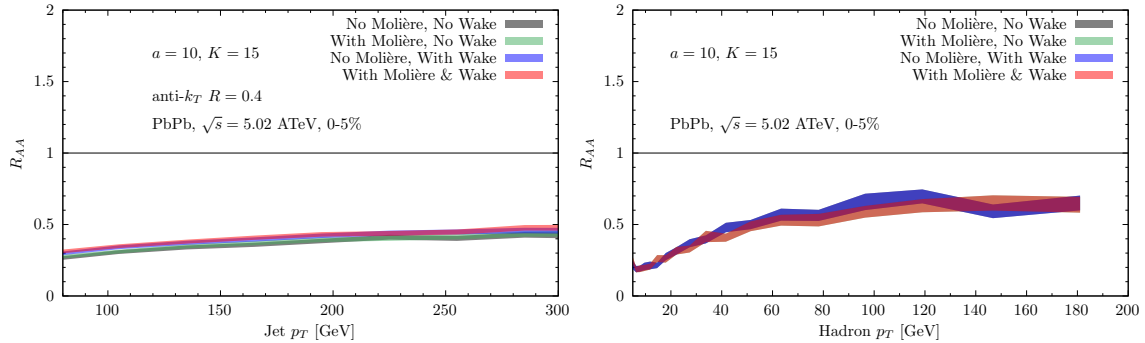


Figure 4: Left: Hybrid Model calculations of R_{AA} of inclusive anti- k_t jets with $R = 0.4$ as a function of jet p_T . Right: Hybrid Model calculations of R_{AA} of single inclusive charged hadrons with transverse momentum p_T . In both panels, R_{AA} is the suppression in PbPb collisions with 0-5% centrality and $\sqrt{s_{NN}} = 5.02$ TeV relative to pp collisions. The four colored bands show results from Hybrid Model calculations with and without Molière scattering with $g_s = 2.25$ and $a = 10$, and with and without the soft hadrons originating from jet wakes. Soft Gaussian transverse momentum broadening with $K = 15$ is included in all calculations. Calculations with Molière scattering (red and green bands) have the parameter that controls the magnitude of strongly coupled energy loss set to $\kappa_{sc} = 0.37$ so as to match prior calculations for jet and hadron suppression without Molière scattering (blue and black bands) calculated with $\kappa_{sc} = 0.404$, the value obtained by fitting Hybrid model calculations including jet wakes but without Molière scattering to data in Ref. [29].

work [29], we fixed κ_{sc} in the Hybrid Model without Molière scattering and with $K = 0$ by fitting to the experimental data on the suppression of jets and single charged hadrons in PbPb collisions relative to pp collisions available at that time, finding $\kappa_{sc}^{\text{no Molière}} = 0.404$. In future work, the values of κ_{sc} , K , g_s and a should be constrained together via a Bayesian uncertainty quantification that takes advantage of the many and varied experimental data sets available today. For the present study, upon choosing $K = 15$ and including Molière scattering with $g_s = 2.25$ and $a = 10$, we shall set $\kappa_{sc} = 0.37$. We do so because, as we shall see in Section 5.1, with this choice the suppression R_{AA} of jets and single hadrons is approximately the same as in the absence of Molière scattering with $\kappa_{sc}^{\text{no Molière}} = 0.404$, the value obtained by fitting to data in Ref. [29].

5.1 Jet and single hadron suppression, and introducing results to follow

In the left panel of Fig. 4 we show Hybrid Model calculations of jet R_{AA} for jets reconstructed with the anti- k_t algorithm [67, 68] and radius parameter $R = 0.4$. In the right panel, we show Hybrid Model calculations of the R_{AA} for charged hadrons. In the calculations without Molière scattering (black and blue curves) we have chosen $\kappa_{sc} = 0.404$. We have adjusted the value of κ_{sc} in the calculations that include Molière scattering (green and red) such that the jet R_{AA} and hadron R_{AA} are very similar when soft hadrons from jet wakes are included (red curves on top of blue curves) or are not included (green curves on top of black curves). This corresponds to choosing $\kappa_{sc} = 0.37$ when we include Molière

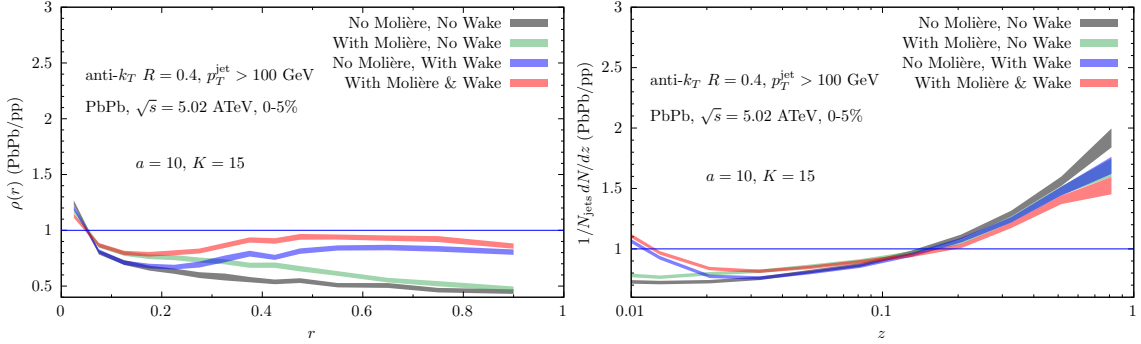


Figure 5: Hybrid Model results for the ratios between the jet shapes (left panel) and jet fragmentation functions (right panel) in PbPb collisions with $\sqrt{s_{\text{NN}}} = 5.02$ TeV and 0-5% centrality and pp collisions for inclusive samples of anti- k_t jets with $p_T^{\text{jet}} > 100$ GeV and $R = 0.4$.

scattering.

In the following subsections, we will investigate a series of ungroomed and groomed jet and jet substructure observables, keeping all parameters fixed as described here. Whenever we see an observable where the red and blue Hybrid Model calculations are similar to each other and well separated from the green and black Hybrid Model calculations, we will conclude that such an observable is more sensitive to jet wakes (a classic strongly coupled, soft, modification to jets that does not involve adding extra prongs) than to Molière scattering. And, whenever we see an observable where the red and green Hybrid Model calculations are similar to each other and well separated from the blue and black Hybrid Model calculations, we will conclude that such an observable is more sensitive to Molière scattering (our classic example of a weakly coupled, hard, modification to jets that does involve adding extra prongs).

Perhaps this goes without saying, but the black, green and blue curves in the Figures should not be compared to experimental data since it is impossible to turn either Molière scattering or jet wakes off in an experiment! The red curves may be compared to experimental data, ideally upon using measurements of many observables like those in the following subsections to fix the values of the four model parameters via a Bayesian uncertainty quantification analysis.

5.2 Two ungroomed observables

Having fixed the parameters in the model, we now begin by examining Hybrid Model results with and without Molière scattering for two of the most well-studied jet observables, namely the jet shape and the jet fragmentation function. Hybrid Model calculations of these observables were first presented in Ref. [27], where the (significant) observable consequences of jet wakes and the (small) consequences of soft Gaussian transverse momentum broadening were analyzed.

In the left panel of Fig. 5, we present the ratio between distributions of the jet shape in PbPb and pp collisions. The jet shape is an observable which measures the

distribution of hadronic transverse momentum relative to the jet axis. It is defined as $\rho(r) \equiv \langle \sum_i p_T^i(r)/p_T^{\text{jet}} \rangle$, where in our analysis we take the average $\langle \cdot \rangle$ among all jets that satisfy $p_T^{\text{jet}} > 100$ GeV. r is the distance in the (η, ϕ) plane between a charged particle i with $p_T^i > 1$ GeV and the jet axis, and is defined as $r = \sqrt{\Delta\eta^2 + \Delta\phi^2}$. Note that the sum over i need not be limited to those particles contained within the jet radius $R = 0.4$. The first thing that we observe is the marked narrowing near the jet core for all four curves. This is due to the selection bias in PbPb collisions towards those jets with a given p_T that lost the least energy, sometimes referred to as the survivor bias. Because the jet production cross-section falls steeply with p_T , the jets found with a given PbPb are more likely to be surviving jets which lost little energy than jets which would have had much more energy absent jet quenching. Since jets that have a narrower shape, and fewer harder fragments, lose less energy, we see that the ensemble of jets reconstructed in PbPb collisions are narrower (left panel of Fig. 5) and harder (right panel of Fig. 5, described below) than in pp collisions, as has been seen in many previous analyses [27–31, 34, 69–77].

Here, in the left panel of Fig. 5 we observe that including Molière scatterings, which can be seen by comparing the green curve to the black curve or by comparing the red curve to the blue curve, broadens the jet shape distribution in a way that partially compensates for its narrowing caused by the selection bias due to energy loss. It is clear that the narrowing of the shapes of jets found in PbPb collisions due to selection bias is a much larger effect than the broadening of these jets by Molière scattering. Furthermore, the effects of Molière scattering are also dwarfed by the effects of jet wakes (compare red and blue curves to black and green curves). Since the soft hadrons originating from jet wakes have a broad angular distribution, including them broadens the jet shape [27], and in an ungroomed observable like this one this effect is much larger than that of Molière scattering. We conclude that although Molière scattering does modify the jet shape distribution, this observable is not well-suited for identifying Molière scattering unambiguously in experimental data.

It is nevertheless interesting to observe that the effect of elastic scatterings is exhausted after $r \gtrsim 0.6$ radians, which gives us a ballpark estimate of the angle out to which the scattered partons from Molière scattering are to be found. The soft hadrons from jet wakes extend out to even larger angles, raising the large angle tail of the jet shape via the addition of soft hadrons coming from the region of QGP behind the jet that has picked up momentum in the direction of the jet. Their effect is largest where the hard particles originating from the (quenched) parton shower are absent, away from the jet core. We see that the effects of jet wakes, and to a lesser degree of Molière scattering, persist out to angles beyond the jet radius parameter, here $R = 0.4$, employed in reconstructing the sample of jets.

We obtain a similar story in the right panel of Fig. 5, where we compute PbPb/pp ratios of the jet fragmentation functions. The jet fragmentation function describes how the momentum of the jet is distributed among the momentum (in the direction of the jet) carried by each charged hadron in the jet. It is defined as the distribution of charged hadrons within the jet with $p_T > 1$ GeV with a given momentum fraction $z \equiv (p_T \cos r)/p_T^{\text{jet}}$, where r is defined as in the jet shape. For each charged hadron, $p_T \cos r$ is the component of its momentum in the jet direction. In this analysis, we average the fragmentation function

over all jets with $p_T^{\text{jet}} > 100$ GeV, and by definition it is normalized to the average number of charged tracks per jet.

In the right panel of Fig. 5 we see in jet fragmentation functions the manifestation of the same physical effects that we saw affecting jet shapes in the left panel. Selection bias towards jets that have lost less energy favors jets with a harder fragmentation function in PbPb collisions, pushing the PbPb/pp fragmentation function ratio up at large z and down at small z . This is the biggest effect. Jet wakes add soft hadrons, with small z . This has a significant effect on the fragmentation function at very low z . (Note that for a 100 GeV jet, $z \sim 0.01 - 0.02$ corresponds to hadrons with $p_T \sim 1 - 2$ GeV originating from jet wakes.) Because of the way that the fragmentation functions are defined, pushing the fragmentation function up at low z also results in pushing it slightly downwards at large z . As for the jet shape, effects of Molière scattering are visible in the fragmentation function ratio by comparing red to blue or green to black: a small decrease at large z and a small increase at lower z . We can observe that Molière scattering pushes the fragmentation function up all the way out to $z \sim 0.1$, meaning that the hadrons that result from these scatterings are harder than those originating from jet wakes. However, the effects of Molière scattering in this observable are so much smaller than the effects of jet wakes and selection bias that, here too, this ungroomed observable is not well-suited for identifying Molière scattering in experimental data.

From the study of these two important ungroomed jet observables we can draw several conclusions. First, Molière scattering does modify the shapes and fragmentation functions of jets, broadening the former and softening the latter. However, selection bias pushes the shapes and fragmentation functions of the samples of jets reconstructed in PbPb collisions more strongly in the opposite directions. These will not be the only observables where we will see effects of Molière scattering partially compensating for effects of selection bias due to energy loss. Second, in ungroomed observables where soft hadrons within the jets make a significant contribution, the soft hadrons from jet wakes modify jets in PbPb collisions relative to jets in pp collisions. This is of significant interest in its own right, but it represents a confounding effect if we are seeking observables with which to observe unambiguous consequences of Molière scattering in experimental data. This points us toward the strategy that we shall follow in the next subsections: analyze groomed observables, including observables that characterize semi-hard subjets within jets.

5.3 Groomed observables

In general terms, groomed jet observables refer to observables involving some algorithmic procedure that serves to remove some soft hadrons from the jets. In this subsection, we analyze three groomed jet observables that have been defined so as to exploit knowledge about the clustering history of a jet. The jet-finding algorithm that is most robust in the presence of an underlying event is the anti- k_t algorithm [67], as it preferentially clusters particles around a high- p_T constituent, which typically lies close to the true partonic jet axis. Once the jet and its constituents have been identified, however, one can probe its internal structure by reclustering the jet using a purely angular-ordered algorithm such as Cambridge–Aachen (C/A) [78, 79]. The C/A algorithm clusters particles based solely on

their angular separation, without reference to their momenta or energies. To leading logarithmic accuracy in the DGLAP evolution variable, vacuum parton showers exhibit strong angular ordering. As a result, when applied in reverse the C/A algorithm approximately reconstructs the splitting history of the jet. Each step in the clustering history can then be characterized by the momentum sharing fraction

$$z_{12} \equiv \frac{\min(p_{T,1}, p_{T,2})}{p_{T,1} + p_{T,2}}, \quad (5.1)$$

where $p_{T,1}$ and $p_{T,2}$ are the transverse momenta of the two branches being merged, and by their relative angular separation

$$R_{12} \equiv \sqrt{\Delta\eta_{12}^2 + \Delta\phi_{12}^2} \quad (5.2)$$

in (η, ϕ) space. The grooming procedures we describe were designed so as to reduce sensitivity to soft, nonperturbative, splittings within the parton shower by selecting a specified subset of these clustering steps. When applied to jets in heavy ion collisions, these grooming procedures also serve to remove most of the sort hadrons originating from jet wakes.

In particular, the Soft Drop grooming algorithm [80] identifies the first splitting within an anti- k_t jet of radius R that satisfies the condition

$$z_g > z_{\text{cut}} \left(\frac{R_{12}}{R} \right)^\beta, \quad (5.3)$$

where z_{cut} and β are parameters that specify the grooming algorithm. The angular separation R_{12} of this first splitting is referred to as R_g . The distributions of z_g and R_g for this first accepted splitting have been measured in pp collisions in Ref. [81] and Ref. [82], respectively, and have been measured in heavy-ion collisions by CMS [41, 81, 83], ALICE [84, 85], and ATLAS [86, 87]. A previous Hybrid Model analysis (without Molière scattering) shows almost no modification to the z_g distribution in heavy-ion collisions compared to pp, with $z_{\text{cut}} = 0.1$ [30], and we have checked that including Molière scattering does not modify this conclusion. (The origin of the soft z_g enhancement seen in experimental data that has not been unfolded [81] can be reproduced by embedding our results in a fluctuating background [88]. However, the distribution of the Soft Drop splitting angle, $(1/N) dN/dR_g$, was found to be significantly modified [30], an effect that is largely driven by selection bias, as has been discussed in theoretical studies [30, 34, 73, 74, 76, 89] and in papers reporting experimental measurements [41, 85] of the Soft Drop splitting angle. As we have seen, because of energy loss the jet sample in PbPb collisions becomes biased toward narrower, less-modified jets that retain a larger fraction of their original energy within the jet cone. This bias suppresses the contribution of jets with large opening angles and enhances the relative weight of narrow configurations in the sample of jets selected in PbPb collisions relative to that in pp collisions, thereby modifying the measured $(1/N) dN/dR_g$ distribution. Jets with larger R_g , which can in qualitative terms be thought of as jets with two semi-hard substructures separated by a larger angle R_g , lose more energy than jets with smaller R_g and so are less numerous among the jets in a given p_T -bin in PbPb collisions. The black and blue curves in the left panel of Fig. 6 serve to revisit these conclusions.

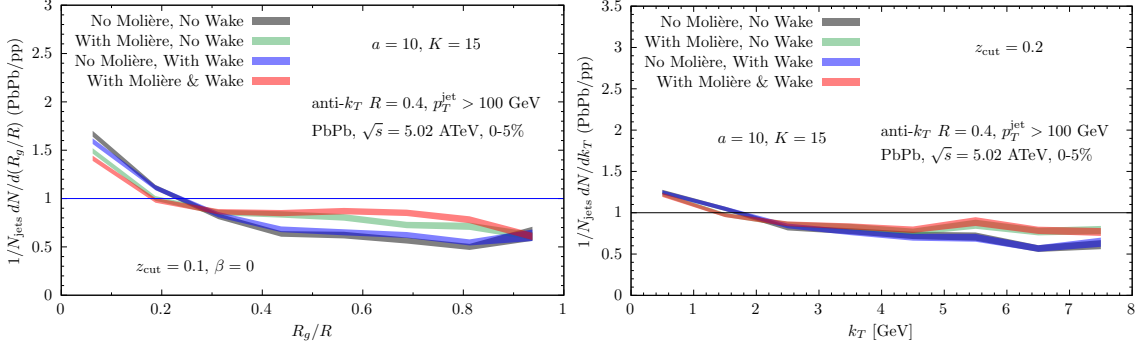


Figure 6: Left: Hybrid Model results for the ratios between the distribution $(1/N_{\text{jets}}) dN/d(R_g/R)$ of the scaled Soft Drop angle R_g/R (left panel) and the distribution $(1/N_{\text{jets}}) dN/dk_T$ of the k_T of the largest splitting (right panel) of jets in PbPb collisions with $\sqrt{s_{\text{NN}}} = 5.02$ TeV and 0-5% centrality and pp collisions for inclusive samples of anti- k_t jets with $p_T^{\text{jet}} > 100$ GeV and $R = 0.4$. In the left panel, the Soft Drop grooming procedure with $z_{\text{cut}} = 0.1$ and $\beta = 0$ is employed.

In the present work, we present Hybrid Model calculations of the Soft Drop angle R_g in heavy-ion collisions that include the effects of Molière scattering, see the red and green curves in the left panel of Fig. 6. This Figure shows Hybrid Model calculations of the ratio of distributions of the scaled Soft Drop angle R_g/R as measured in PbPb collisions to pp collisions for anti- k_t $R = 0.4$ jets with $p_T > 100$ GeV, calculated using grooming parameters $z_{\text{cut}} = 0.1$ and $\beta = 0$. We first note that — consistent with the results of Ref. [30] — the inclusion/exclusion of jet wakes has a negligible effect on the calculations shown. This confirms that since the hadrons which originate from the wake are soft they are largely groomed away by the Soft Drop grooming procedure. This validates our motivation for focusing on these observables, and allows us to focus on the effects of selection bias due to energy loss and Molière scattering. We then observe that including Molière scatterings in our model results in a broadening of the R_g/R distributions in PbPb collisions that is most notable towards the periphery of the jet, for $R_g \gtrsim 0.5R = 0.2$. In qualitative terms, this is consistent with what was found in the jet shape observable in the left panel of Fig. 5, but here the confounding effects of jet wakes are largely absent. We see that selection bias pushes the R_g distribution down at larger R_g/R and correspondingly pushes it up at small R_g/R , while Molière scattering acts in the opposite direction and partially counteracts the effects of selection bias due to energy loss.

In the right panel of Fig. 6, we present Hybrid Model calculations of PbPb/pp ratios of the distributions of an observable referred to as leading k_T [90], which is closely related to R_g and defined as follows. k_T is defined to be the splitting scale associated with the C/A reclustering step that maximizes

$$k_T \equiv z(1-z)p_T^{\text{parent}} \sin \theta, \quad (5.4)$$

where z is the momentum sharing fraction of the splitting, p_T^{parent} is the transverse momentum of the parent parton that splits, and θ is the opening angle between the two daughter

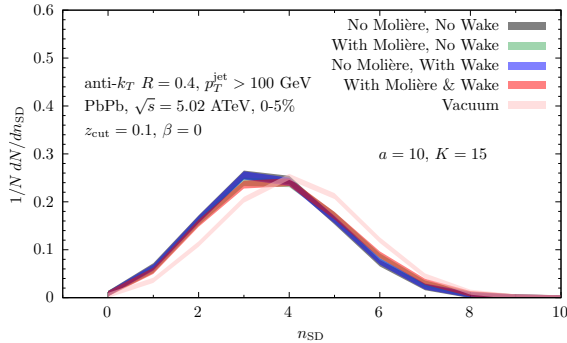


Figure 7: Hybrid Model calculations of the distributions of the number of splittings n_{SD} that satisfy the Soft Drop condition with $z_{\text{cut}} = 0.1$ and $\beta = 0$ within anti- k_t jets of radius $R = 0.4$ and $p_T^{\text{jet}} > 100$ GeV in 0-5% central PbPb collisions and pp collisions (pink curve) with $\sqrt{s_{\text{NN}}} = 5.02$ TeV. All distributions are normalized by the number of $R = 0.4$ jets.

partons after the splitting. Motivated by experimental considerations, we consider only splittings that satisfy $z > z_{\text{cut}} = 0.2$, thereby excluding highly asymmetric splittings. (In experimental data, lowering z_{cut} would increase the number of fake subjects arising from upward fluctuations in the QGP background.) Analogous to what we observed by studying the scaled Soft Drop angle R_g/R in the left panel of Fig. 6, the right panel of this Figure shows that the number of larger k_T splittings is reduced by selection bias due to energy loss, and is enhanced when Molière scatterings are included. Interestingly, recent measurements of the leading k_T observable by the ALICE Collaboration [91] exhibit sufficient sensitivity to discriminate between the inclusion and exclusion of Molière scatterings. This data should therefore definitely be included in any future Bayesian analysis in which experimental measurements of many observables are used to constrain the values of κ_{SC} , K , g_s and a .

In both panels of Fig. 6, we see the effects of Molière scattering only partially compensating for the effects of selection bias due to energy loss. This will make it challenging to use measurements of these observables to claim unambiguous evidence for the presence of Molière scattering. Molière scattering is a physical phenomenon that results in additional “prongs” in jets in PbPb collisions, meaning that more jets should be found with larger values of R_g/R and k_T in PbPb collisions than in pp collisions. Unfortunately, our Hybrid Model calculations show that the PbPb/pp ratios are elevated by Molière scattering, but remain less than one. This motivates looking at these observables in samples of jets that are selected in ways that reduce the bias favoring less modified jets. We will study Hybrid Model calculations of the R_g distribution in photon-tagged jet samples in subsection 5.5, with the goal of reducing the effects of selection bias. There we will also investigate jets with a larger radius R , where the effects of jet wakes are not completely removed and in fact an interesting interplay between jet wakes and Molière scattering is seen.

The first two groomed observables that we have examined focus on the properties of a single splitting, or single clustering step, of the shower. However, we know that each Molière scattering adds one parton to the jet shower and yields two scattered partons that

may have been scattered by a significant angle. This prompts us to ask whether Molière scattering increases the number of subjets within a jet — a question that we shall focus on in the next subsection. In the context of this subsection, though, we take a first look into this idea in Fig. 7 by asking whether Molière scattering increases the number of splittings n_{SD} that satisfy the Soft Drop splitting condition, as this is also a way of asking whether the number of semi-hard structures within a jet has been increased (by Molière scattering) in PbPb collisions relative to pp collisions. In Fig. 7 we present Hybrid Model calculations of the probability distribution of finding n_{SD} reclustering steps that satisfy the Soft Drop condition, with $z_{\text{cut}} = 0.1$ and $\beta = 0$. Jets in PbPb collisions are biased towards those that lost the least amount of energy, which tend to have fewer and narrower hard splittings. Thus, we observe a reduction in n_{SD} in the sample of jets selected in PbPb collisions when compared to that in pp collisions. Once again, jet wakes have almost no effect on this observable since the hadrons originating from jet wakes are too soft to pass the Soft Drop condition. Unfortunately, Molière scatterings have very little effect on n_{SD} , only slightly increasing n_{SD} . Hence, we do not believe that measurements of n_{SD} would be sensitive to the presence of Molière scatterings in PbPb collisions. However, other observables which examine multiple semi-hard structures within a jet may still hold promise for detecting and studying Molière scattering in heavy-ion collisions. These observables are the focus of the next subsection.

5.4 Jets within Jets

In the previous subsection, we saw that groomed substructure is sensitive to the effects of Molière scattering while remaining relatively insensitive to the effects of jet wakes (provided that the value of z_{cut} is large enough). In the present subsection we explore a different set of substructure observables, which examine the properties of (sub)jets of radius R_S contained within a larger jet of radius $R > R_S$ [92].

The procedure is as follows. First, we reconstruct anti- k_t jets of radius R . Then, using only those constituents that have been clustered into a given jet, we reconstruct anti- k_t jets with a specified smaller radius $R_S < R$. Given the specifics of the anti- k_t algorithm, it will tend to cluster first those particles with larger momenta, rendering it well-suited for finding the semi-hard structures that Molière scatterings can generate around the original jet axis. In the top panel of Fig. 8, we show the results of Hybrid Model calculations of the distribution of the number of subjets n_{SubJ} of radius $R_S = 0.1$ with $p_T^{\text{Sub}} > 10$ GeV found within $R = 0.4$ jets with $p_T^{\text{jet}} > 100$ GeV using this procedure. This distribution of the number of jets with n_{SubJ} subjets in pp collisions falls rapidly with increasing n_{SubJ} , where having just two subjets is half as likely as having only one subjet. Since jets in PbPb collisions are biased towards those that lost the least amount of energy and therefore those that contain narrower splittings, we observe an increased number of $R = 0.4$ jets containing only one subjet and a reduction in the number of $R = 0.4$ jets containing multiple subjets, compared to pp collisions.

We see in the top panel of Fig. 8 that the inclusion of Molière scatterings enhances the number of $R = 0.4$ jets with $n_{\text{SubJ}} > 1$. This enhancement arises because a hard $2 \rightarrow 2$ Molière scattering can transfer substantial transverse momentum to a thermal

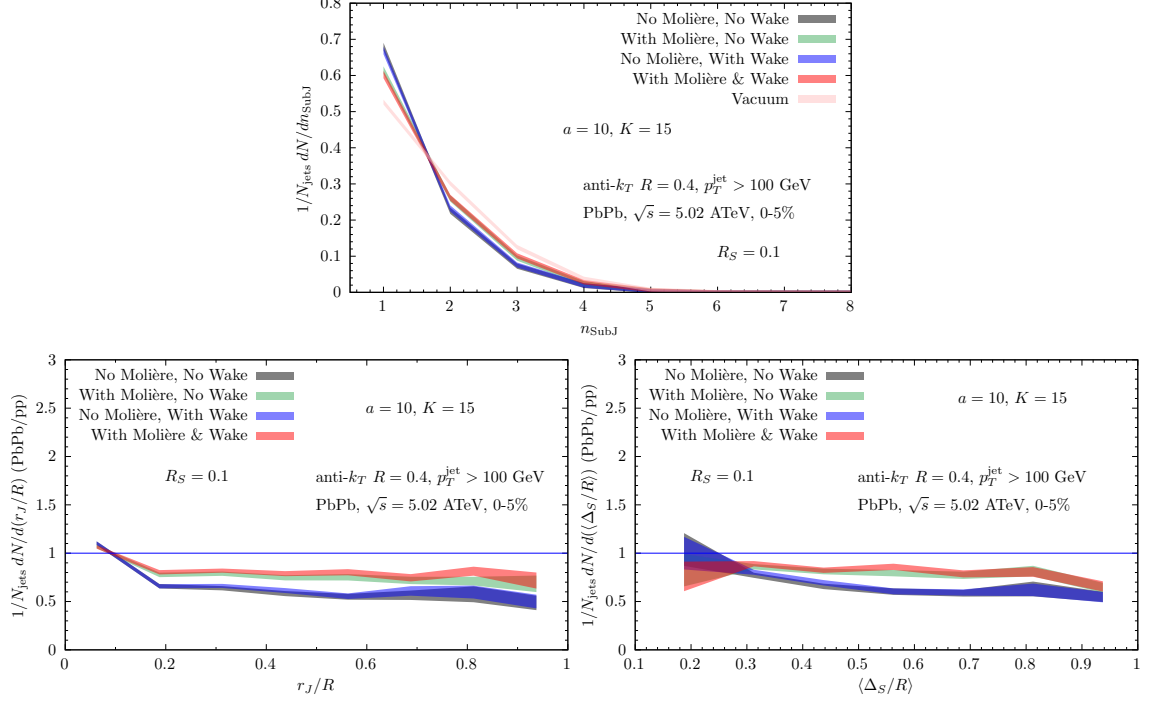


Figure 8: Top: Hybrid Model calculations of the distributions of n_{subJ} , the number of subjects of radius $R_S = 0.1$ with $p_T^{\text{Sub}} > 10$ GeV contained within anti- k_t jets of radius $R = 0.4$ and $p_T^{\text{jet}} > 100$ GeV in 0-5% central PbPb collisions and pp collisions (pink curve) with $\sqrt{s_{\text{NN}}} = 5.02$ TeV. Lower panels: Hybrid Model calculations of the ratios between the distributions of the angular separation r_J between the axis of a subject with $R_S = 0.1$ and the axis of the jet with $R = 0.4$ (lower left) and the angular separation Δ_S between pairs of subjects (lower right) in PbPb collisions and pp collisions.

parton, producing a semi-hard recoil at a sizable angle with respect to the original jet axis (and can also kick the jet parton that initiated the Molière scattering with a substantial transverse momentum). When either the recoiling parton kicked from the QGP or the scattered jet parton remains inside the jet with radius R and carries transverse momentum $p_T \gtrsim 10$ GeV, this may result in the reconstruction of one additional subject of radius R_S . Since the anti- k_t algorithm preferentially clusters high- p_T particles first, it efficiently resolves these semi-hard structures as independent subjects rather than merging them into the leading core. As a consequence, the probability of finding events with $n_{\text{SubJ}} > 1$ is enhanced when Molière scatterings are included. And indeed, the red and green curves in the top panel of Fig. 8 have been pushed toward larger n_{subJ} by Molière scattering. As is by now familiar, this happens only to a degree that partially compensates for the opposite effect arising from selection bias due to energy loss.

In addition to counting the number of subjects contained within an $R = 0.4$ jet, in the lower two panels of Fig. 8 we study the angular distribution of these subjects using two novel observables: (i) the angular separation r_J between the axis of an $R_S = 0.1$ subject and the axis of the $R = 0.4$ jet in which it is contained, and (ii) the angular separation

Δ_S between two $R_S = 0.1$ subjets within the same $R = 0.4$ jet. While n_{SubJ} counts the multiplicity of resolved subjets, $\langle \Delta_S \rangle$ and r_J quantify how far these subjets are separated from one another and from the central core of the jet. The kicks imparted by Molière scattering should serve to increase both Δ_S and r_J .

The bottom panels of Fig. 8 show the PbPb/pp ratios of the normalized distributions $(1/N_{\text{jets}}) dN/d(r_J/R)$ (left) and $(1/N_{\text{jets}}) dN/d(\langle \Delta_S/R \rangle)$ (right), where r_J is the angular separation in (η, ϕ) space between an $R = 0.1$ subjet and the axis of the containing $R = 0.4$ jet, and $\langle \Delta_S/R \rangle$ denotes the average angular separation between pairs of $R = 0.1$ subjets within an $R = 0.4$ jet. All distributions are normalized by the number of $R = 0.4$ jets. In the absence of Molière scatterings, the distributions are suppressed at moderate and large angular separations, reflecting the familiar selection bias toward jets with narrower hard substructures in PbPb collisions. While both observables show little sensitivity to jet wakes, they exhibit visible sensitivity to Molière scatterings. Hard $2 \rightarrow 2$ scatterings can deflect jet partons, broadening the jet, and can kick either jet partons or thermal partons out to sizable angles away from the central core of the jet. These recoiling partons and the wakes they excite can be reclustered into the $R = 0.4$ jet, and if so may then be reconstructed as an $R_S = 0.1$ subjet. This serves to increase both the radial distribution of subjets and the typical angular separation between them, in a way that — yet again — partially compensates for the opposite effect coming from selection bias.

Taken together, the results in Fig. 8 demonstrate that these jets-within-jets observables provide avenues toward the detection and study of Molière scattering off quasiparticles in QGP that are complementary to the groomed observables in the previous subsection. Unfortunately, all of the observables that we have examined so far in this and the previous subsection that focus on modifications to the number and distribution of semi-hard structures within jets suffer from significant confounding effects originating from jet selection bias due to energy loss. In the next subsection, we turn to photon-tagged jet observables in which this selection bias can be partially mitigated and, in some cases, even overcome by the effects of Molière scatterings.

5.5 Photon-tagged Jet Observables

Photon-tagged jet events provide a particularly clean probe of in-medium jet modification. Since the mean free path of photons passing through a droplet of QGP is larger than the size of that droplet formed in heavy-ion collisions, the photon does not interact with the medium or lose energy to it as a passing jet would. This means that when we choose our sample of jets to be those jets found in events in which a photon with a transverse momentum thus and so, selecting events based upon the photon energy introduces no bias favoring jets that lose less energy. Although we shall see that this is not a panacea, this significantly reduces the selection biases that affect inclusive jet measurements.

Note that photon-tagged jets in events with a photon with some p_T^γ , for example the jets in events with a photon with $p_T^\gamma > 150$ GeV, have a rather broad distribution of jet energies even in pp collisions. Of course the photon p_T is balanced by hadronic p_T , but this can be distributed among several jets and it includes soft radiation outside the jet cone(s). Because the jets in PbPb collisions have lost energy, the distribution of the momentum

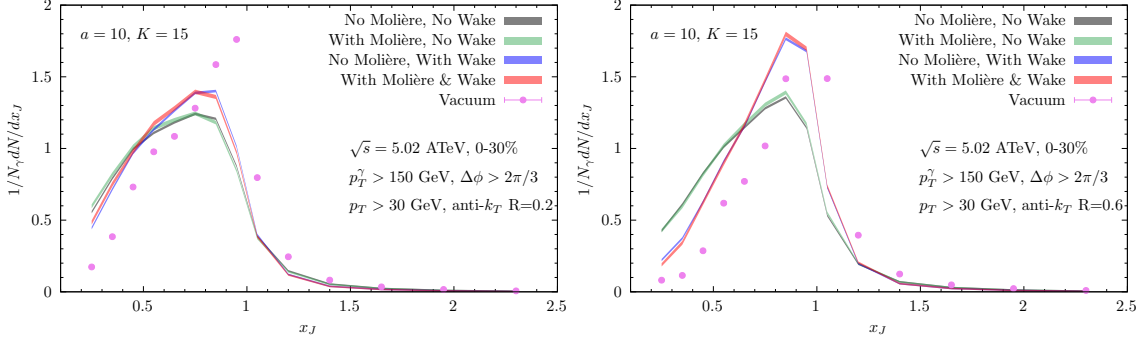


Figure 9: Hybrid Model results for the distributions $(1/N_\gamma) dN/dx_J$ of the photon-jet momentum imbalance variable $x_J \equiv p_T^{\text{jet}}/p_T^\gamma$ for photon-tagged jets with radii $R = 0.2$ (left) and $R = 0.6$ (right), with $p_T^\gamma > 150$ GeV, $\Delta\phi > 2\pi/3$, and $p_T^{\text{jet}} > 30$ GeV in pp (pink points) and 0–30% central PbPb collisions (colored bands) with $\sqrt{s_{\text{NN}}} = 5.02$ TeV.

imbalance variable $x_J \equiv p_T^{\text{jet}}/p_T^\gamma$ will be shifted toward lower x_J in PbPb collisions and will be even broader. To get a sense of this, and because this distribution will be important to understanding the distributions of observables like the Soft Drop angle R_g that we shall focus on below, we begin in Fig. 9 by plotting the x_J distributions for photon-tagged jets selected as follows. We first identify all events with a photon with $p_T^\gamma > 150$ GeV and $|\eta^\gamma| < 1.44$. If an event has multiple photons that satisfy this criteria, the photon with the highest p_T is selected as a reference for the photon-tagged jets in the event. We then require that this photon is “isolated”, which we define as having less than 5 GeV of transverse energy in a cone of $R = 0.4$ around the photon. If this photon is not isolated, then we discard the event altogether. For each selected, isolated photon, we then find and select the highest- p_T jet with $|\eta| < 2$ that is $\Delta\phi > 2\pi/3$ away from the selected photon. In Fig. 9, we show distributions $(1/N_\gamma) dN/dx_J$ of the number of jets within a given bin of x_J , normalized by the number of selected photons, for $R = 0.2$ (left panel) and $R = 0.6$ (right panel) in pp and 0–30% central PbPb collisions at $\sqrt{s_{\text{NN}}} = 5.02$ TeV.

In vacuum, the x_J distribution peaks close to unity, reflecting the importance of events where the photon and a single jet are nearly back-to-back, but the distribution is broad as we have already noted. In PbPb collisions, jet energy loss shifts the distribution toward smaller values of x_J , reflecting our expectation that jet showers which propagate through a droplet of QGP emerge with a reduced transverse momentum relative to that of the photon. The inclusion of Molière scatterings has very little effect on the x_J distributions in Fig. 9. Instead, the dominant modification comes from the inclusion of jet wakes. For both $R = 0.2$ and $R = 0.6$, turning on the wake shifts weight in the PbPb distribution toward larger values of x_J . The jet deposits energy and momentum into the droplet of QGP in the form of a wake; at freezeout, the jet wake becomes soft hadrons with a net momentum reflecting that lost by the jet; and, some of these soft hadrons are subsequently clustered into the jet reconstructed via the anti- k_t algorithm. This means that if we leave out the soft hadrons from jet wakes, the reconstructed jet p_T , and the imbalance x_J , are less than they are when we include jet wakes. Including jet wakes increases the reconstructed jet

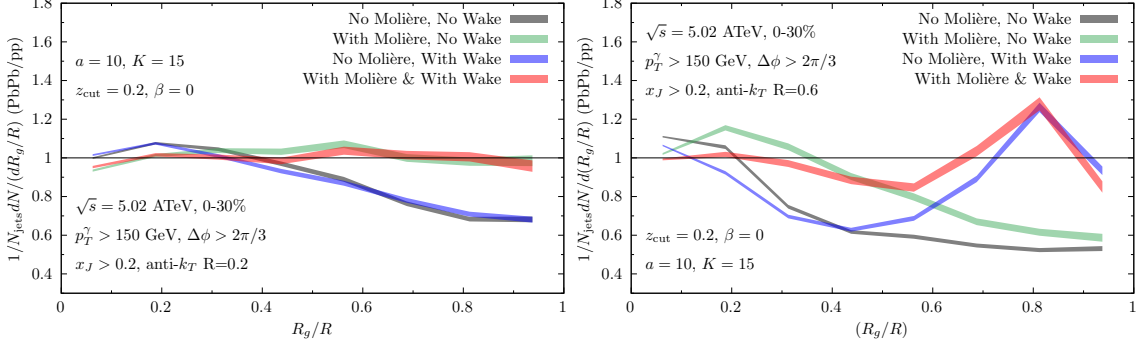


Figure 10: Hybrid Model calculations of the ratios of the distributions of the scaled Soft Drop angle R_g/R for $R = 0.2$ (left) and $R = 0.6$ (right) jets with $x_J > 0.2$ in photon-jet events with $p_T^\gamma > 150$ GeV and $\Delta\phi > 2\pi/3$ in 0-30% central PbPb collisions with $\sqrt{s_{NN}} = 5.02$ TeV to same in pp collisions.

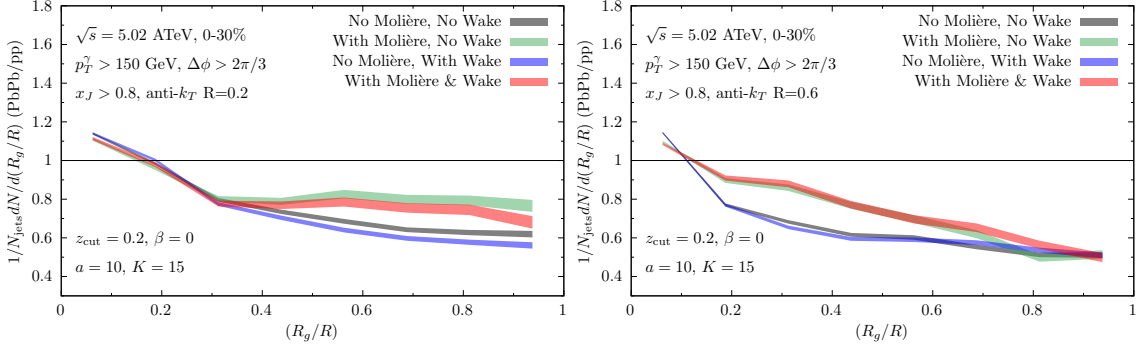


Figure 11: Same as Fig. 10, here for jets with $x_J > 0.8$: PbPb/pp ratios of the distributions of the scaled Soft Drop angle R_g/R for $R = 0.2$ (left) and $R = 0.6$ (right) jets with $x_J > 0.8$ in photon-jet events with $p_T^\gamma > 150$ GeV and $\Delta\phi > 2\pi/3$.

p_T , partially compensating for the energy lost by the hard shower to the medium. As expected, this effect is much more pronounced for jets reconstructed with the larger jet radius $R = 0.6$, as with $R = 0.6$ the jet reconstruction algorithm captures a substantially larger fraction of the wake than is the case if narrower $R = 0.2$ jets are reconstructed. The near overlap of the curves with and without Molière scattering, in both cases including jet wakes, indicates that rare hard elastic scatterings do not appreciably change the overall photon-jet momentum imbalance, even though they can leave clear signatures in more differential substructure observables. To this, we now turn.

With the motivations that we described at the end of the previous subsection, we return to analyzing Hybrid Model calculations of the Soft Drop angle R_g — now in photon-tagged jets. Since selecting events based upon the p_T^γ gives us a way to reduce selection biases, and since grooming suppresses soft wide-angle radiation, these observables are especially sensitive to semi-hard structures generated inside the jet by Molière scatterings. Fig. 10 shows the PbPb/pp ratio of $(1/N_{\text{jets}}) dN/d(R_g/R)$ for photon-tagged jets with $x_J > 0.2$, for $R = 0.2$ (left panel) and $R = 0.6$ (right panel) jets, with the Soft Drop grooming done

using parameters $z_{\text{cut}} = 0.2$ and $\beta = 0$. We note that including jets that have lost up to 80% of their transverse momentum to the medium ($x_J > 0.2$) allows us to significantly, but not completely, eliminate the selection bias due to energy loss. For example, we see from the left panel of Fig. 9 that there are some $R = 0.2$ jets with $x_J < 0.2$, many of which are highly modified jets that have lost more than 80% of their transverse momentum to the medium, and these jets are not included in the sample of jets selected for the R_g analysis in the left panel of Fig. 10. And indeed, we see a moderate narrowing of the R_g distribution in the black and blue curves in this panel, reflecting the effects of the remaining selection bias for $R = 0.2$ jets in the absence of Molière scattering. It is very pleasing to see, however, that in this case the bias coming from not selecting the jets that have lost the most energy is sufficiently modest that including Molière scattering (red and green curves) completely counteracts it.

We can confirm our understanding of the effects of selection bias by comparing the left panel of Fig. 10 to the left panel of Fig. 11 — where we have increased the bias by enforcing a stricter restriction of $x_J > 0.8$ on the selected jets. Indeed, the $x_J > 0.8$ selection increases the bias favoring jets with smaller R_g : we see that even when we include the effects of Molière scattering the R_g distribution in PbPb collisions remains depressed at larger R_g relative to that in pp collisions.

Drawing these elements together, we can now argue that if measurements in experimental data are aligned with what we have seen in the red bands in the left panels of Figs. 10, 11 and 9, this would in concert constitute strong evidence for Molière scattering. Measuring a PbPb/pp ratio of the Soft Drop angle R_g at (or even above) unity for jets with $x_J > 0.2$ in experimental data — as for the red band in the left panel of Fig. 10 — is of course the key element. Confirming the effects of selection bias by seeing the PbPb/pp ratio drop substantially when only jets with $x_J > 0.8$ are included in the sample — as in the left panel of Fig. 11 — is also central to the argument. The third element of the argument is a demonstration that even with $x_J > 0.2$ there must still be some degree of suppression of the PbPb/pp ratio of R_g arising from selection bias: this can be demonstrated by measuring the x_J distribution and seeing that — as in the left panel of Fig. 9 — selecting $x_J > 0.2$ leaves out the most modified jets, meaning that some effects of selection bias remain. That is, seeing the red band in the left panel of Fig. 9 together with comparing the red bands in Fig. 11 to that in Fig. 10 tells us that if we could remove *all* selection bias by extending the measurement down to $x_J > 0$ the PbPb/pp ratio of R_g would be above one — strong evidence for Molière scattering. Or, better to say it more generically, such measurements in concert would constitute strong evidence for hard scattering of jet partons off quasiparticles in the QGP. This would be an exciting indication that the particulate structure of QGP can be resolved by energetic partons in jets.

The CMS collaboration has come close to achieving this goal, in the measurements of R_g in photon-tagged jets that they have reported in Ref. [41] for which we had provided Hybrid Model predictions. They have selected events with $p_T^{\gamma} > 100$ GeV, which means that since reconstructing jets with p_T down to 20 GeV in PbPb collisions is prohibitively challenging they have only been able to select jets with $x_J > 0.8$ and $x_J > 0.4$. Their analysis shows clear evidence for greater effects of selection bias due to energy loss in the

$x_J > 0.8$ sample. For $x_J > 0.4$ the PbPb/pp ratio that they have measured is close to unity. It would be very interesting to see their x_J distribution, so as to estimate how large the remaining effects of selection bias are in their $x_J > 0.4$ sample, as this could strengthen evidence for Molière scattering. We hope, and anticipate, that by going up to $p_T^\gamma > 150$ GeV in future higher statistics data sets, as we have done in the Hybrid Model calculations in this paper, the LHC collaborations will be able to push down to $x_J > 0.2$.

We turn next to the Hybrid Model calculations for the PbPb/pp ratio of the Soft Drop angle R_g for the larger radius jets with $R = 0.6$ in the right panels of Figs. 10 and 11. Although jet wakes have a negligible effect on the modifications of R_g of $R = 0.2$ jets, for jets with the larger radius $R = 0.6$ the impact of jet wakes becomes much more pronounced, in particular at large $R_g \sim 0.5$, meaning $R_g/R \sim 0.8$, in the sample with $x_J > 0.2$ — see the red and blue bands in the right panel of Fig. 10. In the absence of jet wakes, we observe a strong suppression in the number of jets with large values of R_g/R . Molière scattering increases the number of jets with large R_g but the effects of Molière scattering diminish at the largest R_g , suggesting that it is rare for the scattered particles to be deflected away from the core of the jet by more than ~ 0.5 radians. At these largest angles, jet wakes have a very big effect in the right panel of Fig. 10 — but not in the right panel of Fig. 11 since when we include only jets with $x_J > 0.8$ in the sample we are excluding all jets that have lost any significant energy which means excluding all jets with significant wakes. The effects of jet wakes are amplified for larger- R jets because a greater fraction of the wake remains inside the jet cone, and because the Cambridge–Aachen declustering underlying Soft Drop is intrinsically sensitive to angular structure and is not sensitive to the momenta of jet constituents. Note that the behavior seen for $R_g/R < 0.3$ in the right panel of Fig. 10 is quite similar to what we see for $R_g/R < 0.9$ in the left panel — as these correspond to the same range of R_g . With $R = 0.6$ we can see larger values of R_g , where jet wakes make a dominant contribution for $x_J > 0.2$.

Comparing Figs. 10 and 11 makes it apparent that in photon-tagged events varying both the x_J selection and the jet radius R are useful dials, making the interplay between the effects of selection bias due to energy loss, jet wakes, and Molière scattering beautifully manifest. Going from $x_J > 0.2$ to $x_J > 0.8$ dials up the effects of selection bias. Going from $R = 0.2$ jets to $R = 0.6$ jets dials up the effects of jet wakes, in particular in the range $0.4 \lesssim R_g \lesssim 0.6$. And, the effects of Molière scattering are most prominent in $R = 0.2$ jets with $x_J > 0.2$, the left panel of Fig. 10.

A complementary way to quantify jet broadening in photon-tagged events is using the jet girth observable, $g = \int_0^R dr r \rho(r)$, which is simply the first moment of the jet shape. In practice, it is calculated as $g = \sum_i (p_{T,i}/p_T^{\text{jet}}) r_i$, where r_i denotes the angular distance of jet constituent i from the jet axis in (η, ϕ) space. Unlike R_g , which isolates a single splitting that passes the Soft Drop condition, the girth is sensitive to the full radial energy profile of the jet and therefore captures both semi-hard prongs and softer medium-induced radiation. In our calculation of g , we include all constituents of each jet without restricting the transverse momenta of the constituents, as appropriate for a calorimetric measurement. Fig. 12 shows the PbPb/pp ratio of $(1/N) dN/dg$ for photon-tagged jets with $x_J > 0.2$, for $R = 0.2$ (left panel) and $R = 0.6$ (right panel) jets. Fig. 13 presents the same jet girth

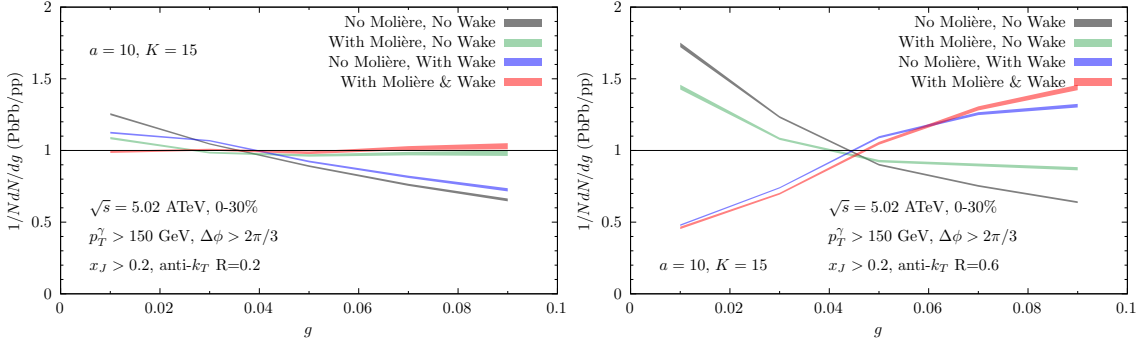


Figure 12: Hybrid Model calculations of the ratios of the distributions of the jet girth g for $R = 0.2$ (left) and $R = 0.6$ (right) jets with $x_J > 0.2$ in photon-jet events with $p_T^\gamma > 150$ GeV and $\Delta\phi > 2\pi/3$ in 0-30% central PbPb collisions with $\sqrt{s_{\text{NN}}} = 5.02$ TeV to the same in pp collisions.

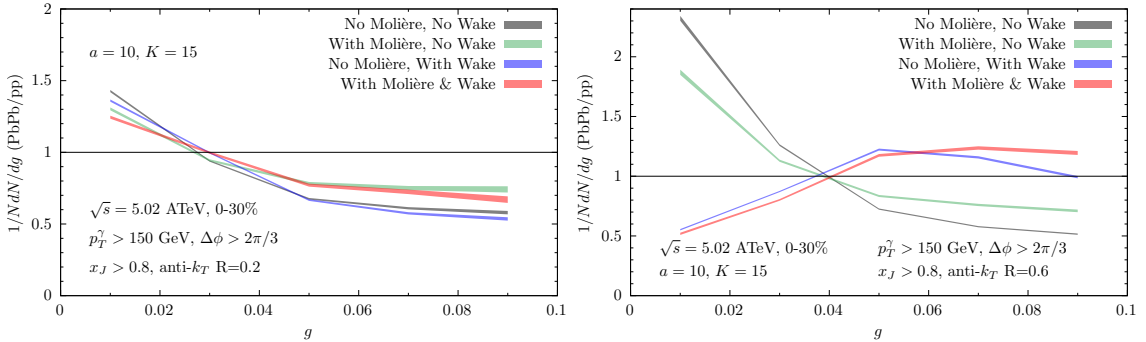


Figure 13: Same as Fig. 12, here for jets with $x_J > 0.8$: PbPb/pp ratios of the distributions of the jet girth g of $R = 0.2$ (left) and $R = 0.6$ (right) jets with $x_J > 0.8$ in photon-jet events with $p_T^\gamma > 150$ GeV and $\Delta\phi > 2\pi/3$.

observable in photon-tagged jets, but with the stricter jet selection $x_J > 0.8$. Comparing these two Figures to Figs. 10 and 11 makes it apparent that, although the results differ in detail, our Hybrid Model calculations of the jet girth observable are telling the same story that we have gleaned from our results for the Soft Drop angle R_g .

We begin with the left panel of Fig. 12. For $R = 0.2$ jets with $x_J > 0.2$, excluding Molière scatterings leads to a suppression of large- g configurations, consistent with the by-now-familiar narrowing of the distribution induced by selection bias and energy transported outside the narrow jet cone. Once Molière scatterings are included, however, the suppression at larger g is essentially completely eliminated, and the PbPb/pp ratio approaches or slightly exceeds unity at large values of g . This reflects the fact that rare hard Molière scatterings can redistribute energy to larger angles within the jet cone, increasing the jet's girth. In the left panel of Fig. 13 we see a suppression in the g distribution at larger g for photon-tagged jets in PbPb collisions regardless of whether Molière scatterings are included or excluded — reflecting the stronger effects of selection bias due to energy loss that are imposed when we restrict the jet sample to jets with $x_J > 0.8$. By comparing

the red and green bands to the blue and black bands in the left panels of both Figs. 12 and 13, we can see that for jets with $R = 0.2$ the increase in jet girth g arising from Molière scattering dominates over that arising from jet wakes, but it is only for the selection of jets with $x_J > 0.2$ in Fig. 12 that the effect of Molière scattering suffices to compensate for the opposite effect arising from selection bias.

One may wonder why turning the wake on/off made more of a difference for the jet shape observable in Fig. 5 than it does for the jet girth observable in the left panels of Figs. 12 and 13. After all, the jet girth is the first moment of the jet shape $\rho(r)$. If we examine Fig. 5, though, we notice that including/excluding the wake only makes a difference to the jet shape for values of $r > 0.2$. And, the left panels of Figs. 12 and 13 depict results for jets with $R = 0.2$. We conclude that it is the narrowness of these jets that is responsible for the effects of jet wakes on the girth distribution being negligible relative to the effects of Molière scattering.

And indeed, when we look at jets with $R = 0.6$ in the right panels of Figs. 12 and 13 we see a different story. For wider jets with $R = 0.6$, in both the $x_J > 0.2$ sample and the $x_J > 0.8$ sample the effects of jet wakes dominate over the effects of Molière scattering. When wakes are included, there is a pronounced enhancement of the PbPb/pp ratio above one for $g \gtrsim 0.04$, since the wake deposits energy and momentum in the form of soft hadrons at sizable angles relative to the jet axis that remain within the wide $R = 0.6$ jet cone. Including Molière scatterings on top of this further enhances the jet girth, as hard recoils and their wakes contribute additional weight at large angles, but for $R = 0.6$ jets this is a small effect compared to that of the jet wakes.

The one place where our Hybrid Model calculations of the girth observable tell a different story than that told by our calculations of the Soft Drop splitting angle R_g observable is in the right panel of Fig. 13. Here, unlike in the right panel of Fig. 11, even with the stricter requirement $x_J > 0.8$ we still observe a clear enhancement of the PbPb/pp ratio above one at $g \gtrsim 0.04$ once jet wakes are included. This reflects the fact that R_g is a groomed observable, in which the impact of the wake is reduced by grooming away soft jet constituents, whereas the girth includes all constituents weighted by their radial distance from the jet axis. Even though restricting the selection of jets to $x_J > 0.8$ eliminates most jets that have lost energy, enough remain in this wide jet sample that their wakes still have a significant effect on the girth distribution at $g \gtrsim 0.04$.

Just as in the case of the R_g/R observable, if measurements of the girth of jets with $R = 0.2$ selected with $x_J > 0.2$ and $x_J > 0.8$ in experimental data are aligned with what we have seen in the red bands in the left panels of Figs. 12, 13 and 9 this would in concert constitute strong evidence for Molière scattering. Measuring a PbPb/pp ratio of the girth g around unity for jets with $x_J > 0.2$, and confirming that there is still some degree of suppression of this ratio arising from selection bias by measuring the x_J distribution and by confirming the effects of selection bias by seeing the PbPb/pp ratio drop substantially when only jets with $x_J > 0.8$ are included would constitute strong evidence for hard scattering of jet partons off quasiparticles in the QGP.

Here, the CMS collaboration is *very* close to achieving this goal in their measurements of the girth g in photon-tagged jets in PbPb and pp collisions [41]. They have selected

events with $p_T^\gamma > 100$ GeV and have analyzed jet samples with $x_J > 0.4$ and $x_J > 0.8$. For $x_J > 0.4$, four of their five data points for the PbPb/ratio are close to unity, and their results show clear evidence for greater effects of selection bias in the $x_J > 0.8$ sample. Although they have not shown their x_J distribution which makes it hard to complete the story as in the preceding paragraph, two further aspects of their analysis and their data make the latter particularly tantalizing. First, nine of their ten data points are in good agreement with the Hybrid Model predictions that CMS showed in Ref. [41] — with Molière scattering included. And, second, their one data point that is not described by the Hybrid Model predictions, namely the PbPb/pp ratio in their highest girth bin with $0.08 < g < 0.1$ for jets with $x_J > 0.2$, is above the Hybrid Model calculation by more than three standard deviations and is more than two standard deviations above unity. This is of course only a single data point, and its large value may represent a statistical fluctuation. However, the only physical effect that we are aware of that can push the PbPb/pp ratio for girth (or R_g) in jets with a cone size as small as $R = 0.2$ above unity is hard scattering of jet partons off quasiparticles in the QGP. This makes this single data point a tantalizing data point. The whole suite of CMS measurements of both g and R_g in Ref. [41] motivate: (i) using these data in a future Bayesian analysis of multiple data sets to constrain the values of all four Hybrid Model parameters, including the two that tell us about Molière scattering; (ii) repeating these measurements with higher statistics; and (iii) repeating these measurements for jets produced in events with photons with $p_T^\gamma > 150$ GeV with $x_J > 0.2$, as in the Hybrid Model calculations that we have shown here. The very high CMS data point [41] for the PbPb/pp girth ratio for $0.08 < g < 0.1$ in jets with $x_J > 0.4$ only adds to these three motivations, as this enhancement, albeit at present only in a single bin of g , is consistent with the expectation that hard (Molière) scattering of jet partons off QGP quasiparticles increases the probability for hard constituents to appear at large angles within the jet.

6 Concluding Remarks and a Look Ahead

In this work, we have incorporated perturbative, high momentum-transfer $2 \rightarrow 2$ Molière scatterings between energetic jet partons and thermal quasiparticles into the Hybrid Model of jet quenching. Prior to this study, the Hybrid Model already included strongly coupled longitudinal energy loss, Gaussian transverse momentum broadening, and the hydrodynamic response of the medium to the passage of a jet in the form of a jet wake. By embedding rare, hard, elastic processes into this framework, we have constructed a description in which soft, strongly coupled interactions and rare, perturbative scatterings coexist within the same dynamical framework.

We began in Section 2 by reviewing perturbative calculations of Molière scattering for energetic partons traversing a droplet of QGP and generalized earlier results [39] by tracking both outgoing partons from the $2 \rightarrow 2$ process, rather than only the scattered jet parton. This extension is necessary for a realistic implementation in a jet-quenching framework, since both outgoing scattered partons (the one from the jet and the one from the QGP) continue to propagate through the medium, lose energy to it, excite wakes in

the QGP, and may scatter again. In Section 3 we identified the region of phase space in which $2 \rightarrow 2$ elastic scattering involves high momentum transfer making a weakly coupled description valid. We then constructed the probability distributions for the outgoing parton kinematics subject to the constraints $|t|, |u| > am_D^2$. Enforcing these constraints ensures that we are only including high momentum transfer scattering, which serves to restrict the allowed ranges of scattering angles and outgoing momenta. We provide full details of our calculation of Molière scattering and the resulting analytic expressions for the matrix elements, probability distributions, cumulative probabilities, and final state kinematics for these scattering processes in four Appendices.

With all of the groundwork in place, in Sec. 4 we incorporated these processes into the Hybrid Model by computing, at each timestep of the in-medium shower evolution, the probability that a hard scattering occurs and sampling the corresponding subprocess and final-state kinematics from these distributions, allowing rare Molière scatterings to be embedded dynamically throughout the Hybrid Model description of the evolution of a parton shower within an expanding cooling droplet of QGP. We imposed the conditions on the exchanged momentum of a $2 \rightarrow 2$ elastic scattering such that $|t|, |u| > am_D^2$, meaning that in adding Molière scattering, treated perturbatively, to the Hybrid Model we are only adding scattering processes with high momentum transfer. The strongly coupled continuous energy loss dE/dx (governed by a parameter κ_{sc}) and continuous soft Gaussian transverse momentum broadening (governed by a parameter K), incorporated in the Hybrid Model here as in previous work, serve together to model the strongly coupled dynamics of both elastic and inelastic soft momentum exchange between jet partons and the QGP liquid. In Section 4, we chose values $a = 10$ and $K = 15$ to ensure a smooth matching between the soft, continuous, Gaussian-distributed transverse momentum kicks and the hard, perturbative, momentum kicks from Molière scattering.

A key objective of this study has been to identify jet observables that are sensitive to the presence of Molière scatterings and, by extension, to the short-distance quasiparticle structure of the quark-gluon plasma. In Section 5, we adjusted the longitudinal energy loss parameter κ_{sc} so that Hybrid Model results for inclusive jet R_{AA} and charged hadron R_{AA} obtained here, with Molière scatterings included, are in good agreement with Hybrid Model results without Molière scattering that were fit to data. This ensured that any differences observed in jet substructure when we turn Molière scattering off/on arise from genuine modifications of the internal structure of jets, rather than from changes in overall suppression. We investigated such effects in two classic ungroomed jet observables, the jet shape and jet fragmentation function, as well as in observables obtained via two different grooming procedures and observables that focus on the number and angular distribution of subjects within jets. We then focussed particular attention on two observables, one groomed and one ungroomed, namely the Soft Drop angle R_g and the jet girth g , for jets produced in association with an isolated hard photon in a sample of events selected based upon the p_T of this photon.

We found that Molière scatterings generate potentially distinctive signatures in a myriad of differential jet substructure observables. In particular, observables that probe angular structure at sufficiently large angles — such as the Soft Drop angle R_g , leading- k_T split-

tings, subjet multiplicities, and angular separations between subjets — exhibit sensitivity to the presence of rare, large-angle, $2 \rightarrow 2$ elastic scatterings. However, we found that in inclusive jet samples (where the events are selected based upon the p_T of the jet therein) the effects of Molière scattering are obscured by the effects of jet selection bias — namely that the jets which are selected in any specified p_T bin are those that have lost the least amount of energy, which tend to be those jets with fewer and narrower splittings. This bias towards jets that survive their traverse of the QGP droplet most unscathed serves to push the distributions of all angular structure observables in PbPb collisions in a direction that favors narrower structures and suppresses broader structures relative to what is seen in pp collisions. Both Molière scattering and jet wakes have the opposite effect. Jet wakes predominantly modify softer and more diffuse components of the jets and enhance the distribution of hadronic energy out to large angles away from the central core of the jet. Molière scattering serves in addition to broaden the angular distribution of semi-hard structures as measured via the Soft Drop splitting angle R_g and subjets within jets.

When the selection bias due to parton energy loss is largely mitigated, for example in samples of high- p_T -photon-tagged jets selected so as to include jets down to small values of $x_J \equiv p_T^{\text{jet}}/p_T^\gamma$, the broadening of the Soft Drop splitting angle R_g and jet girth g distributions due to Molière scattering can potentially overcome the narrowing of these distributions due to jet selection bias, resulting in a net broadening of the Soft Drop splitting angle R_g and the jet girth g . Our Hybrid Model calculations show this happening for samples of narrow $R = 0.2$ jets with $x_J > 0.2$ in events in which the photon has $p_T^\gamma > 150$ GeV. Existing CMS measurements [41] of R_g and g of $R = 0.2$ photon-tagged jets recoiling against photons with $p_T^\gamma > 100$ GeV show strong evidence of the narrowing induced by selection bias in jet samples that satisfy $x_J > 0.8$. The fact that their PbPb/pp ratios for these two observables are close to unity in almost all bins of R_g/R and g in jet samples that satisfy $x_J > 0.4$ is tantalizing, with this ratio even well above unity in one g bin. Together with our results, this motivates relaxing the jet selection criteria further to $x_J > 0.2$ in future high-statistics measurements with higher photon transverse momenta so that one can see the enhancement in the number of photon-tagged jets with large R_g/R and large g in PbPb collisions relative to pp collisions — a definitive consequence of Molière scattering.

Our Hybrid Model calculations show that measurements of the scaled Soft Drop angle R_g/R and jet girth g in photon-tagged jets that are either skinny ($R = 0.2$) or broad ($R = 0.6$) in samples which either include jets that have lost most of their energy ($x_J > 0.2$) or exclude such jets ($x_J > 0.8$) can reveal a fascinating interplay between the effects of Molière scattering and jet wakes. In particular, we found that while measurements of the scaled Soft Drop angle R_g/R and jet girth g in samples of skinny $R = 0.2$ photon-tagged jets are especially sensitive to the effects of Molière scattering, the impact of jet wakes on these observables is comparatively modest. However, for photon-tagged jets with the larger radius $R = 0.6$, contributions from jet wakes become increasingly important, as a greater fraction of the soft, wide-angle medium response remains inside the jet cone and can lead to visible enhancements at large R_g/R and large values of the jet girth g . Furthermore, we found that these large-angle enhancements due to jet wakes are further amplified when Molière scatterings are included, because both outgoing partons produced in a Molière

scattering subsequently propagate through the plasma and each excites its own wake.

Taken together, our results demonstrate that Molière scatterings leave distinctive and measurable signatures in appropriately chosen jet substructure observables in PbPb collisions. This motivates a suite of near-term experimental measurements that can provide definitive evidence for weakly coupled hard scattering of jet partons off quasiparticles in the QGP. Our results also provide strong motivation for a quantitative confrontation between results obtained from Hybrid Model calculations including Molière scattering and experimental data, in particular for a Bayesian quantification of current constraints on the four Hybrid model parameters κ_{sc} , K , g_s and a that incorporates extant experimental data from measurements of (at least) all the observables that we have analyzed in this paper. This is the key next step needed in order to obtain a quantitative assessment of the effects of Molière scattering, namely to determine, with a quantitative estimate of the uncertainty, whether existing measurements (and, soon, the near-term measurements that our results motivate) reveal the presence of weakly coupled Molière scatterings and to quantitatively constrain the associated parameters of our model. Success in this regard would open the door to using future experimental data to quantify important improvements to our model, including an improved description of the properties and momentum distributions of QGP quasiparticles (which we have taken to be non-interacting quarks and gluons with thermal distributions in this exploratory study) and the addition of hard weakly coupled processes that go beyond $2 \rightarrow 2$.

In large collision systems such as PbPb, the observable impacts of Molière scattering compete with the observable impacts of energy loss, in particular via the resulting jet selection bias. In this context it is important to note that energy loss scales steeply with the in-medium path length L traversed by an energetic parton. The strongly coupled energy loss that we employ in the Hybrid Model with a rate dE/dx given in Eq. (4.1), a form based upon holographic calculations in strongly coupled quantum field theory scales parametrically as L^3 for $L \ll x_{\text{stop}}$, and then grows rapidly as L approaches the distance x_{stop} over which a jet parton thermalizes (unless it splits first). All effects of elastic scattering, including the probabilities for the high momentum transfer Molière scattering processes that are our focus in this paper, scale linearly with L . This means that the larger the droplet of QGP, the larger the effects of strongly coupled energy loss, including the effects of the consequent selection bias, will be relative to the effects of elastic Molière scattering. This parametric argument suggests that light-ion collisions, for example oxygen–oxygen (OO) collisions, could provide a particularly promising arena in which to search for signatures of Molière scattering off quasiparticles in QGP. The smaller characteristic size of QGP droplets in OO collisions reduces the available path length, suppressing the parametrically $\mathcal{O}(L^3)$ effects of strongly coupled energy loss more severely than the parametrically $\mathcal{O}(L)$ collisional effects, thereby amplifying the relative importance of the effects of Molière scattering processes in experimental observables. Recent oxygen–oxygen collisions at the LHC and RHIC, with the earliest measurements of hard probes in these systems having already appeared [93–95], present an exciting opportunity to use oxygen–oxygen collisions as an arena in which to detect and study Molière scatterings between energetic jet partons and quasiparticles in the medium.

More broadly, the detection of Molière scatterings in jet substructure observables would mark a significant advance in our understanding of quark-gluon plasma. It would constitute direct evidence that energetic jet partons resolve quark- and gluon-like quasiparticle at sufficiently short distance scales within QGP, an otherwise strongly coupled liquid. Observing such signatures would represent a concrete manifestation of asymptotic freedom in the strongly coupled matter produced in light- and heavy-ion collisions. And, it would open the door to using experimental measurements of jet substructure observables to systematically probe the microscopic, particulate, structure of hot quark-gluon plasma — the primordial liquid that filled the universe in the first microseconds after the Big Bang and that is recreated in these collisions.

Acknowledgments

We gratefully acknowledge helpful conversations with Harry Andrews, Cristian Baldenegro, Joao Barata, Hannah Bossi, Jasmine Brewer, Quinn Brodsky, Jorge Casalderrey-Solana, Leticia Cunqueiro, Francesco D’Eramo, Jean Du Plessis, Rithya Kunnawalkam Elayavalli, Gian Michele Innocenti, Peter Jacobs, Yen-Jie Lee, Arthur Lin, Xoan Mayo Lopez, Guilherme Milhano, Matthew Nguyen, Jaime Norman, Molly Park, Gunther Roland, Andrey Sadofyev, Bruno Scheihing Hitschfeld, Rachel Steinhorst, Adam Takacs, Marco van Leeuwen, Xiaojun Yao and Yi Yin. Research supported in part by the U.S. Department of Energy, Office of Science, Office of Nuclear Physics under grant Contract Number DE-SC0011090. DP acknowledges support from the Ramón y Cajal fellowship RYC2023-044989-I. ASK is supported by the National Science Foundation Graduate Research Fellowship Program under Grant No. 2141064.

A Decomposition of Subprocesses

Recall from Eqs. (2.20) and (2.21) from Sec. 2.2, which we repeat here, that the $2 \rightarrow 2$ elastic scattering amplitudes $|\mathcal{M}^{(n)}(t, u)|^2$ and $|\mathcal{M}^{(n)}(u, t)|^2$ can be decomposed into a linear combination of 7 terms m_i

$$\frac{1}{g_s^4} \left| \mathcal{M}^{(n)}(t, u) \right|^2 = \sum_i c_i^{(n)} m_i(t, u), \quad \frac{1}{g_s^4} \left| \mathcal{M}^{(\bar{n})}(u, t) \right|^2 = \sum_i \tilde{c}_i^{(\bar{n})} m_i(t, u), \quad (\text{A.1})$$

where the 7 terms m_i in question are

$$m_1 = \left(\frac{s}{t}\right)^2, \quad m_2 = -\left(\frac{s}{t}\right), \quad m_3 = 1, \quad m_4 = -\left(\frac{t}{s}\right), \quad m_5 = \left(\frac{t}{s}\right)^2, \quad (\text{A.2})$$

$$m_6 = -\left(\frac{t}{s+t}\right) = \frac{t}{u}, \quad m_7 = \left(\frac{t}{s+t}\right)^2 = \left(\frac{t}{u}\right)^2.$$

Using Table 1, we determine that each $c_i^{(n)}$ is given by the entry in the n -th row and i -th column of the matrix

$$\mathbf{C} = \begin{pmatrix} C_1 & C_2 - C_1 & C_1 + C_2 & 0 & 0 & C_1 + C_2 & C_1 \\ C_1 & C_2 - C_1 & C_1 + C_2 & 0 & 0 & C_1 + C_2 & C_1 \\ C_1 & -(C_1 + C_2) & C_1 + 2C_2 & -(C_1 + C_2) & C_1 & 0 & 0 \\ C_1 & -C_1 & C_1/2 & 0 & 0 & 0 & 0 \\ C_1 & -C_1 & C_1/2 & 0 & 0 & 0 & 0 \\ C_1 & -C_1 & C_1/2 & 0 & 0 & 0 & 0 \\ 0 & 0 & C_1/2 & -C_1 & C_1 & 0 & 0 \\ 0 & C_3 & -(C_3 + C_4) & 2C_4 & -2C_4 & C_3 & 0 \\ 2C_4 & -2C_4 & 2C_3 + C_4 & -C_3 & 0 & C_3 & 0 \\ 2C_4 & -2C_4 & 2C_3 + C_4 & -C_3 & 0 & C_3 & 0 \\ 2C_5 & -2C_5 & 4C_5 & -2C_5 & 2C_5 & 2C_5 & 2C_5 \end{pmatrix}, \quad (\text{A.3})$$

where

$$C_1 = 16(d_F C_F)^2/d_A, \quad (\text{A.4a})$$

$$C_2 = 2C_3 - C_4, \quad (\text{A.4b})$$

$$C_3 = 8d_F C_F^2, \quad (\text{A.4c})$$

$$C_4 = 8d_F C_F C_A, \quad (\text{A.4d})$$

$$C_5 = 8d_A C_A^2. \quad (\text{A.4e})$$

Swapping t and u , one can calculate that each $\tilde{c}_i^{(\tilde{n})}$ is given by the entry in the \tilde{n} -th row and i -th column of the matrix

$$\tilde{\mathbf{C}} = \begin{pmatrix} C_1 & C_2 - C_1 & C_1 + C_2 & 0 & 0 & C_1 + C_2 & C_1 \\ C_1 & C_2 - C_1 & C_1 + C_2 & 0 & 0 & C_1 + C_2 & C_1 \\ 0 & 0 & C_1 & C_2 - C_1 & C_1 & C_1 - C_2 & C_1 \\ 0 & 0 & C_1/2 & 0 & 0 & C_1 & C_1 \\ 0 & 0 & C_1/2 & 0 & 0 & C_1 & C_1 \\ 0 & 0 & C_1/2 & 0 & 0 & C_1 & C_1 \\ 0 & 0 & C_1/2 & -C_1 & C_1 & 0 & 0 \\ 0 & C_3 & -(C_3 + C_4) & 2C_4 & -2C_4 & C_3 & 0 \\ 0 & C_3 & C_4 & C_3 & 0 & 2C_4 & 2C_4 \\ 0 & C_3 & C_4 & C_3 & 0 & 2C_4 & 2C_4 \\ 2C_5 & -2C_5 & 4C_5 & -2C_5 & 2C_5 & 2C_5 & 2C_5 \end{pmatrix}. \quad (\text{A.5})$$

B Evaluating u at $k_T = k_T^{\min}$

In this Appendix, we derive Eq. (3.3), which gives the value of u at the kinematic endpoint $k_T = k_T^{\min}$ where the momentum k_T of the thermal parton participating in the elastic scattering takes on its minimum possible value, given the values of p_{in} , θ , and p . From Eq. (3.5), the Mandelstam variable u can be written as

$$u = t(C_u - D \cos \phi), \quad (\text{B.1})$$

with

$$2q^2 C \equiv (p_{\text{in}} + p)(k_T + k_\chi) + q^2, \quad C_u \equiv C - 1, \quad (\text{B.2})$$

and

$$2q^2 D \equiv \sqrt{(4p_{\text{in}}p + t)(4k_T k_\chi + t)}. \quad (\text{B.3})$$

Since $k_T^{\min} = (q - \omega)/2$ and $k_\chi = k_T + \omega$, at $k_T = k_T^{\min}$ we have

$$k_\chi \Big|_{k_T=k_T^{\min}} = \frac{q + \omega}{2}, \quad 4k_T^{\min} k_\chi \Big|_{k_T=k_T^{\min}} = q^2 - \omega^2. \quad (\text{B.4})$$

Using $t = \omega^2 - q^2$, it follows that $4k_T k_\chi + t = 0$ when $k_T = k_T^{\min}$, and therefore

$$D \Big|_{k_T=k_T^{\min}} = 0. \quad (\text{B.5})$$

As a result, u becomes independent of ϕ at this endpoint: $u(k_T = k_T^{\min}) = t C_u$. To evaluate C_u , note that at $k_T = k_T^{\min}$ we have $k_T + k_\chi = q$. Substituting into the definition of C gives $2q^2 C = (p_{\text{in}} + p)q + q^2 = q(p_{\text{in}} + p + q)$, so that

$$C \Big|_{k_T=k_T^{\min}} = \frac{p_{\text{in}} + p + q}{2q}, \quad C_u \Big|_{k_T=k_T^{\min}} = \frac{p_{\text{in}} + p - q}{2q}. \quad (\text{B.6})$$

Using $\omega = p_{\text{in}} - p$, the minimum momentum of the thermal parton in the medium can be written as $k_T^{\min} = (q - \omega)/2 = (q - p_{\text{in}} + p)/2$, which implies $p - k_T^{\min} = (p_{\text{in}} + p - q)/2$. Therefore,

$$C_u \Big|_{k_T=k_T^{\min}} = \frac{p - k_T^{\min}}{q}. \quad (\text{B.7})$$

Combining these results yields

$$u(k_T = k_T^{\min}) = t \frac{(p - k_T^{\min})}{q}, \quad (\text{B.8})$$

and hence

$$|u(k_T = k_T^{\min})| = \frac{|t| (p - k_T^{\min})}{q}, \quad (\text{B.9})$$

which is Eq. (3.3).

C Kinematics of Elastic $2 \rightarrow 2$ Scattering

In this Appendix, we outline a derivation of the kinematics necessary for a full description of each scattering process, once one has chosen values of the four variables $(x, \tilde{k}_\chi^{\min}, \tilde{k}, \phi)$ according to the appropriate probability distribution as described in Section 3.2. We are considering an incoming massless parton with four-momentum $p_{\text{in}}^\mu = (p_{\text{in}}, 0, 0, p_{\text{in}})$ that scatters elastically off a thermal parton carrying four-momentum $k^\mu = (k_T, \mathbf{k}_T)$. After the collision, the two resulting partons have momenta $p^\mu = (E, \mathbf{p})$ and $k_\chi^\mu = (E_\chi, \mathbf{k}_\chi)$. A generic $2 \rightarrow 2$ process with four massless particles would thus appear to have $4 \times 4 = 16$ real variables. However, the on-shell conditions for these massless partons remove four independent variables. Overall momentum conservation removes another four. Knowledge of \vec{p}_{in} fixes three variables. And, an overall rotation of the system about the \hat{z} axis can be fixed arbitrarily. Thus, the scattering process can be specified by four variables. As described in Sections 2 and 3, the straightforward choice for these four variables is: the outgoing momentum $p = |\mathbf{p}|$ of one of the partons in the final state, the angle θ of this outgoing parton relative to the direction of the incident jet parton, the transverse momentum exchange $k_T = |\mathbf{k}_T|$, and the angle ϕ between the two planes identified by the pair of vectors $(\mathbf{p}, \mathbf{p} - \mathbf{p}_{\text{in}})$ and $(\mathbf{p} - \mathbf{p}_{\text{in}}, \mathbf{k}_T)$.

In this Appendix, we shall describe how the complete kinematics of a $2 \rightarrow 2$ elastic scattering is determined from knowledge of the four variables p , θ , k_T , and ϕ . Before we do that, though, we describe how p , θ , k_T , and ϕ themselves are determined from the four variables x , \tilde{k}_χ^{\min} , \tilde{k} , and ϕ that we sample using the procedure outlined in Sec. 3.2. First, we state the obvious: ϕ is one of the sampled variables and is unchanged. Second, using Eq. (3.9) and the facts that $|t| = am_D^2/x$ and $k_T = k_T^{\min} + \tilde{k}T$, we identify

$$k_T = \frac{|t|}{4\tilde{k}_\chi^{\min}T} + \tilde{k}T = \frac{am_D^2}{4x\tilde{k}_\chi^{\min}T} + \tilde{k}T. \quad (\text{C.1})$$

Third, using Eq. (3.13) and the fact that $p = p_{\text{in}} - \omega$, we write

$$p = p_{\text{in}} - \tilde{k}_\chi^{\min}T + \frac{|t|}{4\tilde{k}_\chi^{\min}T} = p_{\text{in}} - \tilde{k}_\chi^{\min}T + \frac{am_D^2}{4x\tilde{k}_\chi^{\min}T}. \quad (\text{C.2})$$

Finally, since $|t| = 2p_{\text{in}}p(1 - \cos\theta)$, we identify

$$\theta = \arccos\left(1 - \frac{|t|}{2p_{\text{in}}p}\right). \quad (\text{C.3})$$

In the remainder of this Appendix, we will show how, via energy-momentum conservation, knowledge of the four variables p , θ , k_T , and ϕ serves to specify the complete kinematics of a $2 \rightarrow 2$ elastic scattering process. We work in the frame where $\mathbf{p}_{\text{in}} = p_{\text{in}}\hat{z}$ and place \mathbf{p} in the (x, z) plane, meaning that the angle θ between \mathbf{p}_{in} and \mathbf{p} is an angle in this plane: $\mathbf{p} = (p \cos\theta)\hat{z} + (p \sin\theta)\hat{x}$. Conservation of momentum then relates the three components of the recoil momentum \mathbf{k}_χ to the three components of the momentum \mathbf{k}_T of the struck thermal particle:

$$k_{\chi x} = k_{Tx} - p \sin\theta \quad (\text{C.4})$$

$$k_{\chi y} = k_{T y} \quad (\text{C.5})$$

$$k_{\chi z} = k_{T z} - p \cos \theta + p_{\text{in}} . \quad (\text{C.6})$$

$$(\text{C.7})$$

Conservation of energy can then be cast as a relationship between $k_{T z}$ and $k_{T x}$:

$$k_T(p - p_{\text{in}}) + k_{T z} p_{\text{in}} + p p_{\text{in}} - p(k_{T z} + p_{\text{in}}) \cos \theta - k_{T x} p \sin \theta = 0 . \quad (\text{C.8})$$

We can obtain a second relationship between $k_{T z}$ and $k_{T x}$ by noting that, by definition,

$$\cos(\phi) = \frac{(\mathbf{p} \times \mathbf{q}) \cdot (\mathbf{k}_T \times \mathbf{q})}{|\mathbf{p} \times \mathbf{q}| |\mathbf{k}_T \times \mathbf{q}|}, \quad (\text{C.9})$$

where $\mathbf{q} = \mathbf{p} - \mathbf{p}_{\text{in}}$, and writing Eq. (C.9) in the form

$$k_{T x} p_{\text{in}} - k_{T x} p \cos \theta + k_{T z} p \sin \theta = \cos \phi \sqrt{k_T^2 q^2 - (k_{T z} p_{\text{in}} - k_{T z} p \cos \theta - k_{T x} p \sin \theta)^2}. \quad (\text{C.10})$$

With one minor caveat, the two equations (C.8) and (C.10) together with knowledge of $k_T \equiv |\mathbf{k}_T|$ specifies $k_{T x}$, $k_{T y}$ and $k_{T z}$, which then means that via Eqs. (C.4), (C.5) and (C.6) we have also specified $k_{\chi x}$, $k_{\chi y}$ and $k_{\chi z}$. The minor caveat is that since neither Eq. (C.8) nor Eq. (C.10) depends on $k_{T y}$, the sign of $k_{T y}$ is not specified, but we can choose this sign arbitrarily. Explicit solution of Eqs. (C.8) and (C.10) then yields:

$$k_{T x} = 2 \cos \phi (p_{\text{in}} - p \cos \theta) \frac{p p_{\text{in}}}{q^2} \sin \frac{\theta}{2} \sqrt{\frac{k_T k_{\chi}}{p p_{\text{in}}} - \sin^2 \frac{\theta}{2}} + \frac{p \sin \theta}{2} \left(1 + \frac{k_T^2 - k_{\chi}^2}{q^2} \right) \quad (\text{C.11})$$

$$k_{T y} = 2 \sin \frac{\theta}{2} \sin \phi \frac{p p_{\text{in}}}{q} \sqrt{\frac{k_T k_{\chi}}{p p_{\text{in}}} - \sin^2 \frac{\theta}{2}} \quad (\text{C.12})$$

$$k_{T z} = \frac{1}{2} (-p_{\text{in}} + p \cos \theta) \left(\frac{k_T^2 - k_{\chi}^2}{q^2} + 1 \right) + 2 \cos \phi \frac{p^2 p_{\text{in}}}{q^2} \sin \theta \sin \frac{\theta}{2} \sqrt{\frac{k_T k_{\chi}}{p p_{\text{in}}} - \sin^2 \frac{\theta}{2}}. \quad (\text{C.13})$$

This completes the specification of the momenta of all four particles involved in the $2 \rightarrow 2$ scattering process.

D Integrals

Section 3.2 outlines the procedure for choosing the kinematic variables ϕ , \tilde{k} , $\tilde{k}_{\chi}^{\text{min}}$, and x from the appropriate probability distributions via computing the conditional distribution functions P_i , where i runs from 1 to 7, given in Eqs. (3.25), (3.26), (3.27) and (3.28), and the associated cumulative distribution functions. The procedure requires us to perform successive integrals over each of the kinematic variables. The total probability that a Molière scattering occurs in a timestep Δt requires one performing one additional integral over x , as in Eq. (3.23) and then adding the probabilities with appropriate weights as discussed below that equation.

The purpose of this Appendix is to describe the explicit calculation of these integrals. The arguments of these integrals are $m_i^{D,B}(t, u)|\mathcal{J}|P_u$, where $\mathcal{P}_u = \Theta(|u| - am_D^2)$ enforces the constraint $|u| > am_D^2$ from Eq. (3.2), $|\mathcal{J}|$ is the Jacobian resulting from the change of variables given in Eq. (3.17), and the $m_i^{D,B}$ are defined in Eq. (3.21). There, each $m_i^{D,B}$ is written in terms of functions m_i which depend on the Mandelstam variables:

$$\begin{aligned} m_1 &= \frac{s^2}{t^2} = (C - D \cos \phi)^2, & m_2 &= -\frac{s}{t} = C - D \cos \phi, & m_3 &= 1, \\ m_4 &= -\frac{t}{s} = (C - D \cos \phi)^{-1}, & m_5 &= \frac{t^2}{s^2} = (C - D \cos \phi)^{-2}, & & \\ m_6 &= \frac{t}{u} = (C_u - D \cos \phi)^{-1}, & m_7 &= \frac{t^2}{u^2} = (C_u - D \cos \phi)^{-2}, & & \end{aligned} \quad (\text{D.1})$$

with C , D and C_u as defined in Eqs. (3.6), (3.7), and (3.8). As discussed in Section 3.1, the constraint $|u| > am_D^2$ can be cast in the form (3.15), which we repeat here:

$$\mathcal{P}_u = \Theta(|u| - am_D^2) = \Theta(C_u - x - D \cos \phi). \quad (\text{D.2})$$

It is useful to decompose this Heaviside function into three regimes of the variable \tilde{k} , as follows. There are three kinematic regimes for which $C_u - x - D \cos \phi > 0$ can potentially be satisfied:

- (i) If $(C_u - x)/D \geq 1$, the inequality is satisfied for all ϕ and hence $\mathcal{P}_u = 1$.
- (ii) If $-1 < (C_u - x)/D < 1$, the inequality is satisfied only for $\phi \in (\phi_u, 2\pi - \phi_u)$ where

$$\phi_u \equiv \arccos\left(\frac{C_u - x}{D}\right) \in (0, \pi), \quad (\text{D.3})$$

and the constraint \mathcal{P}_u in Eq. (D.2) is equivalent to

$$\mathcal{P}_u = \Theta(\phi - \phi_u)\Theta(2\pi - \phi_u - \phi). \quad (\text{D.4})$$

- (iii) If $(C_u - x)/D \leq -1$, the inequality is never satisfied, meaning that $\mathcal{P}_u = 0$.

The boundaries between (i) and (ii) and between (ii) and (iii) occur when $D^2 - (C_u - x)^2 = 0$, which defines two solutions $\tilde{k}^\pm \equiv \frac{1}{T} \left(\sqrt{k_u(x+1)} \pm \sqrt{(k_u + q)x} \right)^2$, where we have defined $k_u \equiv p - k_T^{\min}$, meaning that $\tilde{k}_u = \tilde{k} + \tilde{p} - \tilde{k}_T$.

When $\tilde{k} > \tilde{k}^+$, $\mathcal{P}_u = 1$. When $\tilde{k}^- < \tilde{k} < \tilde{k}^+$, $\mathcal{P}_u = 1$ if and only if $\cos \phi < (C_u - x)/D$. And if $\tilde{k} < \tilde{k}^-$, then one might expect $\mathcal{P}_u = 0$. However, this third case is more nuanced than that because it is only valid when $D > 0$. If $D = 0$, then the quantity $(C_u - x)/D$ is ill-defined. $D = 0$ when $\tilde{k} = 0$, which occurs when $k_T = k_T^{\min}$. Eq. (3.3) implies that $u(\tilde{k} = 0) = |t|k_u/q$. Thus, $|u(\tilde{k} = 0)| > am_D^2$ is satisfied if and only if $k_u > qx$. So, when $0 < \tilde{k} < \tilde{k}^-$, $\mathcal{P}_u = 0$ and when $\tilde{k} = 0$, $\mathcal{P}_u = \Theta(\tilde{k}_u - \tilde{q}x)$. (Note that $\tilde{k}_u < \tilde{q}x$ for $0 < \tilde{k} < \tilde{k}^-$, whereas when $\tilde{k} = 0$ it is possible that $\tilde{k}_u > \tilde{q}x$. This means that in fact $\mathcal{P}_u = \Theta(\tilde{k}_u - \tilde{q}x)$ for all $\tilde{k} < \tilde{k}^-$.) In light of all of these considerations, we see that the

constraint $|u| > am_D^2$, namely Eq. (D.2), takes different forms in different regimes of \tilde{k} and can be written explicitly in terms of our variables as a sum of Heaviside Θ functions like so:

$$\mathcal{P}_u = \Theta(\tilde{k} > \tilde{k}^+) + \Theta\left(\frac{C_u - x}{D} > \cos\phi\right) \Theta(\tilde{k}^+ > \tilde{k} > \tilde{k}^-) + \Theta(\tilde{k}_u - \tilde{q}x) \Theta(\tilde{k}^- > \tilde{k}). \quad (\text{D.5})$$

There are three terms in Eq. (D.5), which correspond to the three different regimes of the momentum variable k . We will refer to these three terms as $\mathcal{P}_{u1}, \mathcal{P}_{u2}, \mathcal{P}_{u3}$ in order from highest to lowest k . Thus, $\mathcal{P}_u = \mathcal{P}_{u1} + \mathcal{P}_{u2} + \mathcal{P}_{u3}$.

We can further expand the Heaviside function $\Theta(\tilde{k}_u - \tilde{q}x) = \Theta(|u(k=0)| - am_D^2)$ that arises in \mathcal{P}_{u3} as

$$\Theta(\tilde{k}_u - \tilde{q}x) = \Theta\left(k_\chi^{\text{min}+} > k_\chi^{\text{min}} > k_\chi^{\text{min}-}\right) \Theta\left(\frac{p_{\text{in}}^2}{am_D^2} - 1 > x\right) \Theta(p_{\text{in}}^2 - am_D^2), \quad (\text{D.6})$$

where

$$k_\chi^{\text{min}\pm} \equiv \frac{p_{\text{in}} \pm \sqrt{p_{\text{in}}^2 - am_D^2(1+x)}}{2(1+x)}. \quad (\text{D.7})$$

D.1 ϕ Integrals

We begin with the conditional probability distributions $P_i(\phi)$ in Eq. (3.28), and the cumulative probability distributions obtained by integrating these: $\int_0^\phi d\phi' P_i(\phi')$. The necessary integrals over ϕ are all of the form

$$A \int \frac{d\phi}{2\pi} (C - D \cos\phi)^n \mathcal{P}_u, \quad (\text{D.8})$$

where A is a placeholder for all factors which do not depend on ϕ . In this subsection where we focus on doing the ϕ integrals, we will omit A from our expressions. We define the following function of ϕ and z , which will be useful throughout:

$$\varphi(\phi, z) = 2\pi \left[\frac{\phi}{2\pi} + \frac{1}{2} \right] + 2\arctan\left(\sqrt{\frac{z+1}{z-1}} \tan\left(\frac{\phi}{2}\right)\right). \quad (\text{D.9})$$

Then,

$$\int (C - D \cos(\phi))^{-2} \frac{d\phi}{2\pi} = \frac{C}{(C^2 - D^2)^{3/2}} \left(\frac{\varphi(\phi, C/D)}{2\pi} + \frac{D}{2\pi C} \frac{\sqrt{C^2 - D^2} \sin(\phi)}{C - D \cos(\phi)} \right), \quad (\text{D.10a})$$

$$\int (C - D \cos(\phi))^{-1} \frac{d\phi}{2\pi} = \frac{1}{\sqrt{C^2 - D^2}} \frac{\varphi(\phi, C/D)}{2\pi}, \quad (\text{D.10b})$$

$$\int \frac{d\phi}{2\pi} = \frac{\phi}{2\pi}, \quad (\text{D.10c})$$

$$\int C - D \cos(\phi) \frac{d\phi}{2\pi} = \frac{C\phi - D \sin(\phi)}{2\pi}, \quad (\text{D.10d})$$

$$\int (C - D \cos(\phi))^2 \frac{d\phi}{2\pi} = \frac{C^2\phi - 2CD \sin(\phi) + D^2(\phi/2 + \sin(2\phi)/4)}{2\pi}. \quad (\text{D.10e})$$

Since \mathcal{P}_{u1} and \mathcal{P}_{u3} are independent of ϕ ,

$$\int_0^\phi \frac{d\phi'}{2\pi} m_i (\mathcal{P}_{u1} + \mathcal{P}_{u3}) = (\mathcal{P}_{u1} + \mathcal{P}_{u3}) \int_0^\phi \frac{d\phi'}{2\pi} m_i \quad (\text{D.11})$$

Defining $\phi_u \equiv \arccos[(C_u - x)/D] \in (0, \pi)$, we have

$$\int_0^\phi \frac{d\phi'}{2\pi} m_i \mathcal{P}_{u2} = \Theta(\tilde{k}^+ > \tilde{k} > \tilde{k}^-) \left(\int_{\phi_u}^\phi \Theta(\phi > \phi_u) + \int_\phi^{2\pi - \phi_u} \Theta(\phi > 2\pi - \phi_u) \right) \frac{d\phi'}{2\pi} m_i \quad (\text{D.12})$$

From the definitions of C , D , and C_u in terms of the kinematic variables, we obtain

$$\sqrt{C \pm D} = \frac{\sqrt{(\tilde{k}_u + \tilde{q})(\tilde{k} + \tilde{q})}}{\tilde{q}} \pm \frac{\sqrt{\tilde{k}_u \tilde{k}}}{\tilde{q}}; \quad \sqrt{C^2 - D^2} = \frac{\tilde{k} + \tilde{k}_u + \tilde{q}}{\tilde{q}} \quad (\text{D.13a})$$

$$\sqrt{C_u \pm D} = \left| \frac{\sqrt{\tilde{k}_u(\tilde{k} + \tilde{q})}}{\tilde{q}} \pm \frac{\sqrt{(\tilde{k}_u + \tilde{q})\tilde{k}}}{\tilde{q}} \right|; \quad \sqrt{C_u^2 - D^2} = \frac{|\tilde{k} - \tilde{k}_u|}{\tilde{q}}. \quad (\text{D.13b})$$

Finally, if we define $\mathcal{P}_{u13} \equiv \mathcal{P}_{u1} + \mathcal{P}_{u3} = \Theta(k > k^-) + \Theta(k < k^-)\Theta(\tilde{k}_u - \tilde{q}x)$, then we may use Eqs. (D.10) to determine every integral of $m_i \mathcal{P}_u$ over ϕ , obtaining

$$\int_0^{2\pi} \frac{d\phi'}{2\pi} m_1 \mathcal{P}_u = \mathcal{P}_{u13} \left(C^2 + \frac{D^2}{2} \right) - \Theta(\tilde{k}^+ > \tilde{k} > \tilde{k}^-) \int_0^{\phi_u} \frac{d\phi'}{\pi} (C - D \cos(\phi'))^2, \quad (\text{D.14a})$$

$$\int_0^{2\pi} \frac{d\phi'}{2\pi} m_2 \mathcal{P}_u = \mathcal{P}_{u13} C - \Theta(\tilde{k}^+ > \tilde{k} > \tilde{k}^-) \int_0^{\phi_u} \frac{d\phi'}{\pi} (C - D \cos(\phi')), \quad (\text{D.14b})$$

$$\int_0^{2\pi} \frac{d\phi'}{2\pi} m_3 \mathcal{P}_u = \mathcal{P}_{u13} - \Theta(\tilde{k}^+ > \tilde{k} > \tilde{k}^-) \frac{\phi_u}{\pi}, \quad (\text{D.14c})$$

$$\int_0^{2\pi} \frac{d\phi'}{2\pi} m_4 \mathcal{P}_u = \mathcal{P}_{u13} \frac{1}{\sqrt{C^2 - D^2}} - \Theta(\tilde{k}^+ > \tilde{k} > \tilde{k}^-) \int_0^{\phi_u} \frac{d\phi'}{\pi} (C - D \cos(\phi'))^{-1}, \quad (\text{D.14d})$$

$$\int_0^{2\pi} \frac{d\phi'}{2\pi} m_5 \mathcal{P}_u = \mathcal{P}_{u13} \frac{C}{(C^2 - D^2)^{3/2}} - \Theta(\tilde{k}^+ > \tilde{k} > \tilde{k}^-) \int_0^{\phi_u} \frac{d\phi'}{\pi} (C - D \cos(\phi'))^{-2}, \quad (\text{D.14e})$$

$$\int_0^{2\pi} \frac{d\phi'}{2\pi} m_6 \mathcal{P}_u = \mathcal{P}_{u13} \frac{1}{\sqrt{C_u^2 - D^2}} - \Theta(\tilde{k}^+ > \tilde{k} > \tilde{k}^-) \int_0^{\phi_u} \frac{d\phi'}{\pi} (C_u - D \cos(\phi'))^{-1}, \quad (\text{D.14f})$$

$$\int_0^{2\pi} \frac{d\phi'}{2\pi} m_7 \mathcal{P}_u = \mathcal{P}_{u13} \frac{C_u}{(C_u^2 - D^2)^{3/2}} - \Theta(\tilde{k}^+ > \tilde{k} > \tilde{k}^-) \int_0^{\phi_u} \frac{d\phi'}{\pi} (C_u - D \cos(\phi'))^{-2}. \quad (\text{D.14g})$$

The prefactor A in Eq. (D.8) arises from two sources: (i) the Jacobian associated with the change of integration variables $(p, \theta, k_T, \phi) \rightarrow (x, \tilde{k}_{\min}^x, \tilde{k}, \phi)$, and (ii) the thermal

occupation factors $n_D(k_T)[1 \pm n_B(k_\chi)]$. In Sec. 3.1, the phase-space measure transforms as

$$\int dp d\theta dk_T d\phi P_t P_u \longrightarrow \int_0^1 dx \int_0^{p_{\text{in}}} d\tilde{k}_{\text{min}}^\chi \int_0^\infty d\tilde{k} \int_0^{2\pi} d\phi P_u |J|. \quad (\text{D.15})$$

As per Eq. (3.18), the Jacobian $|J|$ is proportional to $\eta/(\tilde{k}_T^{\text{min}} x)$, with $\eta^{-1} \equiv (4\pi)^3 \tilde{p}_{\text{in}}^2$. Furthermore, the integrand contains the product

$$n_D(k_T) [1 \pm n_B(k_\chi)], \quad k_\chi = k_T + \omega, \quad (\text{D.16})$$

with

$$n(k) = \frac{1}{e^{k/T} \mp 1}. \quad (\text{D.17})$$

This can be rewritten algebraically as

$$\begin{aligned} n_D(k_T) [1 \pm n_B(k_T + \omega)] &= \frac{1}{e^{k_T/T} \mp_D 1} \left(1 \pm_B \frac{1}{e^{(k_T+\omega)/T} \mp_B 1} \right) \\ &= \frac{e^{k_T/T}}{(e^{k_T/T} \mp_D 1)(e^{k_T/T} \mp_B e^{-\omega/T})}. \end{aligned} \quad (\text{D.18})$$

Thus, the Jacobian and the thermal weights yield the prefactor

$$A = \eta \frac{\tilde{k}_T^{\text{min}}}{x} \frac{e^{k_T/T}}{(e^{k_T/T} \mp_D 1)(e^{k_T/T} \mp_B e^{-\omega/T})}. \quad (\text{D.19})$$

Therefore, upon restoring the explicit expression for the factor of A from Eq. (D.8) means that all the integrals (D.14) take the form

$$\mathcal{I}_\phi^{(i)} \equiv \eta \frac{\tilde{k}_T^{\text{min}}}{x} \frac{e^{k_T/T}}{(e^{k_T/T} \mp_D 1)(e^{k_T/T} \mp_B e^{-\omega/T})} \left(\int_0^{2\pi} \frac{d\phi'}{2\pi} m_i P_u \right). \quad (\text{D.20})$$

Given values for \tilde{k} , $\tilde{k}_\chi^{\text{min}}$, and x , we can then employ these seven integrals (D.20) (one for each value of i) to choose the value of ϕ according to the appropriate conditional probability distribution using the method described in Section 3.2.

D.2 \tilde{k} Integrals

Next, in order to compute the cumulative distribution for the conditional probability $P(\tilde{k})$ in Eq. (3.27) or in order to compute the conditional probability $P(\tilde{k}_\chi^{\text{min}})$ in Eq. (3.26), we need to write the expression (D.20) in terms of $\tilde{k} = \tilde{k}_T - \tilde{k}_T^{\text{min}}$ and then integrate over \tilde{k} , which is equivalent to integrating $\mathcal{I}_\phi^{(i)}(\tilde{k}_T)$ from Eq. (D.20) over \tilde{k}_T starting from \tilde{k}_T^{min} :

$$\int_0^\infty d\tilde{k} \mathcal{I}_\phi^{(i)}(\tilde{k} + \tilde{k}_T^{\text{min}}) = \int_{\tilde{k}_T^{\text{min}}}^\infty d\tilde{k}_T \mathcal{I}_\phi^{(i)}(\tilde{k}_T). \quad (\text{D.21})$$

To this we now turn. Upon defining

$$\delta \equiv \pm_D e^{(-q+\omega)/(2T)} = \pm_D e^{-k_T^{\text{min}}/T} \quad (\text{D.22})$$

$$\beta \equiv \pm_B e^{(-q-\omega)/(2T)} = \pm_B e^{-k_x^{\min}/T}. \quad (\text{D.23})$$

we obtain

$$\int_{\tilde{k}_T^{\min}}^{\infty} d\tilde{k}_T \mathcal{I}_\phi^{(i)} = \frac{\eta e^{-\tilde{k}_T^{\min}} \tilde{k}_T^{\min}}{x} \int_0^{\infty} d\tilde{k} \frac{e^{\tilde{k}}}{(e^{\tilde{k}} - \delta)(e^{\tilde{k}} - \beta)} \left(\int_0^{2\pi} \frac{d\phi}{2\pi} m_i \mathcal{P}_u \right) \quad (\text{D.24a})$$

$$= \frac{\eta e^{-\tilde{k}_T^{\min}} \tilde{k}_T^{\min}}{x} \sum_{n=1}^{\infty} \frac{\delta^n - \beta^n}{\delta - \beta} \int_0^{\infty} d\tilde{k} e^{-n\tilde{k}} \left(\int_0^{2\pi} \frac{d\phi}{2\pi} m_i \mathcal{P}_u \right). \quad (\text{D.24b})$$

Many of the required integrals take the form

$$\int d\tilde{k} \frac{e^{\tilde{k}} (\tilde{k} + \tilde{k}_u + \tilde{q})^j}{(e^{\tilde{k}} - \delta)(e^{\tilde{k}} - \beta)} = \frac{-1}{\delta - \beta} \sum_{n=1}^{\infty} \frac{(\delta e^{\tilde{k}_u + \tilde{q}})^n - (\beta e^{\tilde{k}_u + \tilde{q}})^n}{n^{j+1}} \Gamma(j+1, n(\tilde{k} + \tilde{k}_u + \tilde{q})). \quad (\text{D.25})$$

If we were able to integrate over the whole range, many of these would simplify upon using the polylogarithm identity

$$\int_0^{\infty} d\tilde{k} \frac{e^{\tilde{k}} \tilde{k}^n}{(e^{\tilde{k}} - \delta)(e^{\tilde{k}} - \beta)} = n! \frac{Li_{n+1}(\delta) - Li_{n+1}(\beta)}{\delta - \beta}. \quad (\text{D.26})$$

What makes this more complicated is the \mathcal{P}_u on the right-hand side of Eq. (D.24b), as the decomposition $\mathcal{P}_u = \mathcal{P}_{u1} + \mathcal{P}_{u2} + \mathcal{P}_{u3}$ in Eq. (D.5) results in different expressions in each of the ranges $\tilde{k} < \tilde{k}^-$, $\tilde{k}^- < \tilde{k} < \tilde{k}^+$, and $\tilde{k}^+ < \tilde{k}$, which we must handle in turn.

We begin by considering the range $\tilde{k}^- < \tilde{k} < \tilde{k}^+$, where the integrals in Eq. (D.24b) are of the form

$$\int_{\tilde{k}^-}^{\tilde{k}} d\tilde{k} e^{-n\tilde{k}} \int_0^{\phi_u(\tilde{k})} \frac{d\phi'}{2\pi} (C - D \cos(\phi'))^m, \quad (\text{D.27})$$

where n and m are integers. The boundaries of the range in \tilde{k} that we are considering are given by the expressions $\tilde{k}^\pm = \frac{1}{T} \left(\sqrt{k_u(x+1)} \pm \sqrt{(k_u+q)x} \right)^2$, which can be expanded so as to yield

$$\tilde{k}^\pm = \left(\tilde{k}_u + x(2\tilde{k}_u + \tilde{q}) \right) \pm 2\sqrt{\tilde{k}_u(\tilde{k}_u + \tilde{q})x(x+1)}. \quad (\text{D.28})$$

We then define the midpoint \tilde{k}_0 and halfwidth Δ_k of the interval $[\tilde{k}^-, \tilde{k}^+]$ by

$$\tilde{k}_0 \equiv \frac{\tilde{k}^+ + \tilde{k}^-}{2}, \quad \Delta_k \equiv \frac{\tilde{k}^+ - \tilde{k}^-}{2}. \quad (\text{D.29})$$

We may then identify

$$\tilde{k}_0 = \tilde{k}_u + x(2\tilde{k}_u + \tilde{q}), \quad (\text{D.30})$$

$$\Delta_k = 2\sqrt{\tilde{k}_u(\tilde{k}_u + \tilde{q})x(x+1)}, \quad (\text{D.31})$$

and rewrite Eq. (D.28) as

$$\tilde{k}^\pm = \tilde{k}_0 \pm \Delta_k. \quad (\text{D.32})$$

Having defined Δ_k and \tilde{k}_0 , we can also define an angle ψ by

$$\Delta_k \sin \psi \equiv \sqrt{(\tilde{k}^+ - \tilde{k})(\tilde{k} - \tilde{k}^-)}, \quad \Delta_k \cos \psi \equiv \tilde{k} - \tilde{k}_0. \quad (\text{D.33})$$

upon noting that

$$(\Delta_k \sin \psi)^2 + (\Delta_k \cos \psi)^2 = (\tilde{k}^+ - \tilde{k})(\tilde{k} - \tilde{k}^-) + (\tilde{k} - \tilde{k}_0)^2 \quad (\text{D.34})$$

$$= (\tilde{k}_0 + \Delta_k - \tilde{k})(\tilde{k} - \tilde{k}_0 + \Delta_k) + (\tilde{k} - \tilde{k}_0)^2 \quad (\text{D.35})$$

$$= \left[\Delta_k^2 - (\tilde{k} - \tilde{k}_0)^2 \right] + (\tilde{k} - \tilde{k}_0)^2 \quad (\text{D.36})$$

$$= \Delta_k^2. \quad (\text{D.37})$$

The following identities, computed using the definitions of \tilde{k}^\pm and k_u from above and q from Eq. (2.16), will prove useful:

$$\sqrt{\tilde{k}^+ \tilde{k}^-} = |\tilde{k}_u - x\tilde{q}| \quad (\text{D.38a})$$

$$\sqrt{(\tilde{k}^+ + \tilde{q})(\tilde{k}^- + \tilde{q})} = \tilde{k}_u + (x+1)\tilde{q} \quad (\text{D.38b})$$

$$\sqrt{\tilde{k}^\pm + \tilde{q}} = \sqrt{(\tilde{k}_u + \tilde{q})(x+1)} \pm \sqrt{\tilde{k}_u x} \quad (\text{D.38c})$$

$$\sqrt{\tilde{k}^\pm} = \left| \sqrt{\tilde{k}_u(x+1)} \pm \sqrt{(\tilde{k}_u + \tilde{q})x} \right| \quad (\text{D.38d})$$

Furthermore, we can rewrite $\phi_u = \arccos[(C_u - x)/D]$, identify $D \sin(\phi_u)$, and calculate $d\phi_u/d\psi$ as

$$\phi_u = \arctan \left(\frac{\tilde{q}x - \tilde{k}_u}{\tilde{k}^+} \tan \frac{\psi}{2} \right) + \arctan \left(\frac{\tilde{q}x + \tilde{k}_u + \tilde{q}}{\tilde{k}^+ + \tilde{q}} \tan \frac{\psi}{2} \right) \quad (\text{D.39a})$$

$$D \sin(\phi_u) = \sqrt{D^2 - (C_u - x)^2} = \frac{1}{\tilde{q}} \sqrt{(\tilde{k} - \tilde{k}^-)(\tilde{k}^+ - \tilde{k})} = \frac{\Delta_k}{\tilde{q}} \sin \psi \quad (\text{D.39b})$$

$$\frac{d\phi_u}{d\psi} = \frac{d\phi_u}{d\tilde{k}} \frac{d\tilde{k}}{d\psi} = \frac{1}{2} \left(\frac{x\tilde{q} - \tilde{k}_u}{\tilde{k}} + \frac{x\tilde{q} + \tilde{k}_u + \tilde{q}}{\tilde{k} + \tilde{q}} \right). \quad (\text{D.39c})$$

Using Eq. (D.39b), we note that at $\tilde{k} = \tilde{k}^\pm$, $D^2 - (C_u - x)^2 = 0$. That is, $(C_u - x)/D = \pm 1$ at $\tilde{k} = \tilde{k}^\pm$. So, $\phi_u = \arccos(\pm 1)$ at $\tilde{k} = \tilde{k}^\pm$. Thus, $\phi_u|_{\tilde{k}=\tilde{k}^+} = 0$. We also note from Eq. (D.5) that when $\tilde{k} = \tilde{k}^-$, we require that $\tilde{q}x > \tilde{k}_u$. Thus,

$$\begin{aligned} \phi_u|_{\tilde{k}=\tilde{k}^-} &= \arccos \left(\text{sgn} \left(\sqrt{\tilde{k}_u(1+x)} - \sqrt{(\tilde{k}_u + \tilde{q})x} \right) \right) = \arccos \left(\text{sgn}(\tilde{k}_u - \tilde{q}x) \right) \\ &= \pi \Theta(\tilde{q}x - \tilde{k}_u). \end{aligned} \quad (\text{D.40})$$

We also evaluate

$$\varphi(\phi_u, C/D)|_{\tilde{k}=\tilde{k}^+} = 0 \quad \varphi(\phi_u, C_u/D)|_{\tilde{k}=\tilde{k}^+} = 0 \quad (\text{D.41a})$$

$$\varphi(\phi_u, C/D)|_{\tilde{k}=\tilde{k}^-} = \pi\Theta(\tilde{q}x - \tilde{k}_u) \quad \varphi(\phi_u, C_u/D)|_{\tilde{k}=\tilde{k}^-} = \pi\Theta(\tilde{q}x - \tilde{k}_u) \quad (\text{D.41b})$$

Upon defining

$$\Phi \equiv \varphi(\phi_u, C/D) ; \quad \Phi_u \equiv \varphi(\phi_u, C_u/D) = \Phi_u^0 \text{sgn}(\tilde{k} - \tilde{k}_u) , \quad (\text{D.42})$$

in terms of the function φ that we defined in Eq. (D.9), we can derive the following expressions that we will also need for computing the integral of \mathcal{I} over \tilde{k} in Eq. (D.24):

$$\Phi = \psi + \arctan\left(\frac{\tilde{q}x - \tilde{k}_u}{\tilde{k}^+} \tan\frac{\psi}{2}\right) - \arctan\left(\frac{\tilde{q}x + \tilde{k}_u + \tilde{q}}{\tilde{k}^+ + \tilde{q}} \tan\frac{\psi}{2}\right), \quad (\text{D.43a})$$

$$\Phi_u = (2\psi - \Phi)\text{sgn}(\tilde{k} - \tilde{k}_u) + 2\pi\Theta(\tilde{k}_u - \tilde{k}), \quad (\text{D.43b})$$

$$\frac{d\Phi}{d\psi} = \frac{d\Phi}{d\tilde{k}} \frac{d\tilde{k}}{d\psi} = \frac{1}{2} \left(2 + \frac{x\tilde{q} - \tilde{k}_u}{\tilde{k}} - \frac{x\tilde{q} + \tilde{k}_u + \tilde{q}}{\tilde{k} + \tilde{q}} \right), \quad (\text{D.43c})$$

$$\frac{d\Phi_u^0}{d\psi} = \frac{d\Phi_u^0}{d\tilde{k}} \frac{d\tilde{k}}{d\psi} = \frac{1}{2} \left(2 - \frac{x\tilde{q} - \tilde{k}_u}{\tilde{k}} + \frac{x\tilde{q} + \tilde{k}_u + \tilde{q}}{\tilde{k} + \tilde{q}} \right). \quad (\text{D.43d})$$

We have almost completed laying the groundwork needed for the evaluation of the integral in Eq. (D.24) for each of the seven integrands $m_i\mathcal{P}_u$. First, though, we need the following integrals, each of which can be obtained via integration by parts after recognizing that $d\tilde{k} = -\Delta_k \sin\psi d\psi$:

$$\int d\tilde{k} e^{-n\tilde{k}} \frac{\phi_u}{\pi} = -\frac{e^{-n\tilde{k}} \phi_u}{n\pi} + \frac{1}{n} \int \frac{d\psi}{\pi} \frac{d\phi_u}{d\psi} e^{-n\tilde{k}} \quad (\text{D.44a})$$

$$\begin{aligned} \int d\tilde{k} e^{-n\tilde{k}} \int_0^{\phi_u} \frac{d\phi'}{\pi(C - D \cos\phi')} \\ = \tilde{q} e^{n(\tilde{k}_u + \tilde{q})} \left(-E_1\left(n(\tilde{k} + \tilde{k}_u + \tilde{q})\right) \frac{\Phi}{\pi} + \int \frac{d\psi}{\pi} \frac{d\Phi}{d\psi} E_1\left(n(\tilde{k} + \tilde{k}_u + \tilde{q})\right) \right) \end{aligned} \quad (\text{D.44b})$$

$$\begin{aligned} \int d\tilde{k} e^{-n\tilde{k}} \int_0^{\phi_u} \frac{d\phi'}{\pi(C_u - D \cos\phi')} \\ = \tilde{q} e^{-n\tilde{k}_u} \left(-E_1\left(n(\tilde{k} - \tilde{k}_u)\right) \frac{\Phi_u}{\pi} + \int \frac{d\psi}{\pi} \frac{d\Phi_u^0}{d\psi} E_1\left(n(\tilde{k} - \tilde{k}_u)\right) \right), \end{aligned} \quad (\text{D.44c})$$

$$\begin{aligned} \int d\tilde{k} e^{-n\tilde{k}} \int_0^{\phi_u} (C - D \cos\phi') \frac{d\phi'}{\pi} \\ = -\frac{\phi_u}{\pi} \left(\frac{h}{\tilde{q}^2 n^2} \Gamma(2, n\tilde{k}) + \frac{f}{n\tilde{q}} e^{-n\tilde{k}} \right) \\ + \int \frac{d\psi}{\pi} \left(\frac{d\phi_u}{d\psi} \left(\frac{h}{\tilde{q}^2 n^2} \Gamma(2, n\tilde{k}) + \frac{f}{n\tilde{q}} e^{-n\tilde{k}} \right) + \frac{\Delta_k^2 \sin^2\psi}{\tilde{q}} e^{-n\tilde{k}} \right) \end{aligned} \quad (\text{D.44d})$$

$$\int d\tilde{k} e^{-n\tilde{k}} \int_0^{\phi_u} (C - D \cos \phi')^2 \frac{d\phi'}{\pi} \quad (\text{D.44e})$$

$$\begin{aligned} &= \frac{\phi_u}{\pi} \left(\frac{h^2 + 2f\tilde{k}_u}{\tilde{q}^4 n^3} \Gamma(3, n\tilde{k}) + \frac{2f}{\tilde{q}^3 n^2} (h + \tilde{k}_u) \Gamma(2, n\tilde{k}) + \frac{f^2}{\tilde{q}^2 n} e^{-n\tilde{k}} \right) \\ &+ \frac{1}{\tilde{q}^2 n} \int \frac{d\psi}{\pi} \frac{d\phi_u}{d\psi} \left(\frac{h^2 + 2f\tilde{k}_u}{\tilde{q}^2 n^2} \Gamma(3, n\tilde{k}) + \frac{2f}{\tilde{q} n} (h + \tilde{k}_u) \Gamma(2, n\tilde{k}) + f^2 e^{-n\tilde{k}} \right) \\ &+ \int \frac{d\psi}{\pi} \frac{\Delta_k^2}{2\tilde{q}} \sin^2 \psi e^{-n\tilde{k}} \left(3 \left(\frac{f}{\tilde{q}} + \frac{h}{\tilde{q}^2} \tilde{k} \right) + 1 + x \right), \end{aligned}$$

$$\int d\tilde{k} e^{-n\tilde{k}} \int_0^{\phi_u} \frac{d\phi'}{\pi (C - D \cos \phi')^2} \quad (\text{D.44f})$$

$$\begin{aligned} &= -\tilde{q} \frac{\Phi}{\pi} e^{n(\tilde{k}_u + \tilde{q})} \left[hn \Gamma(-1, n(\tilde{k} + \tilde{k}_u + \tilde{q})) - 2f\tilde{k}_u n^2 \Gamma(-2, n(\tilde{k} + \tilde{k}_u + \tilde{q})) \right] \\ &+ \tilde{q} e^{n(\tilde{k}_u + \tilde{q})} \int \frac{d\psi}{\pi} \frac{d\Phi}{d\psi} \left[hn \Gamma(-1, n(\tilde{k} + \tilde{k}_u + \tilde{q})) - 2f\tilde{k}_u n^2 \Gamma(-2, n(\tilde{k} + \tilde{k}_u + \tilde{q})) \right] \\ &- \tilde{q} \int \frac{d\psi}{\pi} e^{-n\tilde{k}} \frac{\Delta_k^2 \sin^2 \psi}{(1+x)(\tilde{k} + \tilde{k}_u + \tilde{q})^2} \end{aligned}$$

$$\int d\tilde{k} e^{-n\tilde{k}} \int_0^{\phi_u} \frac{d\phi'}{\pi (C_u - D \cos \phi')^2} \quad (\text{D.44g})$$

$$\begin{aligned} &= -\tilde{q} \frac{\Phi_u}{\pi} e^{-n\tilde{k}_u} \left[hn \Gamma(-1, n(\tilde{k} - \tilde{k}_u)) + 2f\tilde{k}_u n^2 \Gamma(-2, n(\tilde{k} - \tilde{k}_u)) \right] \\ &+ \tilde{q} e^{-n\tilde{k}_u} \int \frac{d\psi}{\pi} \frac{d\Phi_u^0}{d\psi} \left[hn \Gamma(-1, n(\tilde{k} - \tilde{k}_u)) + 2f\tilde{k}_u n^2 \Gamma(-2, n(\tilde{k} - \tilde{k}_u)) \right] \\ &- \tilde{q} \int \frac{d\psi}{\pi} e^{-n\tilde{k}} \frac{\Delta_k^2 \sin^2 \psi}{x(\tilde{k} - \tilde{k}_u)^2}, \end{aligned}$$

where $h = 2\tilde{k}_u + \tilde{q}$, $f = \tilde{k}_u + \tilde{q}$, $E_n(x) \equiv \int_1^\infty dt e^{-xt}/t^n$ is the generalized exponential integral, and $\Gamma(s, x) \equiv \int_x^\infty dt t^{s-1} e^{-t}$ is the upper incomplete gamma function.

We note, again, a simplification when integrating over the full range. For example, the integral of $m_3 \mathcal{P}_u$ evaluates to

$$\begin{aligned} &\int_0^\infty d\tilde{k} e^{-n\tilde{k}} \int_0^{2\pi} \frac{d\phi'}{2\pi} m_3 \mathcal{P}_u = \left(\int_0^{\tilde{k}^-} + \int_{\tilde{k}^-}^{\tilde{k}^+} + \int_{\tilde{k}^+}^\infty \right) d\tilde{k} e^{-n\tilde{k}} \int_0^{2\pi} \frac{d\phi'}{2\pi} m_3 \mathcal{P}_u \quad (\text{D.45}) \\ &= \left(\int_0^{\tilde{k}^-} + \int_{\tilde{k}^-}^{\tilde{k}^+} + \int_{\tilde{k}^+}^\infty \right) d\tilde{k} e^{-n\tilde{k}} \left(\mathcal{P}_{u13} - \Theta(\tilde{k}^- < \tilde{k} < \tilde{k}^+) \frac{\phi_u}{\pi} \right) \\ &= \left(\int_0^{\tilde{k}^-} \Theta(\tilde{k}_u - \tilde{q}x) + \int_{\tilde{k}^+}^\infty \right) d\tilde{k} e^{-n\tilde{k}} - \int_{\tilde{k}^-}^{\tilde{k}^+} d\tilde{k} e^{-n\tilde{k}} \frac{\phi_u}{\pi} \end{aligned}$$

$$\begin{aligned}
&= \frac{1}{n} \Theta(\tilde{k}_u - \tilde{q}x) - \frac{1}{n} \int_{\pi}^0 \frac{d\psi}{\pi} \frac{d\phi_u}{d\psi} e^{-n\tilde{k}} \\
&= \frac{1}{n} \Theta(\tilde{k}_u - \tilde{q}x) + \frac{1}{n} \int_0^{\pi} \frac{d\psi}{\pi} \frac{d\phi_u}{d\psi} e^{-n\tilde{k}},
\end{aligned}$$

where in the fourth equality, we have employed integration by parts and a change of integration variable to ψ .

Finally, we obtain explicit expressions for the seven integrals over \tilde{k} that we need in Section 3 in order to compute the cumulative distribution for the conditional probability $P(\tilde{k})$ in Eq. (3.27) or the conditional probability $P(\tilde{k}_\chi^{\min})$ in Eq. (3.26):

$$\int_0^\infty d\tilde{k} e^{-n\tilde{k}} \int_0^{2\pi} \frac{d\phi'}{2\pi} m_1 \mathcal{P}_u \tag{D.46a}$$

$$\begin{aligned}
&= \Theta(\tilde{k}_u - \tilde{q}x) \left(\frac{2(h^2 + 2f\tilde{k}_u)}{\tilde{q}^4 n^3} + \frac{2f}{\tilde{q}^3 n^2} (h + \tilde{k}_u) + \frac{f^2}{\tilde{q}^2 n} \right) \\
&\quad + \frac{1}{\tilde{q}^2 n} \int_0^\pi \frac{d\psi}{\pi} \frac{d\phi_u}{d\psi} \left(\frac{h^2 + 2f\tilde{k}_u}{\tilde{q}^2 n^2} \Gamma(3, n\tilde{k}) + \frac{2f}{\tilde{q} n} (h + \tilde{k}_u) \Gamma(2, n\tilde{k}) + f^2 e^{-n\tilde{k}} \right) \\
&\quad + \frac{1}{2\tilde{q}} \int_0^\pi \frac{d\psi}{\pi} \Delta_k^2 \sin^2 \psi e^{-n\tilde{k}} \left[3 \left(\frac{f}{\tilde{q}} + \frac{h}{\tilde{q}^2} \tilde{k} \right) + 1 + x \right]
\end{aligned}$$

$$\int_0^\infty d\tilde{k} e^{-n\tilde{k}} \int_0^{2\pi} \frac{d\phi'}{2\pi} m_2 \mathcal{P}_u \tag{D.46b}$$

$$\begin{aligned}
&= \Theta(\tilde{k}_u - \tilde{q}x) \left(\frac{h}{\tilde{q}^2 n^2} + \frac{f}{n\tilde{q}} \right) \\
&\quad + \int_0^\pi \frac{d\psi}{\pi} \left[\frac{d\phi_u}{d\psi} \left(\frac{h}{\tilde{q}^2 n^2} \Gamma(2, n\tilde{k}) + \frac{f}{n\tilde{q}} e^{-n\tilde{k}} \right) + \frac{\Delta_k^2 \sin^2 \psi}{\tilde{q}} e^{-n\tilde{k}} \right]
\end{aligned}$$

$$\int_0^\infty d\tilde{k} e^{-n\tilde{k}} \int_0^{2\pi} \frac{d\phi'}{2\pi} m_3 \mathcal{P}_u = \frac{1}{n} \Theta(\tilde{k}_u - \tilde{q}x) + \frac{1}{n} \int_0^\pi \frac{d\psi}{\pi} \frac{d\phi_u}{d\psi} e^{-n\tilde{k}} \tag{D.46c}$$

$$\int_0^\infty d\tilde{k} e^{-n\tilde{k}} \int_0^{2\pi} \frac{d\phi'}{2\pi} m_4 \mathcal{P}_u \tag{D.46d}$$

$$= \tilde{q} e^{n(\tilde{k}_u + \tilde{q})} \left[E_1(n(\tilde{k}_u + \tilde{q})) \Theta(\tilde{k}_u - \tilde{q}x) + \int_0^\pi \frac{d\psi}{\pi} \frac{d\Phi}{d\psi} E_1(n(\tilde{k} + \tilde{k}_u + \tilde{q})) \right]$$

$$\int_0^\infty d\tilde{k} e^{-n\tilde{k}} \int_0^{2\pi} \frac{d\phi'}{2\pi} m_5 \mathcal{P}_u \tag{D.46e}$$

$$\begin{aligned}
&= \Theta(\tilde{k}_u - \tilde{q}x) \frac{\tilde{q} e^{n(\tilde{k}_u + \tilde{q})}}{(\tilde{k}_u + \tilde{q})} \left[h E_2(n(\tilde{k}_u + \tilde{q})) - 2\tilde{k}_u E_3(n(\tilde{k}_u + \tilde{q})) \right] \\
&\quad + \tilde{q} e^{n(\tilde{k}_u + \tilde{q})} \int_0^\pi \frac{d\psi}{\pi} \frac{d\Phi}{d\psi} \left[hn \Gamma(-1, n(\tilde{k} + \tilde{k}_u + \tilde{q})) - 2f\tilde{k}_u n^2 \Gamma(-2, n(\tilde{k} + \tilde{k}_u + \tilde{q})) \right]
\end{aligned}$$

$$- \tilde{q} \int_0^\pi \frac{d\psi}{\pi} e^{-n\tilde{k}} \frac{\Delta_k^2 \sin^2 \psi}{(1+x)(\tilde{k} + \tilde{k}_u + \tilde{q})^2},$$

$$\int_0^\infty d\tilde{k} e^{-n\tilde{k}} \int_0^{2\pi} \frac{d\phi'}{2\pi} m_6 \mathcal{P}_u \quad (\text{D.46f})$$

$$= \tilde{q} e^{-n\tilde{k}_u} \left[-E_1(-n\tilde{k}_u) \Theta(\tilde{k}_u - \tilde{q}x) + \int_0^\pi \frac{d\psi}{\pi} \frac{d\Phi_u^0}{d\psi} E_1(n(\tilde{k} - \tilde{k}_u)) \right],$$

$$\int_0^\infty d\tilde{k} e^{-n\tilde{k}} \int_0^{2\pi} \frac{d\phi'}{2\pi} m_7 \mathcal{P}_u \quad (\text{D.46g})$$

$$= \Theta(\tilde{k}_u - \tilde{q}x) \tilde{q} \left[3 + \frac{2\tilde{q}}{\tilde{k}_u} + n(\tilde{q} + \tilde{k}_u) + e^{-n\tilde{k}_u} E_1(-n\tilde{k}_u) \left(n(\tilde{q} + 2\tilde{k}_u) + n^2 \tilde{k}_u (\tilde{q} + \tilde{k}_u) \right) \right]$$

$$+ \tilde{q} e^{-n\tilde{k}_u} \int_0^\pi \frac{d\psi}{\pi} \frac{d\Phi_u^0}{d\psi} \left[hn\Gamma(-1, n(\tilde{k} - \tilde{k}_u)) + 2f\tilde{k}_u n^2 \Gamma(-2, n(\tilde{k} - \tilde{k}_u)) \right]$$

$$- \tilde{q} \int_0^\pi \frac{d\psi}{\pi} e^{-n\tilde{k}} \frac{\Delta_k^2 \sin^2 \psi}{x(\tilde{k} - \tilde{k}_u)^2}.$$

The integrals over ψ in the expressions above can be evaluated using Eq. (D.39c), Eqs. (D.43), and upon noting the following expansions

$$e^{-n\Delta_k \cos \psi} = \sum_{r=-\infty}^{\infty} I_r(n\Delta_k) (-1)^r \cos(r\psi), \quad (\text{D.47a})$$

$$\frac{\sqrt{a^2 - 1}}{a + \cos \psi} = 1 + 2 \sum_{n=1}^{\infty} \left(\sqrt{a^2 - 1} - a \right)^n \cos(n\psi), \quad (\text{D.47b})$$

which admit integrals

$$\frac{1}{\pi} \int_0^\pi d\psi e^{-n\Delta_k \cos \psi} = I_0(n\Delta_k), \quad (\text{D.48a})$$

$$\frac{1}{\pi} \int_0^\pi d\psi \frac{\sqrt{a^2 - 1}}{a + \cos \psi} e^{-n\Delta_k \cos \psi} = I_0(n\Delta_k) + 2 \sum_{r=1}^{\infty} (-1)^r \left(\sqrt{a^2 - 1} - a \right)^r I_r(n\Delta_k), \quad (\text{D.48b})$$

where I_r is the r 'th modified Bessel function of the first kind.

D.3 k_χ^{\min} and x Integrals

Next, in order to compute the cumulative distribution for the conditional probability $P(k_\chi^{\min})$ in Eq. (3.26) which we reproduce here

$$P_i(k_\chi^{\min}|x) \propto \int_0^\infty d\tilde{k} \int_0^{2\pi} d\phi m_i^{D,B}(t, u) | \mathcal{J} | \mathcal{P}_u, \quad (\text{D.49})$$

or in order to compute the conditional probability $P(x)$ in Eq. (3.26), reproduced here

$$P_i(x|ab \leftrightarrow cd) \propto \int_0^{p_{\text{in}}} dk_\chi^{\min} \int_0^\infty d\tilde{k} \int_0^{2\pi} d\phi m_i^{D,B}(t, u) | \mathcal{J} | \mathcal{P}_u, \quad (\text{D.50})$$

we need to integrate the expressions that we have obtained in Appendix D.2 over \tilde{k}_χ^{\min} . And then the last step, needed in order to obtain the cumulative distribution for the conditional probability $P(x)$ and the total probability for elastic scattering, is to integrate over x . We perform these integrals numerically.

We perform the integral over k_χ^{\min} using GSL's QAGS algorithm [96–98]. Direct numerical evaluation of the x integral after numerically integrating over \tilde{k}_χ^{\min} would be computationally expensive, and so we use a precomputed, finely grained table of cumulative integrals in x , binned in p_{in}/T . We cover $p_{\text{in}}/T \in [0, 1500]$ with $N_{p_{\text{in}}} = 100$ uniformly-sized bins. For an arbitrary p_{in}/T at runtime we linearly interpolate between the two nearest bins. For each p_{in}/T bin and each (n, i, D, B) channel we tabulate the seven cumulative integrals

$$\Phi_i(x) \equiv \int_0^x dx' P_i(x' | ab \leftrightarrow cd), \quad x \in [0, 1], \quad (\text{D.51})$$

for a uniformly spaced array of $N_x = 100$ bins in $x \in [0, 1]$. Finally, recalling that n denotes the exponent in the convergent geometric sum in Eq. (D.24), for numerical evaluation we must truncate the sum at some finite n , as it is not possible to evaluate the requisite integrals for infinitely many values of n . We have performed the numerical integrations of the integrals needed to evaluate the sum of the first 17 terms, $1 \leq n \leq 17$, in the convergent geometric sum (D.24). For an arbitrary value of x sampled at runtime from $\Phi_i(x)$, we calculate $P_i(\tilde{k}_\chi^{\min}|x)$ in Eq. (D.49) by linearly interpolating between the value of $P_i(\tilde{k}_\chi^{\min}|x)$ computed for the two nearest bins in x .

Finally, last but not least, the total probability of elastic scattering is obtained by evaluating the seven $\Phi_i(x)$ in Eq. (D.51) at $x = 1$ to obtain the seven P_i of Eq. (3.23), and then evaluating the appropriate linear combination as described below Eq. (3.23).

References

- [1] **PHENIX** Collaboration, K. Adcox et al., *Formation of dense partonic matter in relativistic nucleus-nucleus collisions at RHIC: Experimental evaluation by the PHENIX collaboration*, *Nucl. Phys. A* **757** (2005) 184–283, [[nucl-ex/0410003](#)].
- [2] **BRAHMS** Collaboration, I. Arsene et al., *Quark gluon plasma and color glass condensate at RHIC? The Perspective from the BRAHMS experiment*, *Nucl. Phys. A* **757** (2005) 1–27, [[nucl-ex/0410020](#)].
- [3] **PHOBOS** Collaboration, B. B. Back et al., *The PHOBOS perspective on discoveries at RHIC*, *Nucl. Phys. A* **757** (2005) 28–101, [[nucl-ex/0410022](#)].
- [4] **STAR** Collaboration, J. Adams et al., *Experimental and theoretical challenges in the search for the quark gluon plasma: The STAR Collaboration's critical assessment of the evidence from RHIC collisions*, *Nucl. Phys. A* **757** (2005) 102–183, [[nucl-ex/0501009](#)].
- [5] M. Gyulassy and L. McLerran, *New forms of QCD matter discovered at RHIC*, *Nucl. Phys. A* **750** (2005) 30–63, [[nucl-th/0405013](#)].
- [6] D. d'Enterria, *Jet quenching*, *Landolt-Bornstein* **23** (2010) 471, [[arXiv:0902.2011](#)].
- [7] U. A. Wiedemann, *Jet Quenching in Heavy Ion Collisions*, [arXiv:0908.2306](#).

- [8] A. Majumder and M. Van Leeuwen, *The Theory and Phenomenology of Perturbative QCD Based Jet Quenching*, *Prog. Part. Nucl. Phys.* **66** (2011) 41–92, [[arXiv:1002.2206](#)].
- [9] B. V. Jacak and B. Muller, *The exploration of hot nuclear matter*, *Science* **337** (2012) 310–314.
- [10] B. Muller, J. Schukraft, and B. Wyslouch, *First Results from Pb+Pb collisions at the LHC*, *Ann. Rev. Nucl. Part. Sci.* **62** (2012) 361–386, [[arXiv:1202.3233](#)].
- [11] Y. Mehtar-Tani, J. G. Milhano, and K. Tywoniuk, *Jet physics in heavy-ion collisions*, *Int. J. Mod. Phys. A* **28** (2013) 1340013, [[arXiv:1302.2579](#)].
- [12] M. Connors, C. Nattrass, R. Reed, and S. Salur, *Jet measurements in heavy ion physics*, *Rev. Mod. Phys.* **90** (2018) 025005, [[arXiv:1705.01974](#)].
- [13] W. Busza, K. Rajagopal, and W. van der Schee, *Heavy Ion Collisions: The Big Picture, and the Big Questions*, *Ann. Rev. Nucl. Part. Sci.* **68** (2018) 339–376, [[arXiv:1802.04801](#)].
- [14] S. Cao and X.-N. Wang, *Jet quenching and medium response in high-energy heavy-ion collisions: a review*, *Rept. Prog. Phys.* **84** (2021), no. 2 024301, [[arXiv:2002.04028](#)].
- [15] L. Cunqueiro and A. M. Sickles, *Studying the QGP with Jets at the LHC and RHIC*, *Prog. Part. Nucl. Phys.* **124** (2022) 103940, [[arXiv:2110.14490](#)].
- [16] L. Apolinário, Y.-J. Lee, and M. Winn, *Heavy quarks and jets as probes of the QGP*, *Prog. Part. Nucl. Phys.* **127** (2022) 103990, [[arXiv:2203.16352](#)].
- [17] X.-N. Wang and U. A. Wiedemann, *QGP@50: More than Four Decades of Jet Quenching*, 8, 2025. [[arXiv:2508.18794](#)].
- [18] H. Liu, K. Rajagopal, and U. A. Wiedemann, *Calculating the jet quenching parameter from AdS/CFT*, *Phys. Rev. Lett.* **97** (2006) 182301, [[hep-ph/0605178](#)].
- [19] H. Liu, K. Rajagopal, and U. A. Wiedemann, *Wilson loops in heavy ion collisions and their calculation in AdS/CFT*, *JHEP* **03** (2007) 066, [[hep-ph/0612168](#)].
- [20] F. D’Eramo, H. Liu, and K. Rajagopal, *Transverse Momentum Broadening and the Jet Quenching Parameter*, *Redux*, *Phys. Rev. D* **84** (2011) 065015, [[arXiv:1006.1367](#)].
- [21] F. D’Eramo, M. Lekaveckas, H. Liu, and K. Rajagopal, *Momentum Broadening in Weakly Coupled Quark-Gluon Plasma (with a view to finding the quasiparticles within liquid quark-gluon plasma)*, *JHEP* **05** (2013) 031, [[arXiv:1211.1922](#)].
- [22] G. Molière, *Theorie der Streuung schneller geladener Teilchen I. Einzelstreuung am abgeschirmten Coulomb-Feld*, *Zeitschrift für Naturforschung A* **2** (1947) 133.
- [23] G. Molière, *Theorie der Streuung schneller geladener Teilchen II. Mehrfach- und Vielfachstreuung*, *Zeitschrift für Naturforschung A* **3** (1948) 78–97.
- [24] G. Molière, *Theorie der Streuung schneller geladener Teilchen III. Die Vielfachstreuung von Bahnpuren unter Berücksichtigung der statistischen Kopplung*, *Zeitschrift für Naturforschung A* **10** (1955) 177.
- [25] J. Casalderrey-Solana, D. C. Gulhan, J. G. Milhano, D. Pablos, and K. Rajagopal, *A Hybrid Strong/Weak Coupling Approach to Jet Quenching*, *JHEP* **10** (2014) 019, [[arXiv:1405.3864](#)]. [Erratum: *JHEP* 09, 175 (2015)].
- [26] J. Casalderrey-Solana, D. C. Gulhan, J. G. Milhano, D. Pablos, and K. Rajagopal, *Predictions for Boson-Jet Observables and Fragmentation Function Ratios from a Hybrid Strong/Weak Coupling Model for Jet Quenching*, *JHEP* **03** (2016) 053, [[arXiv:1508.00815](#)].

- [27] J. Casalderrey-Solana, D. Gulhan, G. Milhano, D. Pablos, and K. Rajagopal, *Angular Structure of Jet Quenching Within a Hybrid Strong/Weak Coupling Model*, *JHEP* **03** (2017) 135, [[arXiv:1609.05842](#)].
- [28] Z. Hulcher, D. Pablos, and K. Rajagopal, *Resolution Effects in the Hybrid Strong/Weak Coupling Model*, *JHEP* **03** (2018) 010, [[arXiv:1707.05245](#)].
- [29] J. Casalderrey-Solana, Z. Hulcher, G. Milhano, D. Pablos, and K. Rajagopal, *Simultaneous description of hadron and jet suppression in heavy-ion collisions*, *Phys. Rev. C* **99** (2019), no. 5 051901, [[arXiv:1808.07386](#)].
- [30] J. Casalderrey-Solana, G. Milhano, D. Pablos, and K. Rajagopal, *Modification of Jet Substructure in Heavy Ion Collisions as a Probe of the Resolution Length of Quark-Gluon Plasma*, *JHEP* **01** (2020) 044, [[arXiv:1907.11248](#)].
- [31] Z. Hulcher, D. Pablos, and K. Rajagopal, *Sensitivity of Jet Observables to the Presence of Quasi-particles in QGP*, *Acta Phys. Polon. Supp.* **16** (2023), no. 1 1–A57, [[arXiv:2208.13593](#)].
- [32] H. Bossi, A. S. Kudinoor, I. Moulton, D. Pablos, A. Rai, and K. Rajagopal, *Imaging the wakes of jets with energy-energy-energy correlators*, *JHEP* **12** (2024) 073, [[arXiv:2407.13818](#)].
- [33] A. S. Kudinoor, D. Pablos, and K. Rajagopal, *Visualizing how the structure of large-radius jets shapes their wakes*, *JHEP* **01** (2026) 020, [[arXiv:2501.18683](#)].
- [34] A. S. Kudinoor, D. Pablos, and K. Rajagopal, *Constraining the Resolution Length of Quark-Gluon Plasma with New Jet Substructure Measurements*, [arXiv:2509.08881](#).
- [35] A. Beraudo, J. F. Du Plessis, D. Pablos, and K. Rajagopal, *Heavy Quark Energy Loss in the Hybrid Model*, [arXiv:2510.24847](#).
- [36] P. M. Chesler and K. Rajagopal, *Jet quenching in strongly coupled plasma*, *Phys. Rev. D* **90** (2014), no. 2 025033, [[arXiv:1402.6756](#)].
- [37] P. M. Chesler and K. Rajagopal, *On the Evolution of Jet Energy and Opening Angle in Strongly Coupled Plasma*, *JHEP* **05** (2016) 098, [[arXiv:1511.07567](#)].
- [38] J. Casalderrey-Solana, J. G. Milhano, D. Pablos, K. Rajagopal, and X. Yao, *Jet Wake from Linearized Hydrodynamics*, *JHEP* **05** (2021) 230, [[arXiv:2010.01140](#)].
- [39] F. D’Eramo, K. Rajagopal, and Y. Yin, *Molière scattering in quark-gluon plasma: finding point-like scatterers in a liquid*, *JHEP* **01** (2019) 172, [[arXiv:1808.03250](#)].
- [40] D. Pablos and S. Sanjurjo, *Color coherence effects in dipole-quark scattering in the soft limit*, *Phys. Rev. D* **110** (2024), no. 11 L111502, [[arXiv:2406.08550](#)].
- [41] **CMS** Collaboration, A. Hayrapetyan et al., *Girth and groomed radius of jets recoiling against isolated photons in lead-lead and proton-proton collisions at $\sqrt{s_{NN}} = 5.02$ TeV*, *Phys. Lett. B* **861** (2025) 139088, [[arXiv:2405.02737](#)].
- [42] P. B. Arnold, G. D. Moore, and L. G. Yaffe, *Effective kinetic theory for high temperature gauge theories*, *JHEP* **01** (2003) 030, [[hep-ph/0209353](#)].
- [43] T. Sjöstrand, S. Ask, J. R. Christiansen, R. Corke, N. Desai, P. Ilten, S. Mrenna, S. Prestel, C. O. Rasmussen, and P. Z. Skands, *An introduction to PYTHIA 8.2*, *Comput. Phys. Commun.* **191** (2015) 159–177, [[arXiv:1410.3012](#)].
- [44] K. J. Eskola, H. Paukkunen, and C. A. Salgado, *EPS09: A New Generation of NLO and LO Nuclear Parton Distribution Functions*, *JHEP* **04** (2009) 065, [[arXiv:0902.4154](#)].

- [45] S. S. Gubser, D. R. Gulotta, S. S. Pufu, and F. D. Rocha, *Gluon energy loss in the gauge-string duality*, *JHEP* **10** (2008) 052, [[arXiv:0803.1470](#)].
- [46] F. Cooper and G. Frye, *Single-particle distribution in the hydrodynamic and statistical thermodynamic models of multiparticle production*, *Phys. Rev. D* **10** (Jul, 1974) 186–189.
- [47] CMS Collaboration, V. Chekhovsky et al., *Evidence of medium response to hard probes using correlations of Z bosons with hadrons in heavy ion collisions*, [arXiv:2507.09307](#).
- [48] P. Caucal and Y. Mehtar-Tani, *Anomalous diffusion in QCD matter*, *Phys. Rev. D* **106** (2022), no. 5 L051501, [[arXiv:2109.12041](#)].
- [49] P. Caucal and Y. Mehtar-Tani, *Universality aspects of quantum corrections to transverse momentum broadening in QCD media*, *JHEP* **09** (2022) 023, [[arXiv:2203.09407](#)].
- [50] J. Barata, Y. Mehtar-Tani, A. Soto-Ontoso, and K. Tywoniuk, *Revisiting transverse momentum broadening in dense QCD media*, *Phys. Rev. D* **104** (2021), no. 5 054047, [[arXiv:2009.13667](#)].
- [51] J. Barata, Y. Mehtar-Tani, A. Soto-Ontoso, and K. Tywoniuk, *Medium-induced radiative kernel with the Improved Opacity Expansion*, *JHEP* **09** (2021) 153, [[arXiv:2106.07402](#)].
- [52] N. Armesto, C. A. Salgado, and U. A. Wiedemann, *Measuring the collective flow with jets*, *Phys. Rev. Lett.* **93** (2004) 242301, [[hep-ph/0405301](#)].
- [53] Y. He, L.-G. Pang, and X.-N. Wang, *Gradient Tomography of Jet Quenching in Heavy-Ion Collisions*, *Phys. Rev. Lett.* **125** (2020), no. 12 122301, [[arXiv:2001.08273](#)].
- [54] J. Barata, A. V. Sadofyev, and X.-N. Wang, *Quantum partonic transport in QCD matter*, *Phys. Rev. D* **107** (2023), no. 5 L051503, [[arXiv:2210.06519](#)].
- [55] Y. Fu, J. Casalderrey-Solana, and X.-N. Wang, *Asymmetric transverse momentum broadening in an inhomogeneous medium*, *Phys. Rev. D* **107** (2023), no. 5 054038, [[arXiv:2204.05323](#)].
- [56] A. V. Sadofyev, M. D. Sievert, and I. Vitev, *Ab initio coupling of jets to collective flow in the opacity expansion approach*, *Phys. Rev. D* **104** (2021), no. 9 094044, [[arXiv:2104.09513](#)].
- [57] J. Barata, A. V. Sadofyev, and C. A. Salgado, *Jet broadening in dense inhomogeneous matter*, *Phys. Rev. D* **105** (2022), no. 11 114010, [[arXiv:2202.08847](#)].
- [58] J. Barata, J. G. Milhano, and A. V. Sadofyev, *Picturing QCD jets in anisotropic matter: from jet shapes to energy energy correlators*, *Eur. Phys. J. C* **84** (2024), no. 2 174, [[arXiv:2308.01294](#)].
- [59] M. V. Kuzmin, X. Mayo López, J. Reiten, and A. V. Sadofyev, *Jet quenching in anisotropic flowing matter*, *Phys. Rev. D* **109** (2024), no. 1 014036, [[arXiv:2309.00683](#)].
- [60] M. V. Kuzmin and X. Mayo López, *Gluon radiation inside a flowing medium*, [arXiv:2406.14628](#).
- [61] J. Bahder, H. Rahman, M. D. Sievert, and I. Vitev, *Signatures of jet drift in quark-gluon plasma hard-probe observables*, *Phys. Rev. Res.* **8** (2026), no. 1 L012016, [[arXiv:2412.05474](#)].
- [62] N. Armesto, L. Cunqueiro, and C. A. Salgado, *Q-PYTHIA: A Medium-modified implementation of final state radiation*, *Eur. Phys. J. C* **63** (2009) 679–690, [[arXiv:0907.1014](#)].
- [63] K. Zapp, G. Ingelman, J. Rathsman, J. Stachel, and U. A. Wiedemann, *A Monte Carlo Model for 'Jet Quenching'*, *Eur. Phys. J. C* **60** (2009) 617–632, [[arXiv:0804.3568](#)].

- [64] **JETSCAPE** Collaboration, S. Cao et al., *Multistage Monte-Carlo simulation of jet modification in a static medium*, *Phys. Rev. C* **96** (2017), no. 2 024909, [[arXiv:1705.00050](#)].
- [65] **JETSCAPE** Collaboration, A. Kumar et al., *JETSCAPE framework: $p + p$ results*, *Phys. Rev. C* **102** (2020), no. 5 054906, [[arXiv:1910.05481](#)].
- [66] **JETSCAPE** Collaboration, C. Sirimanna et al., *Hard-photon-triggered jets in p - p and A - A collisions*, *Phys. Rev. C* **111** (2025), no. 6 064911, [[arXiv:2412.19738](#)].
- [67] M. Cacciari, G. P. Salam, and G. Soyez, *The anti- k_t jet clustering algorithm*, *JHEP* **04** (2008) 063, [[arXiv:0802.1189](#)].
- [68] M. Cacciari, G. P. Salam, and G. Soyez, *FastJet User Manual*, *Eur. Phys. J. C* **72** (2012) 1896, [[arXiv:1111.6097](#)].
- [69] J. G. Milhano and K. C. Zapp, *Origins of the di-jet asymmetry in heavy ion collisions*, *Eur. Phys. J. C* **76** (2016), no. 5 288, [[arXiv:1512.08107](#)].
- [70] K. Rajagopal, A. V. Sadofyev, and W. van der Schee, *Evolution of the jet opening angle distribution in holographic plasma*, *Phys. Rev. Lett.* **116** (2016), no. 21 211603, [[arXiv:1602.04187](#)].
- [71] J. Brewer, K. Rajagopal, A. Sadofyev, and W. Van Der Schee, *Evolution of the Mean Jet Shape and Dijet Asymmetry Distribution of an Ensemble of Holographic Jets in Strongly Coupled Plasma*, *JHEP* **02** (2018) 015, [[arXiv:1710.03237](#)].
- [72] Y. Mehtar-Tani and K. Tywoniuk, *Sudakov suppression of jets in QCD media*, *Phys. Rev. D* **98** (2018), no. 5 051501, [[arXiv:1707.07361](#)].
- [73] P. Caucal, E. Iancu, and G. Soyez, *Deciphering the z_g distribution in ultrarelativistic heavy ion collisions*, *JHEP* **10** (2019) 273, [[arXiv:1907.04866](#)].
- [74] Y.-L. Du, D. Pablos, and K. Tywoniuk, *Deep learning jet modifications in heavy-ion collisions*, *JHEP* **21** (2020) 206, [[arXiv:2012.07797](#)].
- [75] P. Caucal, A. Soto-Ontoso, and A. Takacs, *Dynamically groomed jet radius in heavy-ion collisions*, *Phys. Rev. D* **105** (2022), no. 11 114046, [[arXiv:2111.14768](#)].
- [76] J. Brewer, Q. Brodsky, and K. Rajagopal, *Disentangling jet modification in jet simulations and in Z +jet data*, *JHEP* **02** (2022) 175, [[arXiv:2110.13159](#)].
- [77] D. Pablos and A. Soto-Ontoso, *Pushing forward jet substructure measurements in heavy-ion collisions*, *Phys. Rev. D* **107** (2023), no. 9 094003, [[arXiv:2210.07901](#)].
- [78] Y. L. Dokshitzer, G. D. Leder, S. Moretti, and B. R. Webber, *Better jet clustering algorithms*, *JHEP* **08** (1997) 001, [[hep-ph/9707323](#)].
- [79] M. Wobisch and T. Wengler, *Hadronization corrections to jet cross-sections in deep inelastic scattering*, in *Workshop on Monte Carlo Generators for HERA Physics (Plenary Starting Meeting)*, pp. 270–279, 4, 1998. [[hep-ph/9907280](#)].
- [80] A. J. Larkoski, S. Marzani, G. Soyez, and J. Thaler, *Soft Drop*, *JHEP* **05** (2014) 146, [[arXiv:1402.2657](#)].
- [81] **CMS** Collaboration, A. M. Sirunyan et al., *Measurement of the Splitting Function in pp and Pb - Pb Collisions at $\sqrt{s_{NN}} = 5.02$ TeV*, *Phys. Rev. Lett.* **120** (2018), no. 14 142302, [[arXiv:1708.09429](#)].

- [82] **ATLAS** Collaboration, G. Aad et al., *Measurement of soft-drop jet observables in pp collisions with the ATLAS detector at $\sqrt{s} = 13$ TeV*, *Phys. Rev. D* **101** (2020), no. 5 052007, [[arXiv:1912.09837](#)].
- [83] **CMS** Collaboration, A. M. Sirunyan et al., *Measurement of the groomed jet mass in PbPb and pp collisions at $\sqrt{s_{NN}} = 5.02$ TeV*, *JHEP* **10** (2018) 161, [[arXiv:1805.05145](#)].
- [84] **ALICE** Collaboration, S. Acharya et al., *Exploration of jet substructure using iterative declustering in pp and Pb–Pb collisions at LHC energies*, *Phys. Lett. B* **802** (2020) 135227, [[arXiv:1905.02512](#)].
- [85] **A Large Ion Collider Experiment, ALICE** Collaboration, S. Acharya et al., *Measurement of the groomed jet radius and momentum splitting fraction in pp and Pb–Pb collisions at $\sqrt{s_{NN}} = 5.02$ TeV*, *Phys. Rev. Lett.* **128** (2022), no. 10 102001, [[arXiv:2107.12984](#)].
- [86] **ATLAS** Collaboration, G. Aad et al., *Measurement of substructure-dependent jet suppression in Pb+Pb collisions at 5.02 TeV with the ATLAS detector*, *Phys. Rev. C* **107** (2023), no. 5 054909, [[arXiv:2211.11470](#)].
- [87] **ATLAS** Collaboration, G. Aad et al., *Measurement of substructure-dependent suppression of large-radius jets with charged particles in Pb+Pb collisions with ATLAS*, *Phys. Lett. B* **871** (2025) 139929, [[arXiv:2504.04805](#)].
- [88] H. A. Andrews, *Exploring the phase space of medium induced QCD radiation with jets in ALICE at the LHC*. PhD thesis, Birmingham U., 2019.
- [89] L. Apolinário, D. Costa, and A. Soto-Ontoso, *Bottom-up approach to describe groomed jet data in heavy-ion collisions*, [[arXiv:2601.13310](#)].
- [90] Y. Mehtar-Tani, A. Soto-Ontoso, and K. Tywoniuk, *Dynamical grooming of QCD jets*, *Phys. Rev. D* **101** (2020), no. 3 034004, [[arXiv:1911.00375](#)].
- [91] **ALICE** Collaboration, S. Acharya et al., *Search for quasi-particle scattering in the quark-gluon plasma with jet splittings in pp and Pb–Pb collisions at $\sqrt{s_{NN}} = 5.02$ TeV*, *Phys. Rev. Lett.* **135** (2025), no. 3 031901, [[arXiv:2409.12837](#)].
- [92] X. Zhang, L. Apolinário, J. G. Milhano, and M. Płoskoń, *Sub-jet structure as a discriminating quenching probe*, *Nucl. Phys. A* **956** (2016) 597–600, [[arXiv:1512.09255](#)].
- [93] **ALICE** Collaboration, N. Strangmann, “Nuclear modification of π^0 production in O-O collisions with ALICE.” Talk at the VIII-th International Conference on the Initial Stages of High-Energy Nuclear Collisions (Initial Stages 2025), Sept., 2025.
- [94] **ATLAS** Collaboration, *Measurement of dijet transverse momentum balance in O+O and pp collisions at 5.36 TeV with the ATLAS detector*, 2025. ATLAS-CONF-2025-010.
- [95] **CMS** Collaboration, A. Hayrapetyan et al., *Discovery of suppressed charged-particle production in ultrarelativistic oxygen-oxygen collisions*, [[arXiv:2510.09864](#)].
- [96] M. Galassi, J. Davies, J. Theiler, B. Gough, G. Jungman, M. Booth, and F. Rossi, *GNU Scientific Library Reference Manual*. Free Software Foundation, 3rd ed., 2009. Version 1.12.
- [97] M. C. Galassi, J. Davies, J. Theiler, B. Gough, G. Jungman, P. Alken, M. Booth, F. Rossi, and R. Ulerich, *GNU Scientific Library*. Network Theory, Ltd., 8, 2019.
- [98] R. Piessens, E. de Doncker-Kapenga, C. W. Überhuber, and D. K. Kahaner, *QUADPACK: A Subroutine Package for Automatic Integration*. Springer, Berlin, 1983.